Davy-Faraday Research Laboratory
The Royal Institution

Department of Geology
University College London
University of London

Electronic Structure Properties of Metal Oxide Surfaces

Thesis submitted for the degree of Philosophiæ Doctor
by

Steven John Gennard

September 2001

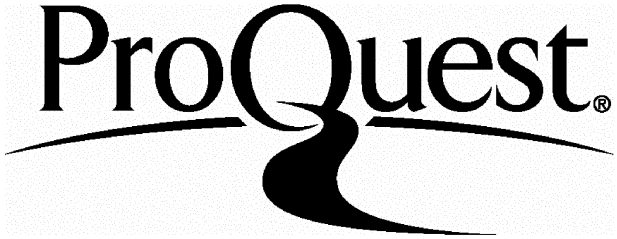

"Now brain, I don't like you and you don't like me,
but if we work on this together I can get back to killing you with beer."

Homer J. Simpson

Table of Contents

List of Figures

List of Tables

Acknowledgements

Anyone who has completed a PhD will know that writing the thesis is, without a doubt, the most difficult part. Myself, I have found that writing these acknowledgements to be even more so. To those who don't get a mention here, you have not been forgotten and will always be remembered.

First and foremost, I have to say that this work would never as reached a conclusion, or have made it into print, without the tireless help and endless support I received from Drs. Furio Corà, and Maria Alfredsson. Your efforts will never be forgotten. I must also mention my two supervisors: Prof. Richard Catlow and Prof. David Price, who have been a great help through this work, and have offered much support during my PhD. The memories of Il Ciocco will stay with me for a very long time to come!

Likewise to Stu Peirson, who has kept me alive and well-fed over the years, both mentally and nutritionally! As my best friend and flatmate, he has been there almost since the beginning of my time in London, and has survived the good times and the bad like a saint. He has helped me more than he will ever realise, and for this I will be eternally grateful.

My thanks go to all the friends and colleagues I met during my three years at the Royal Institution, and especially to those who kept me on the not-so-straight and narrow! Justin Bradley cannot escape a special mention, for all his support, and our many evenings at Brutons! Cheers! And I hope there are many more to come!

Last, but certainly not least, I have to mention my family, to whom I dedicate this thesis. They have always supported me throughout my academic career: from the early days of A-levels, through Cambridge and finally to London. My mum, dad, brother, sister and grandparents all alike, thanks guys!

To the younger generation of my family: my niece Chloe, nephew Ashley and my new niece/nephew due shortly, you have a lot to live up to guys! Sorry! Receiving a special mention here is my Nannan June, who gave me endless hassle to complete this thesis, but unfortunately passed away just days before its completion: *Bye bye Nannan, Good night, God Bless.*

Abstract

In this work we present the results obtained from *ab initio* Quantum Mechanical calculations performed on bulk and surface systems of Cerium Dioxide (CeO_2) and Zirconium Dioxide (ZrO_2). Calculations have been performed using both the Hartree-Fock and Kohn-Sham Hamiltonians using a variety of Density Functional schemes proposed in the literature, including the LDA, GGA, and the new three-term hybrid functional schemes (B3LYP) have been examined in these solid state systems.

We report results obtained from the bulk cubic phase common to both materials, in addition to several of the stable ambient pressure ZrO_2 polymorphs known to exist experimentally. The energetics of the cubic-tetragonal ZrO_2 phase transition have also been examined closely, and the correct order of stability of these ambient pressure phases was predicted in agreement to both experimental and other recent theoretical studies.

Surface calculations were performed in addition to the bulk materials, with work concentrating primarily on the two most thermodynamically stable surfaces of the cubic phase: {011} and {111}. Calculated properties of these surfaces, including electronic and ionic relaxations, and surface energetics were in good agreement to available experimental data, similar *ab initio* calculations and also to a series of interatomic potential based calculations which we preformed. The relative stability of these two surfaces is in very good agreement to previous calculations and experimental studies.

Acknowledgements

Anyone who has completed a PhD will know that writing the thesis is, without a doubt, the most difficult part. Myself, I have found that writing these acknowledgements to be even more so. To those who don't get a mention here, you have not been forgotten and will always be remembered.

First and foremost, I have to say that this work would never as reached a conclusion, or have made it into print, without the tireless help and endless support I received from Drs. Furio Corà, and Maria Alfredsson. Your efforts will never be forgotten. I must also mention my two supervisors: Prof. Richard Catlow and Prof. David Price, who have been a great help through this work, and have offered much support during my PhD. The memories of Il Ciocco will stay with me for a very long time to come!

Likewise to Stu Peirson, who has kept me alive and well-fed over the years, both mentally and nutritionally! As my best friend and flatmate, he has been there almost since the beginning of my time in London, and has survived the good times and the bad like a saint. He has helped me more than he will ever realise, and for this I will be eternally grateful.

My thanks go to all the friends and colleagues I met during my three years at the Royal Institution, and especially to those who kept me on the not-so-straight and narrow! Justin Bradley cannot escape a special mention, for all his support, and our many evenings at Brutons! Cheers! And I hope there are many more to come!

Last, but certainly not least, I have to mention my family, to whom I dedicate this thesis. They have always supported me throughout my academic career: from the early days of A-levels, through Cambridge and finally to London. My mum, dad, brother, sister and grandparents all alike, thanks guys!

To the younger generation of my family: my niece Chloe, nephew Ashley and my new niece/nephew due shortly, you have a lot to live up to guys! Sorry! Receiving a special mention here is my Nannan June, who gave me endless hassle to complete this thesis, but unfortunately passed away just days before its completion: *Bye bye Nannan, Good night, God Bless.*

Abstract

In this work we present the results obtained from *ab initio* Quantum Mechanical calculations performed on bulk and surface systems of Cerium Dioxide (CeO_2) and Zirconium Dioxide (ZrO_2). Calculations have been performed using both the Hartree-Fock and Kohn-Sham Hamiltonians using a variety of Density Functional schemes proposed in the literature, including the LDA, GGA, and the new three-term hybrid functional schemes (B3LYP) have been examined in these solid state systems.

We report results obtained from the bulk cubic phase common to both materials, in addition to several of the stable ambient pressure ZrO_2 polymorphs known to exist experimentally. The energetics of the cubic-tetragonal ZrO_2 phase transition have also been examined closely, and the correct order of stability of these ambient pressure phases was predicted in agreement to both experimental and other recent theoretical studies.

Surface calculations were performed in addition to the bulk materials, with work concentrating primarily on the two most thermodynamically stable surfaces of the cubic phase: {011} and {111}. Calculated properties of these surfaces, including electronic and ionic relaxations, and surface energetics were in good agreement to available experimental data, similar *ab initio* calculations and also to a series of interatomic potential based calculations which we preformed. The relative stability of these two surfaces is in very good agreement to previous calculations and experimental studies.

1 General Introduction

This aim of this work is primarily to demonstrate that Hartree-Fock, and DFT, *ab initio* calculations can be performed on the bulk and surfaces systems of the two oxides: ceria and zirconia.

These materials are employed in a wide range of commercial applications, where they act to catalyse some very important chemical processes, with a potentially far-reaching environmental impact. The specifics of some of these applications, including automobile exhaust catalytic converters and Solid Oxide Fuel Cells (SOFCs), are discussed in greater detail in chapter 3. A detailed understanding about the nature of these materials, including both structural and electronic properties, will be of great interest to attempts to better understand the functioning of these materials.

At the time this work began, back in 1997, computing resources were much more limited than they are today. Previous attempts to examine these materials using quantum mechanical methods had shown severe downsides and were forced to make quite restrictive choices in order to proceed. The limited stability of the phases studies here has also meant that experimental data was quite limited, with the work concentrating more on the overall devices, rather than any one material in particular. In more recent times, environmental concerns have prompted several groups to rethink this attitude, and each day, more and more papers are published on these materials.

The work presented here is aimed at providing more complex studies of these materials with a well-understood base from which to begin, the subtleties of the zirconia phase stabilities discussed in chapter 5, and the comparison of the cubic phase in the two oxides (chapter 4) provide evidence demonstrating the suitability of the optimised basis functions to future studies, and draw important parallels between the high quality *ab initio* calculations and interatomic potential (IP) based studies. The latter shall remain important until such time as thermal effects (dynamics) may be incorporated into quantum mechanical as easily as is possible with many IP molecular dynamics programs.

Chapter 2 discusses the theoretical methods used to perform the various calculations reported in this thesis, including a general background to quantum theory. Chapter 3 discusses briefly some of the commercial applications in which ceria and zirconia are

used. The importance of these applications to our everyday lives, and also to the environment, is the key driving force which all future studies on these materials rely upon, and also helps to provide funding for research such as this reported here.

The remaining chapters discuss some of the results obtained in the course of this research, chapter 4 studies only the cubic fluorite structure which is common to both ceria and zirconia, and helps to establish the parameters needed in order to perform more complex studies in the later chapters. Chapter 5 examines the two non-cubic phases of zirconia stable under ambient pressure, the tetragonal and the monoclinic. In particular, the energetics and electronic features behind the cubic-tetragonal phase transition are examined in much greater detail than previous calculations were able.

Catalytic applications of these materials are very much concerned with the properties of material at a surface, the manner by which the oxide is able to interact with exhaust gases or act as a support for noble metal depositions are of great interest. Chapter 6 therefore provides results from an examination of the bare {011} and {111} surfaces of these materials, chosen as they are believed to be the two most thermodynamically stable surfaces. Chapter 7 provides a final brief summary of some of the more important conclusions which can be drawn from the results presented in this thesis.

2 Theoretical Methods

2.1 A Personal Introduction to Quantum Mechanics...

Quantum Mechanics (QM) is, undoubtedly, a remarkable breakthrough of the last century of scientific research; of comparable importance to Einstein's theory of general relativity. QM represented a fundamental change in the way the world around us is considered, and caused many arguments among the greatest minds of the era. QM even prompted the man who derived the fundamental equations governing its use to state: "I don't like it, and I'm sorry I ever had anything to do with it!" (Erwin Schrödinger).

One of the central controversies surrounding quantum theory is, quite simply: what is light? Isaac Newton suggested, over 300 years ago, that beams of light were actually made from individual tiny particles of light. However this 'corpuscular theory of light' was largely ignored by the majority of scientists in favour of Huygens' wave theories, in which light was considered to be a continuous wave of varying electric and magnetic fields. Further work in the 1800s by Young, Fresnel, Maxwell and Hertz appeared to finally seal the coffin on Newton's particle theory forever – no easy task given Newtons formidable reputation. However, even this wave theory was not able to explain some experimental observations.

At the same time, the assumption that all matter was constructed from individual atoms was being refined in Europe by many, including Boltzmann. He used an atomistic picture of gases, and a statistical interpretation of the more traditional laws of Newtonian mechanics, to explain many properties observed in gaseous systems. His work was not universally accepted, until a paper by (the then unknown) Albert Einstein was published in *Annalen der Physik* in 1905. Einstein actually published three papers in this particular issue: one detailing his theory of special relativity,* the second on the

* Einstein went on to extend this theory to include non-inertial reference frames into his theory of general relativity in 1919

interactions which occur between light and electrons,* and the final one on Brownian motion – which finally established the existence of atoms beyond *any* reasonable doubt.

In the early 1900s, the picture of the atom changed almost daily. Work on radioactive decay by Rutherford and Geiger established that Thompson's 'Christmas pudding' model was clearly wrong – in order to explain their results from alpha-particle scattering, the majority of the atom must be empty space: a pinhead (positively charged) nucleus containing most of the mass of the atom orbited by the negatively charged electrons like the planets orbit the sun seemed to be the best we could get! The Bohr model, as it was known, is still taught in many schools today. This model greatly concerned Rutherford: how were the (negative) electrons and the (positive) nucleus kept apart and the atom not collapse in upon itself? The answer lay in the way in which light interacts with matter.

When an object gets hot, it emits light: as it is heated, a metal rod glows red, then yellow, and finally white before melting into a liquid. The hotter the metal becomes, the more intense the light it emits, and the shorter the wavelength of that light. Maxwell's earlier work had suggested that this light came from the motion of charge carriers, i.e. electrons, which generated electro-magnetic fields given off as visible light. The problem was that classical descriptions of how the electrons would move to generate those fields, gave a very different picture to that actually observed from the metal rod. By analogy to waves on a string,† and the result that the energy of the radiation emitted is directly proportional to the frequency of that radiation, the predicted emission spectrum from a hot object led to an "ultraviolet catastrophe" — a blackbody should produce huge amounts of high frequency (short wavelength) radiation — as there are many more combinations of short wavelengths which can 'fit' into a given length of string than there are long wavelengths! In fact, at higher energies (shorter wavelengths)

* The electron had been discovered by J. J. Thompson just seven years earlier at the Cavendish Laboratory in Cambridge, who then proposed his "Christmas pudding" model of matter – announced at the Royal Institution.

† using a perfect emitter (and absorber) or radiation – known as a "blackbody"

the amount of radiation emitted actually falls to zero – in clear contradiction to the classical prediction.*

This concerned one particular German physicist: Max Planck, who spent the end of the 19th century trying to solve it. He finally found a solution in the summer of 1900 when he applied the equations of statistical mechanics derived by Boltzmann† to the problem – he split the total energy up into n discrete packets. This process is illustrated in figure 2.1, which shows the energy of a particle (E) orbiting a central nucleus versus the equilibrium radius (r) of the orbit; the classical (Newtonian) view of energy is shown by the solid curve, $E(r) \sim f(r^2)$, and our particle may possess any arbitrary amount of energy it chooses. Plank restricted the amount of energy to just those discrete blocks indicated by the crosses, which would restrict the radius of the orbit to a set of permitted values, separated by a 'forbidden band'. This process is known as *quantisation* of the particles energy, with each energy packet called a '*quanta*'.

* although classical theory was able to explain the low frequency end of the spectra quite comfortably!

† Planck actually spent much of his life arguing that Boltzmann's theories were preposterous, as they predicted that (statistically) entropy could decrease, but was highly unlikely to do so – traditional views were that entropy *must always* increase, *never* decreasing in any circumstances. The competition between the two grew so intense that Boltzmann committed suicide (as his career and reputation lay in ruin) just before Planck realised that Boltzmann was right all along. In his final publication before his death, Boltzmann wrote "I write this in the hope that should my theories be proven correct, not too much work will have to be repeated" (Quoted in "*The Historical Development of Quantum Theory*", Volume I, page 16 by Mehra, J. and Rechenberg, H.).

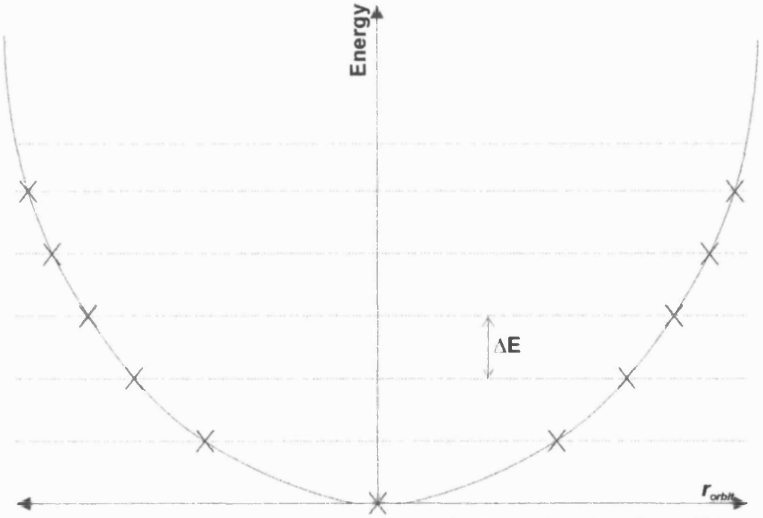

Figure 2.1:A comparison of classical (Newtonian) mechanics, the solid curve, to Planks quantised energy levels (crosses). The crosses indicate Planks permitted energy levels, the solid curve represent the classical energy of an electron in 'orbit' around Bohr's atom. Transitions between the defined energy levels involve absorption or emissions of an energy quanta, having energy ΔE.

A single quanta has an individual energy which is given by equation (2.1) where h is Planck's constant, 6.62608×10^{-34} Js; n is an integer, 0,1,2,...; and ν is the frequency of the radiation. Each 'packet' was considered using Boltzmann's statistical mechanics theories derived originally for the study of gases. Mid-way through the derivation Plank spotted the end result he was searching for, and simply quoted it as the end result: he forgot that (according to classical theories) he needed to re-combine all the discrete quanta into the whole by integrating to reform an energy continuum (the original solid curve in figure 2.1).

$$E = nh\nu \tag{2.1}$$

This was a significant breakthrough, and represented a massive change in scientific opinion. After more than 300 years, Newton's corpuscular theory of light began to raise its head once more – and it fell to Einstein to make the connection.

This simple restriction altered the whole picture of the atom in a way not even Plank could have foretold: now, the electron orbits could only have fixed radii*, and were able

* Bohr calculated the radius of the simplest orbit, that of the isolated hydrogen atom – a value known today as the Bohr radius –(0.5291775Å)

to absorb or emit energy in fixed amounts in order to move between the energy levels – a result which explained the appearance of the atomic emission spectra of Hydrogen gas and helped such a controversial theorem become widely accepted (after much initial resistance) by the scientific community.

2.2 Molecular Orbital Theory

Already in 1905 Planck had theorised that the true nature of light was both particulate and wave-like, a concept which was ratified by Einstein shortly after. However, it was not until 1926 that a coherent mathematical theory was developed by Erwin Schrödinger (1), which explained how this could be so and the consequences of it. Central to this theory lays Schrödinger's wave equation, the time-independent form of which is shown in equation (2.2).

$$\hat{\mathbf{H}}\psi = E\psi \tag{2.2}$$

In the derivation of equation (2.2), Schrödinger postulated that *all* information regarding *each and every* particle present in the system (even in a system as large as the universe itself!) was contained within a single universal function, which he named the "wavefunction", Ψ.

Later, Born suggested a more physical interpretation to Ψ: he stated that the (scalar) quantity $\Psi^*\Psi\partial V$, where Ψ^* is the complex conjugate of Ψ, should be interpreted as the probability that a particle described by Ψ was contained within the element of volume, ∂V: or as it is more commonly known, the charge density - $\partial\rho$ (2). At any point in time, the particle must exist *somewhere* in the system, therefore we can say that the sum of all such probabilities must be unity providing that the wavefunction is normalised (see later), or more mathematically that:

$$\int_V \Psi^*\Psi dV = 1 \tag{2.3}$$

Every experimentally observable quantity is associated with a quantum mechanical operator; the mean value of the operator is the average (expectation) value of the property. There are operators which determine momentum, dipole moments, energy, and every other measurable experimental property. In quantum mechanics, our primary

concern is usually with the energy of a system or particle; the operator which determines energies is known more commonly as the Hamiltonian, $\hat{\mathbf{H}}$, after the mathematician Walter Hamilton who was one of the pioneers of the matrix algebra fundamental to the solution of Schrödinger's wave equation.

The Hamiltonian is given by a summation of all of the independent terms which make up the total energy of the system; i.e. a summation of the individual kinetic ($\hat{\mathbf{T}}$) and potential energy ($\hat{\mathbf{V}}$) operators for every particle considered in Ψ. The resulting operator will be a second order partial differential equation with many variables.*

Because we are primarily concerned with the *electronic* distribution of a system, and as electrons are able to respond almost instantaneously to any changes in the positions of the nuclei, then the electrons can be assumed to be considered as being in equilibrium with the nuclei at all times, with the nuclei themselves being effectively stationary. This is known as the Born-Oppenheimer approximation (3), and can reduce the complexity of the equations quite considerably, since terms involving only nuclear motion can be treated separately in the total Hamiltonian, leaving behind the remainder, which is more commonly known as the 'electronic Hamiltonian', $\hat{\mathbf{H}}^{elec}$.

The electronic Hamiltonian will contain terms involving the kinetic energy of an electron (T_e), the electrostatic interaction between the electron and the nuclei, and the interactions between multiple electrons. The simplest electronic system which can be studied with the Hamiltonian is that of a single, isolated hydrogen atom, containing a single proton-electron pair,† and is shown in equation (2.4). In this equation: h is Planck's constant, m_e is the electron rest mass, q_e is the electronic charge, r is the electron-proton separation, ψ is the electronic wavefunction and E is the corresponding energy of the system.

---

* There must be three variables for each particle considered, due to the three independent coordinate axes (note we have so far neglected electron spin, which is a fourth variable to be considered!)

† The other special case is that of a uniform electron gas, but this is not considered here...

$$\left\{-\frac{h^2}{8\pi^2 m_e}\nabla^2 - \frac{q_e^2}{4\pi\varepsilon_o r}\right\}\psi = E\psi \qquad (2.4)$$

This equation can be solved by writing ψ as the product of a radial function, $R(r)$, and an angular function, $\Theta(\theta)$. Applying the method of separation of variables to this equations produces a series of solutions for ψ, and therefore a value for E. The eigenfunctions obtained contain four parameters, which alter the physical properties of the solutions but can take on a range of values. These parameters are known as the four *quantum numbers* of the hydrogen atom, and are:

- n, the primary quantum number. This can be any positive integer greater than zero, and defines the 'range' of the solution.*
- l, the angular quantum number. This has values $0..(n\text{-}1)$ and defines the shape of the orbital.
- m_l, the azimuthal quantum number. This has values of $0..\pm l$ and defines the directionality of the orbital
- *spin*. This takes on one of two values, $\pm\frac{1}{2}$, and allows a single orbital to hold up to two electrons without violating the Pauli exclusion principle.

These solutions are the well known "atomic orbitals" (AOs), or more commonly known as the *s*, *p*, *d*, and *f* orbitals of an isolated hydrogen atom. In this case, n defines the 'shell' the orbital lies in (**1***s*, **2***s*...); l distinguishes between the *s*, *p*, *d*... orbitals in a single shell; and m_l identifies the individual p_x, p_y, p_z... orbitals, for example.

In larger systems, containing many nuclei arranged into molecular structures, each containing several electrons, complications manifest themselves in two ways: firstly the Hamiltonian operator must contain potential energy terms for the interaction between two electrons. The presence of these terms makes a separation of variables impossible, therefore another mathematical procedure must be used to determine the equilibrium wavefunction. A second problem is that there will exist an infinite number of functions

* The larger the value of n, the more diffuse the orbital is in space.

which are *mathematical* solutions to equation (2.2), however the majority of them do not have properties which we require for a wavefunction. Ψ must be:

- continuous (and also have a continuous first derivative),
- be single-valued,
- tend to zero at infinity
- be "physically reasonable"
- be anti-symmetric on interchange of any two electrons

These concerns are addressed by use of a "variational" technique in solving the Schrödinger equation. This is simply an alternative method of solving a second order differential equation, and is as mathematically valid as a separation of variables method used previously. The variational approach relies on the result that if a function is a solution to equation (2.2) then the derivative of the calculated energy must be zero since the solutions correspond to a minimum energy configuration of the electrons. Therefore, if a function ψ_{trial} can be found which gives little or no change in the calculated energy of the system when changed by the infinitesimal amount $\partial\psi_{trial}$, then ψ_{trial} must be a solution to the many-electron Schrödinger equation.

Since a variational technique does not require a separation of variables, the functional form which the Hamiltonian operator takes is of lesser importance. In addition, it is possible to restrict the functional forms chosen for ψ_{trial} in the variational solution to only those which exhibit the features required for the final solution (save for certain adjustable parameters). In so doing, we determine the best approximation to the "true" solution that is possible, subject to the restrictions imposed on ψ_{trial}. The more degrees of freedom ψ_{trial} is allowed to have, then the closer the variational solutions will be to the "true" solution, however the computational costs incurred will be significantly greater. By imposing no restrictions on ψ_{trial} we again obtain an infinite number of solutions and recover the original problem!

It must be noted that if a function ψ_{trial} is found to solve the Schrödinger equation, then the function $\alpha\psi_{trial}$ must also be a solution, for any arbitrary value of the scalar

multiplier α. A variational technique is not able to assign a value to α. Using the Bohr postulate mentioned earlier, and a little elementary probability theory, the sum of all such probabilities over all space must be unity: a result which can assign a value to α via equation (2.5) below. This is a process known as *normalisation* of the wavefunction.

$$\alpha^2 \int_V \left(\psi^*_{trial} \psi_{trial}\right) dV = 1 \qquad (2.5)$$

All that remains to be defined now is the many-electron Hamiltonian operator and the functional forms of the trial wavefunctions used in the variational procedure. The two most common ways used to construct the Hamiltonian operator are that derived by Hartree (4-6) and Fock (7), or that derived by Kohn and Sham (8). These operators contain identical one-electron terms (i.e. kinetic energy and electron-nuclear interactions) but differ in the way in which each incorporates the two-electron terms. The form used for the resulting wavefunction is dependent on the computer code used in the calculations: the work presented here has been performed using the only commercially available periodic Hartree-Fock code — CRYSTAL (9,10) which uses Gaussian functions to represent the crystalline wavefunctions and is also capable of using both the Hartree-Fock *and* the Kohn-Sham Hamiltonians with similar functions, this will be explained in greater detail in sections 2.3 and 2.4.

2.3 Hartree-Fock Theory

The concepts of Hartree-Fock theory are much simpler to understand when referring to molecular systems (in fact, the Hartree-Fock equations were derived for molecular studies). The work described in the following chapters of this thesis was performed mostly using periodic Hartree-Fock calculations, which are an extension of the molecular Hartree-Fock theory to examine periodic systems. These are covered in greater detail in section 2.3.3.

2.3.1 Molecular Hartree-Fock Theory (Cluster Methods)

In the majority of quantum mechanical calculations, the primary concern is with the chemistry of the system being studied, i.e. the chemical features of the N-electron wavefunction of the system, ψ. The Schrödinger equation can only be solved for the simplest cases of the isolated hydrogen atom, and the uniform electron gas. The most notable result from the hydrogen atom is that we obtain a series of eigenstates which

form the one-electron atomic orbitals denoted as the *s*, *p*, *d*, and *f* orbitals (depending on their angular properties and energy level) according to the observed spectroscopic properties of atomic hydrogen.

In an *N*-electron system, the total wavefunction (Ψ) may be broken down into a product of *N* one-electron atomic or molecular orbitals (MOs),* ϕ_i, as shown in equation (2.6). In the case of molecular systems, the one-electron MOs are in turn often taken to be constructed from a *L*inear *C*ombination of one-electron *A*tomic *O*rbitals (the LCAO method), denoted by φ_i. These φ_i often take a functional form of one of the *s*, *p*, *d*, and *f* AOs described earlier from the isolated hydrogen atom; the whole approach therefore connects the calculated equilibrium wavefunction for an *N* electron system to the more conventional chemical description of the individual AOs on each ion. The intermediate step, constructing a series of one-electron MOs is analogous to the formations of bonds between different species present in the system.

$$\Psi = \phi_1\phi_2\ldots\phi_N \equiv \prod_{i=1}^{N}\phi_i \tag{2.6}$$

$$\phi_i = \sum_{j=1}^{n} c_{ij}\varphi_j \tag{2.7}$$

Each atomic solution must be linearly independent (orthogonal) to the others, i.e. the atomic orbitals must be mutually orthogonal, and also each molecular solution constructed be linearly independent to all others as well.

The atomic and molecular orbitals described so far are purely spatial orbitals. Results from the isolated hydrogen atom indicate that electrons possesses a fourth degree of freedom known as the 'spin'. The Pauli Exclusion principle (11) states that no two electrons may possess identical sets of four quantum numbers, i.e. a spatial AO/MO can hold more than one electron provided that they have different spins, one 'spin-up' ($\alpha_i \equiv \uparrow$), and one 'spin-down' ($\beta_i \equiv \downarrow$).

* Each molecular orbital is one possible solution to the chosen Hamiltonian

A more common representation of the molecular orbitals is to consider instead so-called *spin orbitals* (χ_i): an electron spin orbital is a combination of the (spatial) molecular orbital the electron is within, and the spin the electron has. This procedure creates two distinct spin molecular orbitals from each spatial molecular orbital, if we have $2n$ electrons present, then we must also have $2n$ spin orbitals: $\chi_1 = \alpha\phi_i$, $\chi_2 = \beta\phi_i$.

The wavefunction must also obey the *anti-symmetry principle*:* any interchange of two electrons causes the sign of the wavefunction to reverse (but does not alter its magnitude). If we consider for a moment, a two electron system with electron A in spin orbital $\chi_i(\mathbf{r_A})$ and electron B in spin orbital $\chi_j(\mathbf{r_B})$, then the total wavefunction of the system, $\Psi(\mathbf{r_A},\mathbf{r_B}) = \chi_i(\mathbf{r_A})\chi_j(\mathbf{r_B})$, is clearly not anti-symmetric, since if we interchange electrons A and B:

$$\Psi(\mathbf{r_A},\mathbf{r_B}) = \chi_i(\mathbf{r_A})\chi_j(\mathbf{r_B}) \qquad \Psi(\mathbf{r_B},\mathbf{r_A}) = \chi_i(\mathbf{r_B})\chi_j(\mathbf{r_A})$$

$$\Psi(\mathbf{r_A},\mathbf{r_B}) \neq -\Psi(\mathbf{r_B},\mathbf{r_A})$$

However, if instead we set $\Psi(\mathbf{r_A},\mathbf{r_B}) = \chi_i(\mathbf{r_A})\chi_j(\mathbf{r_B}) - \chi_i(\mathbf{r_B})\chi_j(\mathbf{r_A})$, and interchange the two electrons:

$$\Psi(\mathbf{r_A},\mathbf{r_B}) = \chi_i(\mathbf{r_A})\chi_j(\mathbf{r_B}) - \chi_i(\mathbf{r_B})\chi_j(\mathbf{r_A}) \qquad \Psi(\mathbf{r_B},\mathbf{r_A}) = \chi_i(\mathbf{r_B})\chi_j(\mathbf{r_A}) - \chi_i(\mathbf{r_A})\chi_j(\mathbf{r_B})$$

$$\Psi(\mathbf{r_A},\mathbf{r_B}) = -\Psi(\mathbf{r_B},\mathbf{r_A})$$

As the number of electrons in a system grows, the complexity of this wavefunction will increase dramatically. To simplify the notation, we can represent this wavefunction by the determinant of the 2×2 matrix:†

---

* This feature arises because electrons are identical fermion particles – any interchange of any two electrons must cause a change in sign of the wavefunction. This property is common to all particles which obey Fermi-Dirac statistics.

† A determinant representation is used since an interchange of two rows in a determinant does not change the value of the determinant, only its sign.

$$\begin{aligned}\Psi(\mathbf{r}_A,\mathbf{r}_B) &= \chi_i(\mathbf{r}_A)\chi_j(\mathbf{r}_B) - \chi_i(\mathbf{r}_B)\chi_j(\mathbf{r}_A) \\ &= \begin{vmatrix}\chi_i(\mathbf{r}_A) & \chi_j(\mathbf{r}_A)\\ \chi_i(\mathbf{r}_B) & \chi_j(\mathbf{r}_B)\end{vmatrix}\end{aligned} \tag{2.8}$$

For the more general case of the *n*-electron wavefunction, we use the determinant of the $n\times n$ matrix shown below. This construction ensures that the wavefunction is always anti-symmetric, due to the very nature of matrix arithmetic, and is known more commonly as a *Slater determinant* (12,13).*

$$\Psi(\mathbf{r}_1,\mathbf{r}_2,\ldots,\mathbf{r}_N) = \begin{vmatrix}\chi_1(\mathbf{r}_1) & \chi_2(\mathbf{r}_1) & \cdots & \chi_N(\mathbf{r}_1)\\ \chi_1(\mathbf{r}_2) & \chi_2(\mathbf{r}_2) & \cdots & \chi_N(\mathbf{r}_2)\\ \vdots & \vdots & \ddots & \vdots\\ \chi_1(\mathbf{r}_N) & \chi_2(\mathbf{r}_N) & \cdots & \chi_N(\mathbf{r}_N)\end{vmatrix} \tag{2.9}$$

Now that we have a mathematical relationship describing the formation of the one-electron molecular orbitals from the provided atomic orbitals, we can begin to calculate the energy of the interactions between two of these orbitals, defined in equation (2.10)), and for computational efficiency is generally represented by an $n\times n$ matrix, H_{ij}.

$$H_{ij} = \int_V \left(\psi_i^* \hat{\mathbf{H}} \psi_j\right) dV \equiv \left\langle \psi_i \middle| \hat{\mathbf{H}} \middle| \psi_j \right\rangle \tag{2.10}$$

The primary problem in solving the Schrödinger equation in a multi-electron system is the presence of electron-electron interactions. The Heisenberg uncertainty principle (14) tells us that we can never know exactly the precise location of an electron, at the same time as its velocity; in order to sum the kinetic energies of the electron we therefore lose all information regarding the position of the electron at that instant. The same is true in reverse. To overcome the problem, Hartree-Fock theory uses what is known as a *mean field theory*: rather than considering the electrostatic interactions between two individual electrons at a moment in time, we instead examine the extent of

* The Slater determinant will also have a normalising constant pre-multiplying the determinant, which has been omitted here for simplicity. This normalising constant is equal to $(N!)^{-1/2}$

the interaction between a particular electron and an averaged potential field created by the remaining electrons.

To achieve this, we construct a Hamiltonian-like operator, called the Fock operator $\hat{\mathbf{F}}$, which contains only one-electron terms which can be readily calculated. $\hat{\mathbf{F}}$ can be represented by an $n \times n$ matrix, just as the Hamiltonian can be. The elements of the Fock matrix, F_{ij}, are defined by the set of n differential equations formed from the Schrödinger-like equation shown in equation (2.11).

$$F_i \psi_i = \sum_{j=1}^{n} E_{ij} \psi_j \tag{2.11}$$

The Hamiltonian operator is also reduced to the summation of two separate operators: one containing all terms involving only a single electron, $\hat{\mathrm{H}}_1$ (e.g. electron-nucleus potential energy, kinetic energy), the other containing all terms including two electrons, $\hat{\mathrm{H}}_2$ (e.g. electron-electron potential energy, etc) where $\hat{\mathbf{H}} \equiv \hat{\mathbf{H}}^{\mathrm{TOT}} = \hat{\mathbf{H}}_1 + \hat{\mathbf{H}}_2$. The total energy of the system (with total wavefunction Ψ) is then given by:

$$E^{TOT} = \left\langle \Psi \middle| \hat{\mathbf{H}}^{\mathrm{TOT}} \middle| \Psi \right\rangle \equiv \left\langle \Psi \middle| \hat{\mathbf{H}}_1 \middle| \Psi \right\rangle + \left\langle \Psi \middle| \hat{\mathbf{H}}_2 \middle| \Psi \right\rangle \tag{2.12}$$

It can be shown that in the expansion of the right hand side of the above equation, many of the cross-terms vanish with the end result being that each component can be written as:

$$\left\langle \Psi \middle| \mathbf{H}_1 \middle| \Psi \right\rangle = 2 \sum_{i=1}^{n} H_{ii} \tag{2.13}$$

$$\left\langle \Psi \middle| \mathbf{H}_1 \middle| \Psi \right\rangle = \sum_{i}^{n} J_{ii} + \sum_{i}^{n} \sum_{j \neq i}^{n} \left(2J_{ij} - K_{ij} \right) \tag{2.14}$$

where:

$$H_{ii} = \int \left(\psi_i^*(1) \hat{\mathbf{H}}_1 \psi_i(1) \right) dV_1 \tag{2.15}$$

$$J_{ij} = \sum_{kl} \iint \left(\psi_i^*(1) \psi_k^*(2) \left(\frac{1}{r_{12}} \right) \psi_j(1) \psi_l(2) \right) dV_1 dV_2 \equiv \sum_{kl} \langle ij | kl \rangle \tag{2.16}$$

$$K_{ij} = \sum_{kl} \iint \left(\psi_i^*(1) \psi_k^*(2) \left(\frac{1}{r_{12}} \right) \psi_l(1) \psi_j(2) \right) dV_1 dV_2 \equiv \sum_{kl} \langle il | kj \rangle \tag{2.17}$$

The operator $\hat{\mathbf{J}}$, called the Coulomb operator, can be represented by a $n \times n$ matrix (with elements J_{ij}), while $\hat{\mathbf{K}}$ is the Exchange operator, represented by a matrix with elements K_{ij}. The equations for these operators can be simplified so that the total energy of the system is given by:

$$E^{TOT} = 2\sum_{i}^{n} H_{ii} + \sum_{i}^{n} \sum_{j}^{n} \left(2J_{ij} - K_{ij} \right) \tag{2.18}$$

It is useful at this point to mention that we can define a one-electron orbital energy to be:

$$E_i = H_{ii} + \sum_{j}^{n} \left(2J_{ij} - K_{ij} \right) \tag{2.19}$$

where E_i represents the energy of an electron described by the molecular orbital ψ_i interacting with the bare nucleus, as well as the average potential field due to the remaining $(2n-1)$ electrons.* This definition further simplifies the expression for the total energy of the system to become:

$$E^{TOT} = \sum_{i=1}^{n} \left(E_i + H_{ii} \right) \equiv 2\sum_{i=1}^{n} E_i - \sum_{i=1}^{n} \sum_{j=1}^{n} \left(2J_{ij} - K_{ij} \right) \tag{2.20}$$

* Often, this is instead the potential field due to *all* electrons present in the system – the potential due to the considered electron itself is later subtracted by one of several available schemes, although for the purpose of this discussion I shall ignore this effect.

The Hartree-Fock, Schrödinger-like differential equation follows directly from the above results if we define the elements of the Fock matrix as $F_i = H_i + \sum_j \left(2J_{ij} - K_{ji}\right)$. The various terms in this operator can be better understood if we examine the physical forces they represent:

- H_i — This operator contains all of the one-electron terms present in the Hamiltonian: including the kinetic energy and the interaction between an electron and the nucleus.

- J_{ii} ($\equiv K_{ii}$) — The operator to determine the energy for the Coulomb interaction between the two electrons in the molecular orbital ψ_i (one has spin α, the other has spin β)

- J_{ij} — The operator to determine the energy for the Coulomb interaction between the electron in molecular orbital ψ_i and the electron in molecular orbital ψ_j

- K_{ij} — The operator to determine the *exchange energy* between the two electrons in molecular orbitals ψ_i and ψ_j. This is an energy which arises due to the Pauli exclusion principle and acts to stabilise the spatial separation of two electrons which have the same spin.

Each of these integral terms must be evaluated and then used in the determination of the ground state wavefunction. Since the computational procedure employed used a variational approach to determine the ground state molecular wavefunction, which is described using an LCAO scheme, then all that remains to be done is to determine the values of the coefficients c_{ij} in equation (2.7), which is achieved by means of the Roothaan-Hall equation (15-17), shown in equation (2.21)):

$$\mathbf{FC} = \mathbf{SCE} \tag{2.21}$$

$$S_{ij} = \int \left(\psi_i \psi_j\right) dV_1 \tag{2.22}$$

In equation (2.21), $\hat{\mathbf{F}}$ is the Fock operator, represented by an $n \times n$ matrix (**F**) with elements $F_{ij} = \left\langle \psi_i \middle| \hat{\mathbf{F}} \middle| \psi_j \right\rangle$; **E** a diagonal matrix with elements that are the one-electron orbital energies, E_i ($\equiv E_{ii}$) defined in equation (2.19); **S** is a matrix of elements which are

the overlap integrals between two different one-electron orbitals as defined in equation (2.22); and **C** is a matrix of the coefficients, C_{ij}. This equation can be reduced to the form of a standard eigenvalue equation, which can then be solved using an iterative approach: a trial solution for **C** allows us to determine a trial solution for the Fock matrix, which can then be used to determine a better estimate for **C**, followed by a better estimate for **F**, and so on. There will come a point when our solution for **C** gives a Fock matrix which returns the same coefficient matrix again (within a certain tolerance). The system at this point is said to be *self-consistent*, since the electron distribution is consistent with the potential field which it creates. This iterative process is more commonly known as the *Self-Consistent Field* (SCF) procedure.

2.3.2 Basis Sets

A basis set is simply the set of functions which is used to describe the space that the wavefunction exists in. They are effectively a set of "building blocks" from which we can describe the complex features of the atomic orbitals, the calculated molecular orbitals, and the total wavefunction itself.

Ideally, an atomic basis set would be constructed from an infinite set of (orthogonal) functions, allowing it to represent *exactly* the electronic configuration of any "real world" system defined in the same space that the basis functions describe. However, instead we need to approximate this ideal basis with a finite number of functions; the size chosen by balancing several key factors including:

(1) the accuracy required of the calculations,

(2) the functional form used in the basis,

(3) available computational resources,

(4) the property being examined,* and

(5) the nature of the system under study.

* For example, calculation of dipole moments requires extensive polarisation functions to be included in the basis set, while a geometry optimisation of the same structure may not.

Generally, unless there are overriding concerns, the functional form used for the atomic basis is chosen to best suit the system under study; the challenge lies in balancing the accuracy required of the calculations with the resources available (known as the 'cost' of the calculations). An extensive basis set containing a great many functions would provide very accurate results, but would also require a substantial amount of time and space to provide them!

Now that we have established a framework for solving the Schrödinger equation in a many-electron problem, all that remains is to define the set of one-electron atomic orbitals, ϕ_i, to be used in the calculations – i.e. the "basis set".

It is generally accepted that the solutions derived by Slater as the exact solutions for the hydrogen atom (16,17) are of the best type, and are known as Slater-Type Orbitals (STO). A STO has the form illustrated in equation (2.23), with the variables A_i and α_i, however it is found that if such a function is used to represent an atomic orbital then many of the integrals which we need to calculate become impossible to perform analytically, only numerically. In addition, overlap integrals involving atomic orbitals centred on different atoms become very costly to evaluate.

To simplify the mathematics, a series of N Gaussian functions, called a *Gaussian contraction*, is used to form a Gaussian-Type Orbital (GTO) which best approximates the STO, shown in equation (2.24)) with variables B_{ij} and β_{ij}.

$$\phi_i \equiv \left(A_i e^{-\alpha_i r}\right)\Theta(\theta,\varphi) \tag{2.23}$$

$$\phi_i \equiv \left(\sum_{j=1}^{N} B_{ij} e^{-\beta_j r^2}\right)\Theta'(\theta,\varphi) \tag{2.24}$$

Gaussian functions have the advantage that integrals involving the atomic orbitals can be calculated analytically, however due to the difference between the shape of a Gaussian and a STO we need to consider more Gaussian's than we would STOs. GTOs do have certain problems associated with them, the most obvious is the fact that a GTO tends to the value of B_{ij} at the origin while a STO tends to A_i (known as a "cusp"). In addition, a GTO also tends to zero much faster than a STO does. This is rarely a problem in practice, however: the *chemistry* of a particular system is dictated by the valence electrons, which are adequately described by GTOs.

The standard nomenclature for a GTO is to label the basis set as "STO-*n*G", where *n* is the number of Gaussian functions used in the contraction to represent the STO (the same as the value of *N* in equation (2.24)). If the chosen representation contains only enough orbitals to accommodate the total number of electrons on the atom, the basis set is said to be "*minimal*"; for example, a minimal basis set for hydrogen or helium contains only the 1*s* orbital, while for lithium it would contain the 1*s* and 2*s* orbitals. Minimal basis sets are quick and simple to perform calculation on. However, they do have one major inadequacy: atoms at the end of a row (in the periodic table) have the same number of basis functions as those at the start of the row, despite the fact that they have more electrons. This feature leads to a large anti-symmetry in the basis set, and is especially problematic when studying oxygen or fluorine-containing compounds with minimal basis sets.

These problems can be overcome by using more sophisticated, and complex, basis sets. The simplest approach is to increase the number of Gaussian contractions used to describe each orbital. A basis set using two contractions is called a "double-zeta" basis set, and the same applies to triple-zeta basis sets.* The innermost Gaussian contraction is termed the "contracted" function, while the outermost is termed the "diffuse" function. The overall orbital is a linear combination of the two functions.

The problem with using such a basis set is that it can quickly become rather expensive, which may be counteracted by representing the valence orbitals by double-zeta basis functions and leaving the core orbitals represented by a single Gaussian contraction. This procedure generally works quite well since it is only the valence electrons which are involved in the chemical description of the system, and therefore need to be described most accurately. Such a basis set is said to be of a "*split-valence double-zeta*" quality, and is represented in the form *j-kl*G — where *j* is the number of Gaussian contractions used to represent the core orbitals (one for each orbital), *k* is the number of Gaussian's used to represent the contracted valence orbitals and *l* is the

* These terms are really only applicable to molecular studies, in periodic codes such as CRYSTAL the basis set usually only have a "double-zeta quality". In practice, the basis functions of neighbouring ions complement each ions basis set so that triple-zeta (or higher) basis functions are rarely necessary.

number used to represent the diffuse valence orbitals.* One other important extension which can be made to the basis set is to include *polarisation functions*, which are orbitals that have an angular quantum number one larger than the outermost valence orbitals (i.e. *p* orbitals for hydrogen, or *d* orbitals for the heavier elements).

Another very effective simplification which we can make is to remove the core electrons from the basis set completely, and instead represent their interaction with the outer valence electrons by an averaged potential field surrounding the nucleus, known as an Effective Core Potential (ECP). This assumption generally works well since the core electrons are not involved in the chemical bonding of the system and can greatly reduce the cost of the calculations. There are two types of ECP available: a small-core ECP and a large-core ECP. Small-core ECPs are preferable since they leave more electrons for explicit study in the calculations and therefore recreate the chemistry of the system well, but for very expensive calculations a large-core ECP may have to be used. A large-core ECP describes all electrons up to the noble gas before the ion under consideration by the potential field. For example, in zirconium, a large-core ECP describes all electrons up to Kr while a small-core ECP describes electrons up to Ar.

2.3.3 The Pseudopotential Approximation

It is important to realise that different expressions for the basis functions can be implemented in the same QM code. It is, in fact, even possible to combine multiple functional forms of the basis functions to exploit the benefits of each. For example, plane waves are suited to describe highly delocalised electronic systems, but are unable to adequately represent the more localised regions of electron density which surround the nucleus of an ion. In this case, an accurate description would require several million functions, at great computational cost. To counteract this difficulty, atom centred functions can be included in the basis to represent the core regions of an ion, while plane waves are used to cover inter-ionic regions where electrons are delocalised (subject to the constraint that the electron density be continuous across the boundary between the two functional forms). This is illustrated in figure 2.2

* A split-valence triple-zeta basis set would have the form *j-klm*G

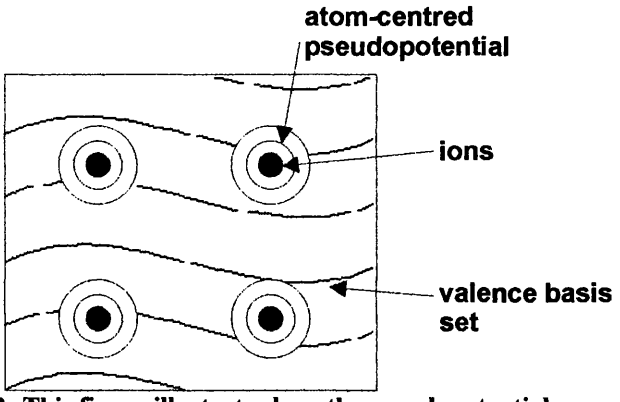

Figure 2.2: This figure illustrates how the pseudopotential approximation works. The use of a potential field localised around the nucleus allows core electrons to be represented separately to the valence basis functions. A similar technique is used in Linear Augmented Plane-wave (LAPW) calculations to represent core electrons differently to valence electrons.

If a system contains heavy ions, it is well known that one simple way to dramatically reduce the cost of the calculations is to use the 'pseudopotential (PP) approximation'. In a study of catalysis, we are primarily concerned with the *chemistry* of the system, which depends mostly upon the valence electrons; electrons lying deep in core states are generally unimportant and, particularly on heavy ions, constitute a significant proportion of the total number of electrons present in a system. For this reason they are usually not included explicitly in *ab initio* calculations. Instead a potential field surrounding the nucleus of the ion is used, which is designed to represent the electrostatic repulsion effect the core electrons would exert on their outer neighbours and thereby reduce significantly the overall cost of the calculation without sacrificing the chemical description of the material. This potential field is known as a *pseudopotential* (PP), or alternatively as an *Effective Core Pseudopotential* (ECP).

In the work described in this thesis, we chose to use the Hay and Wadt small-core pseudopotentials, as they have been successfully used in similar studies of metal oxides (18,19), and are available for both Ce and Zr ions. Equation (2.25) shows how the electrostatic potential energy (W_{PP}) is calculated for the Hay and Wadt family of pseudopotentials; in which Z_N is the effective nuclear charge (the actual nuclear charge minus the number of electrons which the pseudopotential represents), P_l is an operator connected to the angular quantum number of the orbitals replaced; M, n_k, α_k, M_l, n_{kl}, c_{kl}, and α_{kl} are the atomic pseudopotential parameters which define the pseudopotential.

$$W_{PP} = \left(-\frac{Z_N}{r}\right) + \left(\sum_{k=1}^{M} r^{n_k} C_k e^{-\alpha_k r^2}\right) + \left(\sum_{l=0}^{3}\left[\sum_{k=1}^{M_l} r^{n_{kl}} C_{kl} e^{-\alpha_{kl} r^2}\right] P_l\right) \qquad (2.25)$$

2.3.4 Periodic Hartree-Fock

Until now we have examined only molecular systems. There are, however, a great many systems which are not molecular in nature, the most obvious being crystalline lattices that are periodic in three dimensions, or surface structures with two-dimensional periodicity.

The description of Hartree-Fock theory given so far is applicable only to molecular systems. For this reason, molecular Hartree-Fock theory was extended to include also crystalline materials, and is implemented in the QM code CRYSTAL (9,10).

Periodic Hartree-Fock theory is identical to the molecular case in many ways, with only a few subtle differences, the greatest one between the two techniques is the functional form which the atomic orbitals assume: in the periodic scheme the atomic orbitals are actually Bloch functions, $\varphi_\mu(\mathbf{r})$, shown in equation (2.26) where the sum over **g** indicates a summation over all reciprocal lattice vectors, while the atom centred atomic orbitals $\varphi_\mu(\mathbf{r})$ are a series of Gaussian contractions as in the molecular case. A Bloch function is simply a representation of the basis set in reciprocal space, and this function has the same periodicity as the crystal lattice; these features mean that by using Bloch functions to solve the Hartree-Fock equations we are able to fully exploit all translational symmetry operation present in the system.

$$\phi_\mu^{\mathbf{k}}(\mathbf{r}) = \sum_{\mathbf{g}} \chi_\mu^{\mathbf{g}}(\mathbf{r}) e^{i\mathbf{k}.\mathbf{g}} \tag{2.26}$$

$$\chi_i(\mathbf{r},\mathbf{k}) = \sum_\mu c_{\mu i}(\mathbf{k}).\varphi_\mu(\mathbf{r},\mathbf{k}) \tag{2.27}$$

The resulting crystalline spin orbitals, $\chi_i(\mathbf{r},\mathbf{k})$, see equation (2.27), are the periodic equivalent of the molecular orbitals in molecular Hartree-Fock theory, and are again formed using a LCAO approach (although this time the atomic orbitals, $\varphi(\mathbf{r},\mathbf{k})$, are replaced by the Bloch functions of equation (2.26)). The coefficients $c_{\mu i}$ of the crystalline orbitals are again calculated through the Roothaan-Hall equation (15-17).

The Roothaan-Hall equations are solved self-consistently, as they were in the molecular scheme. These equations would ideally be solved at every allowed *k*-point in the first Brillouin zone, as a different solution is obtained from every *k*-point; in practice, however, reciprocal space is sampled by a finite grid of *k*-points with the

solution at intermediate points being determined by extrapolation of solutions calculated. The first Brillouin zone is the irreducible portion of reciprocal space; a grid of *k*-points is generated which spans the whole volume of the irreducible zone. Each point is represented by a unique **k**-vector, and these points are weighted according to the Pack-Monkhorst scheme (20); the Roothaan-Hall equations are then solved at each *k*-point so that the shape of the bands across the whole Brillouin zone can be determined (which is not a concern in molecular studies).

2.4 Density Functional Theory

Density functional theory (DFT) is an alternative approach for constructing the Hamiltonian used in solving the Schrödinger equation for many-electron systems. The primary difference between DFT and Hartree-Fock theory is the way in which exchange and correlation energies are determined: Hartree-Fock derives an exact expression for the exchange operator while totally neglecting the correlation contribution. DFT schemes, on the other hand, use approximate expressions for both exchange and correlation operators. This technique is coded into a great many computational programs, and is often the technique of choice in many studies. However, since the component energy terms are only approximate there will always be doubt regarding the quality of the results: the exchange energy may be calculated accurately while the correlation may be much less so, or vice versa. In some cases, it is found that a fortuitous cancellation of errors occurs in DFT, with errors in the exchange energy being cancelled out by errors in the correlation energy, leading to calculated results that are on a par with experiment.

The first implementations of DFT used a "Local Density Approximation" (LDA): the functionals used to calculate the exchange and correlation energies were functions of the local electron density only. These functionals are derived mathematically from the case of a uniform-electron gas — an infinite system containing electrons of uniform charge density ρ. In a crystalline system, the irreducible cell is divided into a grid of points and the charge density determined at each point; the exchange and correlation energies can then be calculated by comparison to this free-electron gas model and then summed over all points considered in order to determine a "total energy". LDA schemes generally underestimate the experimental lattice parameter by ~2%, and the band gap by as much

as 50%. In this thesis, the LDA functionals proposed by Perdew and Zunger (21-24) were employed.

To improve the agreement of LDA calculations to experiment, the functionals employed were made more complex: in particular the exchange and correlation functionals were assumed to be functions of *both* the local charge density *and* the local charge density gradient. New and improved functionals were derived in this way and are called a "Generalised Gradient Approximation" (GGA). Their application to solid-state systems can either underestimate or overestimate experimental observables depending upon the system under study, and the exact functional chosen – the GGA calculations performed in this thesis used the Perdew-Wang functionals (22-25).

2.5 Problems with Hartree-Fock Theory

In Hartree-Fock theory, the total wavefunction of a particular system (Ψ) is represented by the product of N one-electron molecular orbitals (ϕ_i) (equation (2.6)). In equation (2.7) we saw further that each of these N molecular orbitals was to be represented using a linear combination of one-electron atomic orbitals (φ).

When Hartree-Fock theory is implemented into a computational code, we provide a basis set of atomic orbitals and calculate from this a series of one-electron molecular orbitals. Rather than calculating a set of molecular (crystalline) functions from which the total wavefunction is represented (by equation (2.6)), instead we simple take the single solution which provides a system of minimum energy, and discard all others.

This approach is known as a *single-determinant solution*, because we have calculated a single set of possible eigenstates (of the Hamiltonian matrix) to provide a single solution of minimum energy.

An additional problem is the total elimination of the energy contribution due to electron correlation: the mean field approximation used in Hartree-Fock theory considers each electron moving in the average potential field created by the other electrons. Electron correlation arises because the motion of a particular electron is dependent on the relative motions of the other electrons at any moment in time. The slightest change in the direction (say) of one electron causes the motions of all the other

electrons to adapt. With a mean-field approximation, these effects cannot be incorporated into our description of the system.

Hartree-Fock theory does, however, provide an exact expression for the exchange energy, at the cost of totally removing the correlation energy. Density functional schemes operate in a slightly different way, by providing analytic expressions based on the total electron density. These expressions can be derived from the uniform-electron gas model and *are* able to include approximate correlation energies, in addition to the approximate exchange energy. In general, the exchange energy is larger than the correlation energies by an order of magnitude, so often the Hartree-Fock approach is perfectly adequate (especially in systems where electron correlation effects are low).

Correlation acts as a binding energy, i.e. it must be subtracted from the exchange energy and will be larger for more compacted systems. Inclusion of correlation effects into Hartree-Fock calculations, either *a posteriori* or self-consistently, cause a reduction in the pure Hartree-Fock minimum energy lattice parameters, band gaps, and a corresponding increase in the elastic constants.

2.6 Hybrid HF-DFT Schemes

HF and DFT calculations often provide errors in opposite directions when compared to experimental data : when one scheme overestimates, the other often underestimates. An obvious way of improving the accuracy of the calculations is therefore to combine the HF and DFT components into the same Hamiltonian.

We can achieve this goal in one of two ways: either Hartree-Fock calculations can be complemented *a posteriori* using a correlation-only density functional on the Hartree-Fock equilibrium charge density, to calculate an approximate value of the electron correlation energy. Since this estimate for correlation is added *a posteriori*, then the HF electron density is unable to adapt to the inclusion of the correlation effect – resulting in the modified results overestimating the "rigidity" of the system to external perturbations. Often the pure Hartree-Fock results are preferable to those corrected *a posteriori*, since we are certain where our deficiency lies.

An alternative that is currently becoming increasingly popular is to employ a mixed Hartree-Fock and Density Functional exchange Hamiltonian. Much of the early work

was done in molecular studies by Becke *et al.* (26-28) who developed the B3LYP hybrid scheme using the Lee-Yang-Parr correlation functional (29). Hybrid methods calculate the exchange energy as a combination of the Hartree-Fock exchange and a chosen DFT exchange functional, and then add in the appropriate DFT correlation functional. Such schemes commonly produce results midway between the DFT and Hartree-Fock results, as we should expect, but they are capable of reproducing the experimental band structure much more accurately than either Hartree-Fock or pure DFT calculations are capable of; they also have the added advantage that the exchange energy is determined more accurately by using a proportion of the exact Hartree-Fock value. In this work we have begun to examine the performance of the new B3LYP scheme in zirconia, one of the first applications of the method to the solid-state.

2.7 Geometry Optimisation

The geometry of the materials examined in this thesis were optimised to a state of minimum total energy when calculating equilibrium properties. The primary QM code used in this research (CRYSTAL) permits calculation of the total internal energy (E) of a given system, but it does not currently calculate forces acting on individual species present.* All geometry optimisations must therefore be performed numerically, using a conjugate gradient, or steepest descent approach.

An initial reference geometry is defined for the system and the total internal energy for that configuration, E^0, is calculated (with a single-point calculation). Next, every movable atom is displaced in turn, by a small amount dx along each crystallographic axis in sequence while the other atoms remain fixed in their reference positions. The total energy of the system is calculated at each step from a series of single-point calculations to provide the two energies $E_i(x^0+dx)$ and $E_i(x^0-dx)$, for every degree of freedom, as shown in figure 2.3.

* The total force on an atom is given by $\mathbf{F}^{TOT} = \sum_i F(x_i) = -\sum_i dE/dx_i$ (where x_i are the independent coordinate axes).

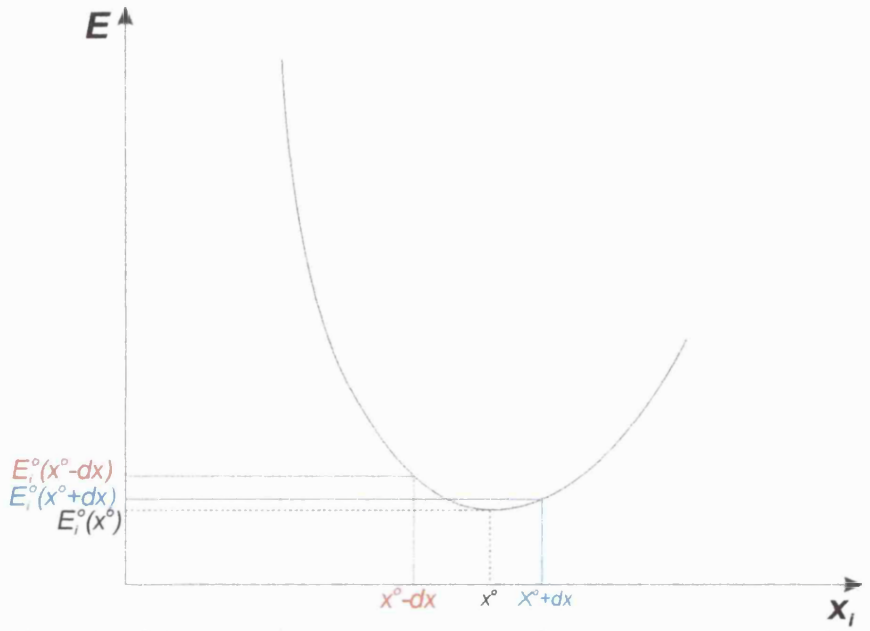

Figure 2.3: Schematic of the energy changes which occur during a numerical geometry optimisation.

These individual energy gradients can be combined to form a total energy gradient for the optimisation as a whole, **G**. All degrees of freedom are then relaxed simultaneously by a displacement vector, **d**, along the combined energy surface constructed from the energy gradient **G**. Once a minimum energy configuration is obtained, the ion configuration forms a new reference geometry, with energy E^1.

As the optimisation progresses, the displacement vector **d** is carried through to the next optimisation step, a process which can greatly reduce the number of optimisation steps needed to reach the optimised geometry. As the geometry reaches its optimal configuration, the energy difference between consecutive cycles slowly decreases: the accuracy of the individual single point calculations is dynamically increased to ensure it remained at least two orders of magnitude higher than this difference at all times.

After k cycles have completed, the value of E^k-E^{k-1} will eventually drop below a given threshold (which was taken to be 10^{-6} Ha in the current series of calculations, or 10^{-7} Ha for higher tolerance calculations), or each component of **G** becomes smaller than 10^{-3} Ha/Å. At this point, the optimisation was considered to have converged, and the configuration of step k is taken as the optimal geometry of the system under study.

This method of geometry optimisation is a 'conjugate gradient' approach, which is an improvement to a standard 'steepest descent' method. The primary difference between the two schemes is that a steepest descent approach does not account for

previous knowledge obtained about the profile of the energy surface: for every step taken, the direction chosen depends only on the energy gradients surrounding that point – the direction taken being that which has the steepest gradient.

In contrast, a conjugate gradient method uses information found from previous steps to reduce greatly the number of future optimisation steps and reduce the inherent "back-tracking" that a steepest-descent approach involves. The idea is to let each search direction be dependent of all other directions searched previously to find the minimum, so that the system is able to converge to a minimum much faster than would be achieved by simply taking the steepest gradient at each step.

The use of this process, although expensive in comparison to internal force-based optimisations, is remarkably powerful and provides optimised configurations in good agreement with experiment.

2.8 Interatomic Potential Methods

Interatomic potential (IP) based studies describe the nature of the bonding between two ions via a simple expression. There are many different forms this expression can assume, in the present work the Buckingham form was used: shown in equation (2.28) where E_{ij} refers to the energy of the two body interaction between ion i and ion j.

$$E_{ij}(r) = Ae^{-\left(\frac{r}{\rho}\right)} - \frac{C}{r^6} \qquad (2.28)$$

The Buckingham model can be used in connection with the '*shell*' model, in which ions are constructed of two components: a central point nucleus – containing the entire mass of the atom (m_N) and having charge X, surrounded by a mass-less shell with charge Y; the total charge on the ion being $X+Y$. The shell is then connected to the core by a spring, with force constant k. The use of a shell model allows the interatomic potentials to attempt to represent the polarisability of the ion, the (negative) shell can move separately from the (positive) core, permitting the ion to possess an overall dipole moment which a non-shell model is not able to do. Ion-ion interactions are modelled through the interaction of shells on neighbouring ions through the Buckingham equation.

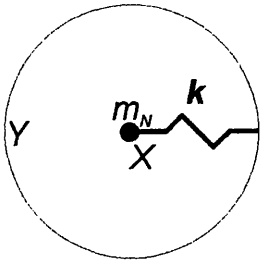

Figure 2.4: The shell model of an atom. The meaning of the symbols is given in the text.

The ions in the structure are then relaxed at constant pressure, to allow the bulk unit cell dimensions to change, to minimise all internal forces between the ions. The energy of the minimised configuration is then easily calculated. The low cost of IP calculations makes them ideal for studying complex systems with low symmetry, such as supercell defect clusters, or low index surface structures. In addition, kinetic effects may be included into the calculation through use of a harmonic-oscillator approximation in lattice dynamics simulations.

A 'potential set' is a collection of all parameters needed in order for a particular ion to be included into an IP calculation. The parameters are usually generated empirically, by fitting the Buckingham equation to experimental observables – often the lattice parameter, ion positions and the independent elastic constants (or bulk modulus), as these are the most readily available properties. The results of *ab initio* calculations can also provide data for use in improving the available potential sets, since the same quantities can be calculated for a wide range of systems in various configurations.

2.9 Surface Modelling

In a simulation, a surface is simply a two-dimensional version of a three-dimensional crystal, with a surface normal along a particular crystallographic direction. Generally, we can extract a 'slab' of material, infinitely repeated in two-dimensions, and with a finite thickness in the third dimension from our crystal structure quite simply. Calculations using this cleaved surface slab will be significantly more expensive than the bulk crystal and increase rapidly as the slab thickness is increased, because the number of symmetry operators present in the slab is less than that of the bulk, and also the number of atoms in the crystallographic unit cell has increased.

In a computational code, there are several ways in which the surface itself can be represented internally.

(1) Construct a local cluster of ions arranged in the chosen surface configuration, surrounded by a periodic representation of the remainder of the surface structure, and proceed as in the three-dimensional cluster calculations.

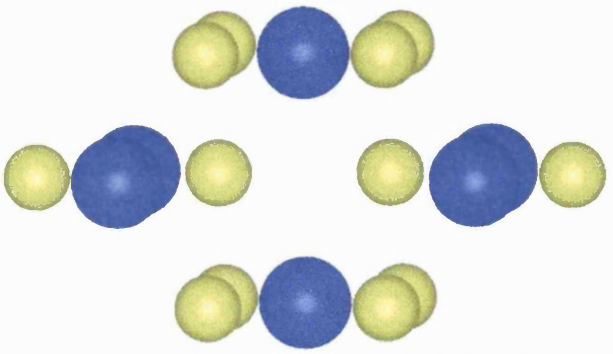

Figure 2.5: Graphic illustrating the cluster method of surface modelling. The cluster is embedded in a grid of point charges to reproduce the electrostatic effects of the crystal.

(2) Construct a block of material that represents the surface under study, which is contained within a three-dimensional unit cell repeated to create a family of two-dimensional slabs separated by vacuum in the third dimension. The size of this vacuum needs careful optimisation to ensure that the slabs do not interfere with one another.

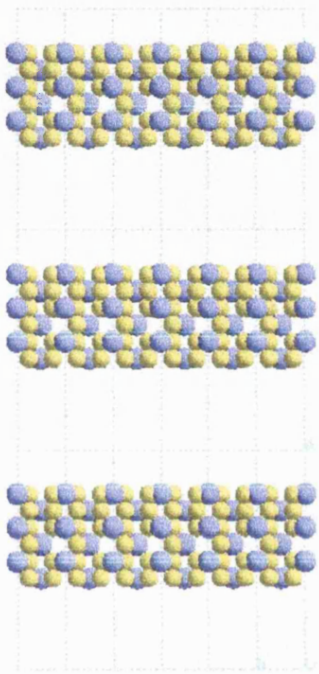

Figure 2.6: Graphic illustrating surface model used in CASTEP. A three-dimensional unit cell is built which creates a series of parallel surface planes, separated by vacuum.

(3) The two-dimensional surface can be cleaved from the three-dimensional crystal and subsequent calculations made only in two-dimensional space.

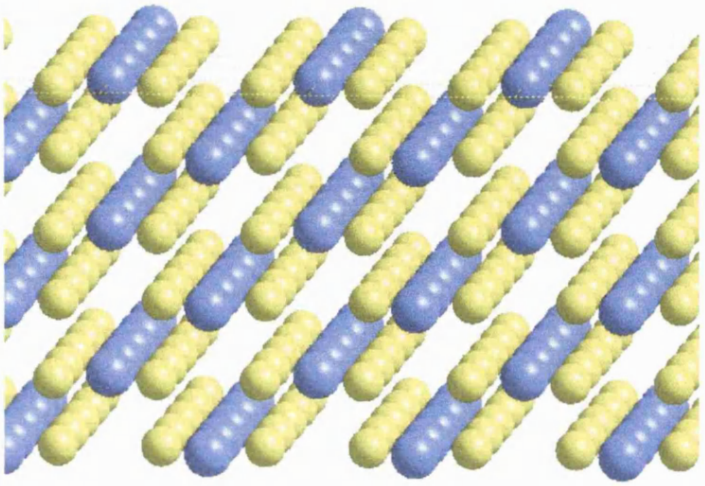

Figure 2.7: Graphic illustrating the two-dimensional surface model used in CRYSTAL. The slab has a finite thickness in the third dimension.

The first of these methods is used in molecular cluster studies, such as the calculations reported in section 4.4.2 which made use of the Gaussian[94] code (30); the second is generally used in calculations employing plane-wave basis functions. If we cleave a general crystal along the {*hkl*} planes, we can create one of two basic surface types, illustrated in figures 2.8(a) and (b), depending on the types of ions present and their local arrangement in the crystal. Figure 2.8(a) shows a surface constructed from layers of equally charged ions, where each layer in the surface is electrically neutral. Surfaces of this type can have any thickness we desire as the resulting slab (as a whole) satisfy the two requirements that they must be (1) electrically neutral and (2) have no overall dipole moment acting across them.

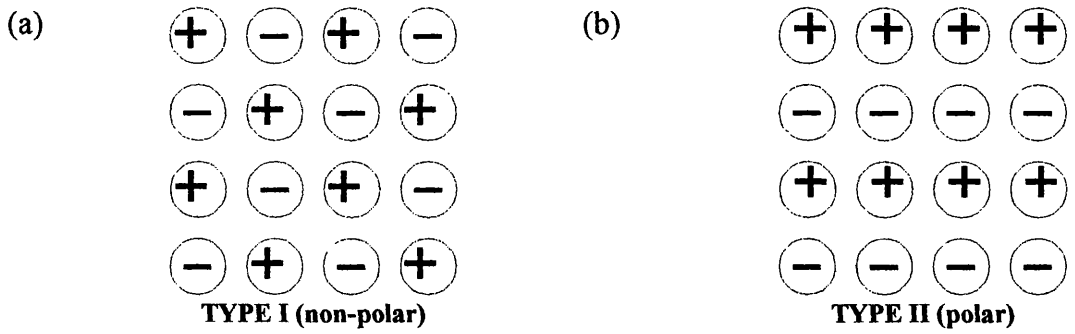

Figure 2.8: Possible surface types created from cleaving a three-dimensional crystal. (a) Surfaces constructed from individually neutral atomic layers; (b) Surfaces constructed charged layers, where a series of layers defines a (repeating) neutral unit

Surfaces of the type shown in figure 2.8(b) however, are not; in this case each layer itself is not electrically neutral. We clearly cannot choose an arbitrary number of atomic layers in this situation since the resulting slab is likely to possess a large dipole moment acting across it, which would act to destabilise the ions in the slab. Figure 2.9 illustrates two methods of removing this dipole, the first in figure (a), creating a *symmetrised* slab, involves constructing a neutral repeating unit from adjacent layers of material. By constraining the slab to contain a whole number of these blocks, the resulting slab will not have an overall dipole moment. The second method in figure (b), creating a *reconstructed* slab, involves selectively removing ions from the upper and lower surfaces to cancel out the total dipole moment. There is a third method which can be used, but which is not covered here, which is to hydroxylate the surface ions and cancel out the slabs overall charge.

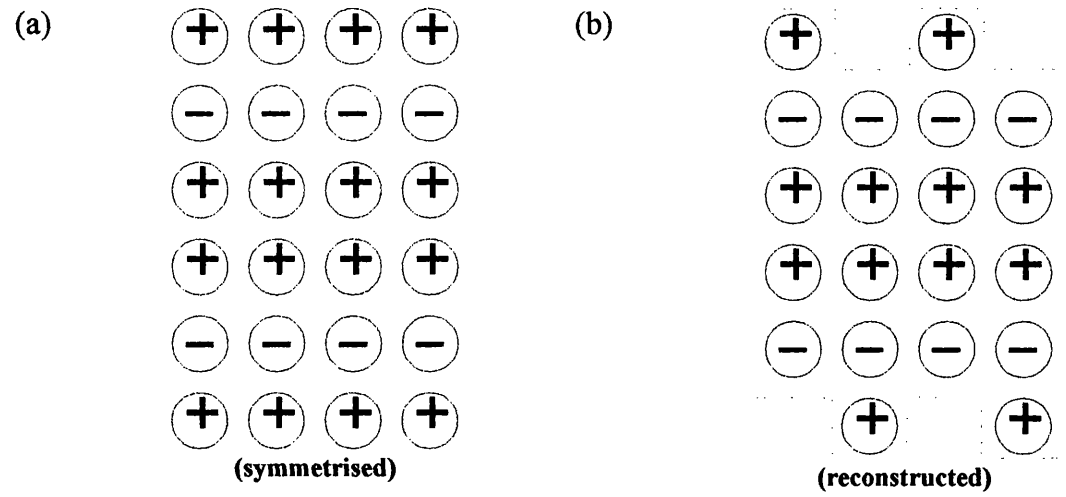

Figure 2.9: Ways of neutralising slabs with a non-zero dipole moment.

For any surface, we have defined the surface energy ($E_{surface}$) of that surface as shown in equation (2.29); where E_{slab} is the energy calculated for the slab, $E_{crystal}$ is the energy calculated for the perfect three-dimensional crystal, and A is the surface area of the cleaved slab. This equation then gives us the energy, per unit area, required to cleave the surface from the perfect bulk crystal.*

$$E_{surface} = \frac{E_{slab} - E_{crystal}}{2 \times A} \tag{2.29}$$

After cleavage of the prefect crystal, it is often possible to reduce the total energy of the slab by relaxing ions away from the positions they occupied in the bulk material. The surface energies corresponding to such slabs are referred to as *relaxed* surface energies. In order to keep the calculations affordable, only ion relaxations which did not destroy symmetry operations were allowed in the current work. Both the relaxed and unrelaxed surface energies for the various slabs studied are reported in sections 6.1 and 6.4.

The model employed in the IP study to represent a surface uses a two region partition of the system: ions near the surface are attributed to region I, and are fully relaxed to

* The factor of two arises because the cleaved slab actually has two surfaces, an upper and a lower face!

minimise the internal energy; ions further away from the surface form region II, and are fixed to their lattice positions. Region II represents the bulk continuation of the surface, and creates the correct embedding forcefield in which region I ions move. Given the relatively low cost of IP calculations, no constraints were imposed on the ionic relaxations, which could therefore include symmetry-breaking displacements. The results showed however that such relaxations were energetically unfavourable, validating the choice of a constrained relaxation in the QM calculations.

2.10 Elastic Properties

The calculated lattice parameter depends on the position of the minimum of the energy surface described by the combination of basis functions and Hamiltonian: if the experimental and calculated a_{cub} agree closely, then the theoretical energy surface has a minima localised in approximately the correct location, which however does not necessarily imply that overall energy surface is the same as the experimental one – figure 2.10 illustrates this point. An experimental energy surface is shown (in two dimensions) by the solid line, alongside two distinct theoretical descriptions of that surface: Theory A (dashed line), and Theory B (dotted line). From this figure, it is clear that neither theory provide an accurate description of the overall energy surface, even though both give the same energy minimum as experiment. Any correct theoretical energy surface must also have the same curvature around the minimum as the experimental surface.

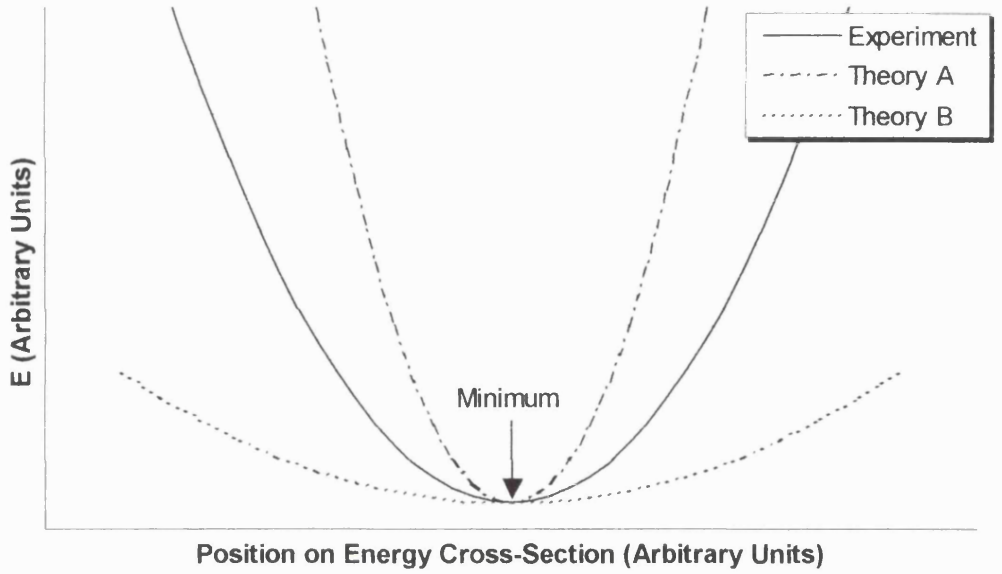

Figure 2.10: Schematic illustrating the importance of correctly reproducing the curvature of the energy surface around the minimum.

In general, the elastic constants of a general anisotropic material form a forth rank tensor: C_{ijkl}, having 21 independent coefficients. By application of the Voigt convention, which separates the strain tensor into translational and rotational components this can be reduced to just two indices: known as the Voigt indices C_{ij}.

The procedure for determining the independent elastic constants varies between actual computational code used: many are able to work directly with the first (and second) derivatives of the energy as this is how the majority of geometry optimisers function (the force acting on a particular atom is given by the energy gradient surrounding it). The CRYSTAL code however, used extensively throughout this thesis, is not able to do so.

Instead, the crystallographic unit cell is deformed by application of an external stress tensor, which preserves the total volume of the unit cell but alters its shape accordingly. The magnitude of this external stress is then altered, the resulting change in internal energy of the cell being related to the value of the elastic constant modelled by the

applied distortion. In the cases examined here, the change in energy is expressed as a Taylor series, below in equation (2.30):*

$$E(\varepsilon_1,\cdots) = a + b\delta^2 + c\delta^3 + \cdots \qquad (2.30)$$

A clear account of the theory behind this process is documented in the CRYSTAL user manual (9). For reference, the necessary stress tensors for calculation of the C_{11}, C_{12}, C_{44} and the bulk modulus, B, are given below, which form the complete set of independent elastic constants of cubic systems, like ceria and cubic-zirconia. In these equations, V is the volume of the primitive cell (since for cubic systems, the primitive unit cell contains one formula unit).

C_{11} $\quad \varepsilon = \begin{bmatrix} \delta & 0 & 0 \\ 0 & 0 & 0 \\ 0 & 0 & 0 \end{bmatrix}$ $\quad C_{11} = 2b/V$

C_{12} $\quad \varepsilon = \begin{bmatrix} \delta & 0 & 0 \\ 0 & -\delta & 0 \\ 0 & 0 & 0 \end{bmatrix}$ $\quad C_{11}\text{-}C_{12} = b/V$

C_{44} $\quad \varepsilon = \begin{bmatrix} 0 & \delta & \delta \\ \delta & 0 & \delta \\ \delta & \delta & 0 \end{bmatrix}$ $\quad C_{44} = b/6V$

B $\quad \varepsilon = \begin{bmatrix} \delta & 0 & 0 \\ 0 & \delta & 0 \\ 0 & 0 & \delta \end{bmatrix}$ $\quad B = 2b/9V$

The bulk modulus is the single most representative quantity of all the elastic properties. It can be determined as mentioned above, or from the fact that in cubic

* The Taylor expansion of the energy as a function of the applied strain has no term proportional to δ, this is because the elastic constant must be calculated for a cell in equilibrium; the term proportional to δ gives the gradient of the energy acting on the atom. If this were not zero, there would be a net force acting on the atom and the system is not in equilibrium.

systems: $B = (C_{11}+2C_{12})/3$; there are also many more sophisticated equations of state reported in the literature (31) which can be used to provide a more detailed interpretation of the energy/strain relationship than a simple parabola, as used above. Results from all three sources will be quoted in this thesis, although as the above methods are valid only for cubic systems (and the calculations become much more complex for non-cubic crystals), we shall often only report figures from the more detailed equations of state, which are dependent only on the calculated internal energy as a function of cell volume.

The calculation of these elastic properties not only demonstrates that our *ab initio* model provides an accurate description of the true energy surface of a material, and allows comparison of calculated properties to those determined experimentally, but they are also instrumental in developing improved interatomic-potential parameters for future studies beyond the capabilities of quantum mechanical codes.

3 Commercial Applications

The following chapters aims to give a brief account of some of the more commercially attractive applications of ceria and zirconia, not as cheap filler materials, but as active catalysts in their own right. Also, it shall discuss some of the more pertinent questions raised by experimental studies, and demonstrate the ways in which theoretical simulations can assist in providing the answers.

Most applications which make use of the catalytic properties of ceria and zirconia rely primarily upon the extremely high oxygen ion conductivity that they possess. An important feature of this conductivity, is that it can be controlled and carefully designed to a particular level simply by doping with various amounts and proportions of metal oxides. By adding a lower valent oxide such as Y_2O_3 or CaO, in order for the material to maintain overall charge neutrality then vacancies must be introduced onto the oxygen sub-lattice. Here, two host metal ions, M(+IV), are replaced by Y(+III) ions; this introduces a (-II) charge discrepancy which can be compensated for by removal of a single oxygen ion. In the infamous Kroger-Vink notation this can be expressed by equation (3.1).

$$2M_M + O_O \rightarrow 2Y'_M + V_O^{\bullet\bullet} \qquad (3.1)$$

If instead, a higher valent metal oxide is added, we must introduce oxygen ions into interstitial sites to counter the higher positive charge of the dopant metal ions, as shown in equation (3.2). In this situation the material can act as an oxygen source.

$$2M_M + V_{INT} \rightarrow 2X_M^{\bullet} + O''_{INT} \qquad (3.2)$$

3.1 Automobile exhaust three-way catalytic converters

Three-way catalytic converters (TWCs) have been fitted to the exhausts of new cars in Britain for several years now. They remove harmful pollutants present in the engine exhaust fumes (e.g. NO_x, CO, and uncombusted fuel (32,33), forming CO_2, NO_2 and water as the reaction products. The conversion of exhaust fumes occurs naturally at a very slow rate, although it was found that by passing the exhaust fumes over certain noble metals (such as platinum or rhodium) then the speed and efficiency of the conversion was significantly improved.

A typical catalytic converter has a honeycomb cordierite shell, creating the maximum surface area possible to interact with the exhaust gases. This shell is then coated with a mixture of alumina and ceria; a noble metal (often Pt) is then deposited onto the surface, see figure 3.1. An alumina support is used to improve the cohesion of the Pt droplets to the cordierite shell and experiments revealed that the efficiency of the converter was improved even further when small quantities of ceria were added. The present understanding why this occurs is that the ceria allows the support to act as an oxygen reservoir (as explained above) and this ensures that the environment surrounding the Pt droplets is always optimal for the conversion to occur.

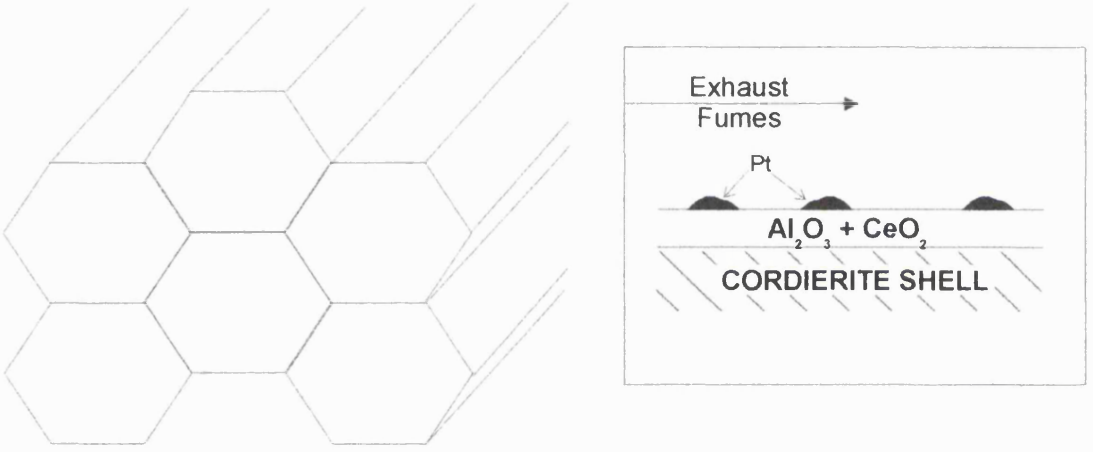

Figure 3.1: Schematic of an Automobile Exhaust Three-Way Catalytic Converter, illustrating the honeycomb cordierite shell of the device, and a closer view of the surface of the shell.

Catalytic converters operate most efficiently within a specific temperature range, usually between 250°C and 900°C, when the temperature of the converter is sustained by the exothermic conversion reactions occurring within it. The time taken for this condition to be reached is known as the "*light-off time*", and it is also during this period when the engine is generating the largest quantity of harmful products. Clearly, a reduction in the length of the light-off time is desirable; it was observed that by adding ceria to the Pt support, the light-off time decreased by an appreciable amount.

3.2 Solid Oxide Fuel Cells

SOFCs convert chemical energy directly into electrical energy, bypassing the highly inefficient conversion to mechanical energy which most electricity generation methods currently in use employ (34). It is a very simply concept: a hydrogen-rich fuel is passed over an anode, and a gaseous oxygen source passed over the cathode. These two

electrodes are separated by a solid electrolyte, yttria-stabilised cubic-zirconia, although Ga-doped ceria can also be used.

An yttria-stabilised cubic phase is employed for two main reasons: most importantly since yttrium has a formal charge of +III, in order to maintain charge neutrality oxygen vacancies are introduced into the material, increasing the materials ionic conductivity. Secondly, a stabilised cubic phase is used is to ensure that no phase changes occur as the cell is heated up to its operating temperature (approximately 1000°C). If any phase changes occurred, the cell volume would inevitably change and after several thermal cycles could result in the anodic material spalling away from the zirconia electrolyte, and the cell would then no longer function.

At the anode, the fuel oxidises oxygen ions incorporated into the lattice - releasing electrons and increasing the local oxygen vacancy concentration. These electrons then travel via an external circuit towards the cathode (35); the difference in oxygen vacancy concentrations between the two electrodes causes the migration of oxygen ions though the electrolyte. At the cathode, the electrons released reduce gaseous oxygen to restore the equilibrium vacancy concentration and the cycle repeats. This procedure is illustrated in figure 3.2.

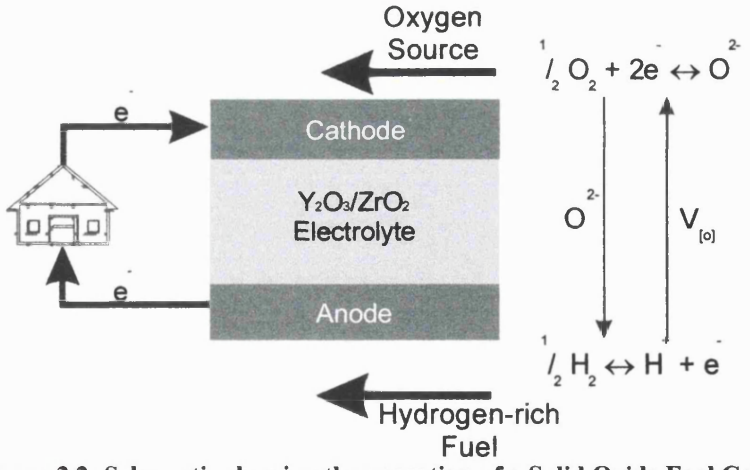

Figure 3.2: Schematic showing the operation of a Solid Oxide Fuel Cell.

For efficient operation the electrolyte material clearly needs a high ionic conductivity and a low electronic conductivity. It must also be stable at the fuel cell operating temperature and be easily fabricated. Yttria-stabilised zirconia has all of these features and is therefore the usual choice of electrolyte.

3.3 Sensors

The Solid Oxide Fuel Cell just described, used an oxygen concentration gradient to drive O^{2-} ions through the zirconia electrolyte and 'complete the circuit' electronically, providing power to an external source and using up fuel at the electrodes themselves. If this process were operated in a slightly different manner (and on a much smaller scale!) we find that it is possible to construct a solid device which can be used to monitor the oxygen concentration in a given source.

If one side of the material is exposed to a standard atmosphere containing 20% oxygen, then oxygen concentration changes on the opposite side of the material would result in charge transfer across the material and an external current which can be monitored and used to control a larger device.

This process is best illustrated by example: the most common oxygen sensor in commercial use lies inside the exhaust stream of an automobile, and is more commonly referred to as the *lambda probe* (the air/fuel ratio is given the symbol 'λ'). In the internal combustion engine, the precise value of λ is of great importance – if it is too high, then the amount of fuel present in the reaction chamber is too great and the engines performance is very low. This situation can be detected by a lambda-probe, since the outlet exhaust fumes would contain a much higher oxygen ratio than normally expected, the sensor can then trigger the fuel injection system to increase the fuel flow rate and restore optimal conditions. Conversely, if λ is too low, the there is not enough oxygen present in the reaction chamber, and the exhaust fumes contain large amounts of uncombusted fuel (therefore decreasing the oxygen content to almost nothing). Under these conditions the engine is wasting fuel and running highly uneconomically, the sensor can respond by altering the fuel inlet to restore the optimal balance.*

* There are however, circumstances which do require such conditions in the engine: at this point the engine power will be a maximum, although uneconomical to maintain, it may be desirable for short periods of time.

3.4 Acid Catalysts

In the last 1970's, Hino *et al.* (36,37) treated the surface of a zirconia sample with sulphuric acid, and created a material known as a 'superacid catalyst'; in this case, the resulting material acted to catalyse the isomerisation of hydrocarbons. More recently, the addition of a wider range of anions, has produced solids having incredible acidic and catalytic properties.

The formation of these acids has massive industrial implications: the isomerisation reactions of many common hydrocarbons involve the use of extremely hazardous materials, including liquid HF, H_2SO_4 and $AlCl_3/BF_3$ (Friedel-Crafts reagents). The use of a solid acid is highly preferable, as storage and handling requirements are much safer, making the entire process much more profitable.

Replacement of the existing catalysts can only be considered when the catalytic activity of the superacid is equal to, or better than, the activity of the (hazardous) catalyst, unless some other overriding concern is considered. Electronic structure calculations on the common surfaces of this material will play an important role in tailoring the specific acid properties of zirconia, and hopefully permit a closer understanding of the source of this acidity.

4 Fluorite

4.1 A Structural Overview of Ceria and Zirconia

It is generally accepted that CeO_2 exists with just a single bulk structure – a cubic phase having the fluorite (CaF_2) structure, illustrated in figure 4.1. The primitive cell for this phase contains two ions: an oxygen ion is located at the point with fractional coordinates [¼,¼,¼], and represented by the yellow spheres in figure 4.1; and secondly a metal ion, represented by the blue spheres, is located at the origin [0,0,0]. The complete lattice is then generated by applying the symmetry operators of space group number 225 (F m 3 m).

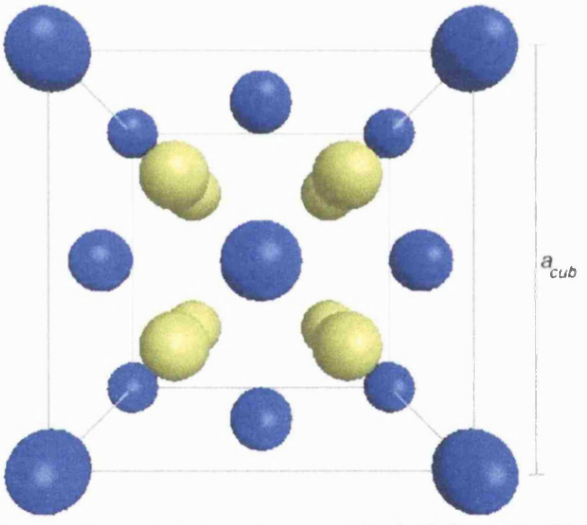

Figure 4.1: The fluorite structure common to both CeO_2 and *c*-ZrO_2 (under the appropriate experimental conditions). Blue ions represent the cations (Ce/Zr); yellow ions represent anions (O).

In such a structure, the anions are coordinated by a tetrahedron of the four closest cations; cations are instead surrounded by a cube of the eight closest anions. We can view this geometry in two different ways, with reference to the cation and anion sublattices, respectively:

(1) a face-centred cubic (fcc) array of metal ions, surrounded by oxygen ions that fill *all* tetrahedral interstices in the structure, or equivalently

(2) a cubic close-packed (ccp) array of oxygen ions, in which the cations occupy *alternate* cubic interstices, so that exactly half are filled.

The experimental cubic lattice parameter of ceria, a_{cub}, as determined from X-Ray Diffraction (XRD) studies is 5.411 Å (38), a highly reproducible figure illustrating the extremely high stability of the material. The corresponding bulk modulus, B_{cub}, of ceria, determined by ultrasonic measurements is 236 GPa (39).

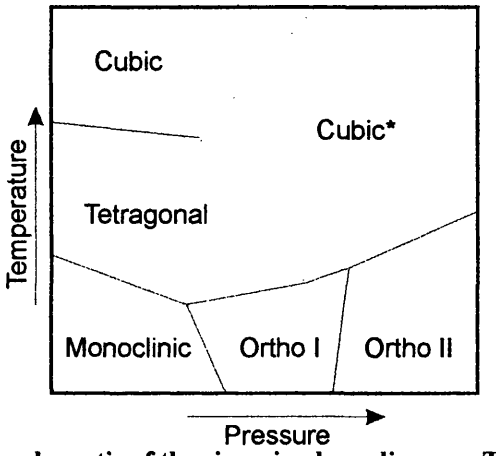

Figure 4.2: A schematic of the zirconia phase diagram. This image is reproduced from that in Ref. (40)

In contrast to ceria, the phase diagram of zirconia (an illustration from Ref. (40) is reproduced in figure 4.2) shows several different structural forms, each of which is stable inside a given temperature and pressure range (41). In this thesis, I am primarily concerned with the use of zirconia in applications operating under atmospheric pressure. For this reason, only the three phases stable under ambient pressure conditions are discussed here.

The high temperature phase, stable for $T > 2600$K, assumes a cubic fluorite structure analogous to that of ceria, which I refer to as c-ZrO_2 in this thesis. In this cubic fluorite-like phase, the experimentally determined lattice parameter lies with the range $a_{cub} = 5.121 - 5.191$Å (38,42), approximately 5% lower than in ceria.

The range of experimental values is caused by the limited stability of this phase; x-ray diffraction (XRD) studies at temperatures as high as 2600K are firstly difficult to perform; secondly, thermal vibration of the ions creates a large broadening of the peaks in the recorded x-ray spectrum, resulting in a great degree of uncertainty in the configuration of the refined structure which makes it extremely difficult to draw any meaningful conclusions from experiment.

To try and circumvent the problems of high-temperature XRD studies, instead, non-stoichiometric zirconia can be examined under less-hostile environments. As mentioned

earlier in this thesis, the cubic phase can be artificially stabilised outside its normal stability field by the addition of large amounts of Y_2O_3, CeO_2 or CaO to the pure phase. Using this method it is possible to stabilise the cubic phase of zirconia down even to room temperature, for further experimental analysis.

In the work by Kandil *et al.* (43), the independent elastic constants of the cubic phase were determined using ultrasonic techniques for a series of zirconia samples (doped with pre-determined levels of yttria), over temperatures ranging from 20°C to 700°C. Kandil used commercially-prepared samples containing 8.1, 11.1, 12.2, 15.5 and 17.9 mol% yttria.* The data was then extrapolated back to predict what the measured elastic properties would have been in an yttria-free sample. This extrapolation technique has been used by several groups attempting to study the properties of pure (and doped) zirconia systems experimentally.

In the following discussion, we should always remember that thermal effects cannot be included into *ab initio* QM calculations at the present time.† All calculations reported in this thesis were performed at the effective temperature of absolute zero. Thermal effects, including lattice expansion and thermal vibrations can all become significant factors, especially when studying systems only stable above temperatures as high as 2600K!

4.2 Previous Studies

There have been numerous interatomic potential based studies performed on ceria and zirconia in recent years (44-48) while the number of *ab initio* quantum mechanical studies is more limited. The reason for this is clear: until recently, calculations of this nature were far too expensive to be cost effective, meaning that substandard basis sets generally had to be used. Because of this, results from interatomic potential (IP) studies were often more reliable and accurate than the *ab initio* studies. A*b initio* calculations

* These concentrations were chosen based on the earlier work by Glushkova *et al.* (82) where they found that a minimum of 8 mol% yttria was needed to stabilise *c*-ZrO_2 at room temperature.

† Without incurring severe cost penalties. As computer power increases, this will no longer be the case.

are usually preferable to IP calculations since they make no assumptions about the nature of the interactions between the ions in the material. As these interactions define the overall chemistry of the material, the detailed analysis permitted by QM studies can be of great importance in better understanding the chemical (catalytic) properties of the material.

The work discussed in this thesis forms the first joint (periodic) Hartree-Fock study of both ceria and zirconia. Although similar work has been performed on either ceria or zirconia independently, such as the papers by Hill and Catlow (49); Stefanovich *et al.* (50), and Orlando *et al.* (51) for example, these studies are not directly comparable to one another in the same way as the calculations reported here.

It is therefore important to reinvestigate these two oxides with a more accurate procedure, and in a consistent manner to enable a direct comparison of the calculated properties of ceria and zirconia. In this section, I shall provide a brief summary of the important conclusions from papers in the literature most relevant to the current study.

4.2.1 Ceria

Few studies have been performed on either the bulk or surface structure of ceria employing a Hartree-Fock approach, and little more with DFT methods. The only HF study of note is that by Hill and Catlow in 1993 (49). Even as recently as eight years ago, it was only possible to perform such calculations using minimal basis sets on the ions. In actual fact, this particular work employed a minimal (STO-3G) basis set on the oxygen ions along with a minimal basis set for a cerium atom; such a combination is "unbalanced". It is our belief that such basis functions would not permit a sufficiently large enough variational freedom of the orbitals on the anions: the only unoccupied orbitals present in this description of ceria are the outermost valence orbitals on the cerium ions, therefore these orbitals must be used to reproduce the chemical properties of the material as a whole.

Hill and Catlow concluded that ceria is a partially covalent insulator, with a cubic lattice parameter of 5.385 Å and a bulk modulus of 357 GPa; the (Mulliken) charge assigned to the cations was +2.35 |e| (and therefore –1.17 |e| to the anions), and the calculated HF band gap reported as 11.25 eV. They quote an experimental value, determined by Wuilloud *et al.* using XPS measurements (52), of between 4-5 eV. More

specifically, the metal *d*-band dispersion was 5.80 eV and that of the oxygen *p*-bands, 8.86 eV.

The literature contains several well developed (and much tested) potential sets which have been used to successfully model the bulk and surface properties of ceria: a comprehensive IP study of all $\{hkl\}$ surfaces in which $h^2 + k^2 + l^2 \leq 20$ was performed by Vyas, *et al.* (46,48) using the two potential sets he derived (and are listed for reference on page 124, in tables 6.1 and 6.2). In this work, Vyas concluded that potential set 1 best described the properties of simple surfaces and of the bulk material – including defect structures and simulated bulk annealing studies; potential set 2 was created to improve upon potential set 1 in studying high index faces where the original potential set failed. Vyas *et al.* used slabs having a (region I) thickness of approximately 25 Å, much larger than is possible in any QM study at present. This potential set was also used more recently by Baudin *et al.* (53), who performed a Molecular Dynamics (MD) simulation of the {011} and {111} surfaces of ceria.

The Vyas study was extended in the course of the current calculations to provide additional data not reported in the literature; chapter 6 details our extended IP study of the {011} and {111} surfaces examined here, while various structural properties of the bulk are reported later in this discussion for reference.

4.2.2 Zirconia

Zirconia currently has many more practical applications than ceria, due in part to its abundance on Earth which makes zirconia the cheaper of the two. This has created a greater driving force towards performing *ab initio* calculations on zirconia-based systems, despite their extreme computational cost.

Orlando *et al.* examined the cubic and tetragonal phases of bulk zirconia, and also the {011} surface. Although *ab initio* results were desirable, the low symmetry of the non-cubic phases and the thickness of the surface slabs studied, meant that lower quality basis functions had to be used. Their basis set was not minimal, however it did make use of a large-core ECP on the Zr ions: a choice which leaves only the outermost four metal ion electrons to be studied explicitly in the calculations. Their choice substantially reduces the cost of the calculations, but may significantly reduce the confidence we can have in the calculated properties of the material.

In the work by Stefanovich, *et al.* (50), both periodic HF and IP calculations were performed on pure and doped zirconia systems; the aim of this work being to analyse the energetics of the phase transitions occurring between the three ambient pressure phases. The periodic HF calculations performed in this paper made use of the same small-core Hay-Wadt pseudopotential used here, with the valence basis functions reported in their earlier paper (54); for cost reasons a Durand-Barthelat pseudopotential (55) was also applied to the oxygen ions.

Their analysis of the non-cubic phases will be studied in greater detail later in this thesis; the study of the cubic phase attributed a (Mulliken) charge of +3.038 |e| to the Zr ions (and therefore –1.519 |e| to the oxygen ions) in a cubic unit cell with a lattice parameter of 5.154 Å.

In the work by Fabris *et al.* (56) an empirical tight-binding (TB) approach was used, the implementation of which is discussed in Reference (56), and the connected work by Finnis *et al.* (57) used a Linear Muffin Tin Orbital scheme (LMTO) to study the properties of the cubic and tetragonal phases of zirconia, and in particular the energetics associated with the phase transformation between the two.

Of the remaining key QM studies on ZrO_2, such as the work by Stapper *et al.* (58) and that by Christensen and Carter (59), the basis functions used are plane-waves; these do not require the laborious and careful optimisation of the atom-centred Gaussian basis sets used in CRYSTAL, however, the non-localised nature of the plane wave basis functions makes it difficult to derive detailed *chemical* interpretations from the results obtained – which were a key requirement of the calculations reported here.

The work by Christensen and Carter used the LDA Hamiltonian with a plane wave cut-off energy of 800 eV, and applied a *k*-point separation of 0.05 $Å^{-1}$; for comparison the CASTEP calculations performed here using ultrasoft pseudopotentials with an energy cut-off of 430 eV, and the same *k*-space grid density.

Interatomic potential calculations on stoichiometric cubic zirconia are few and far between, as the phase has such restricted stability. Instead, many of the IP studies employ potential sets optimised for use in doped systems; several of these sets were tested on the pure phase, but their performance was less than adequate. The best

potential set we have found in the literature to date is that derived by Balducci, *et al.* (44,47,60) shown in table 6.3.

4.3 Basis Set Optimisation

In any computational study there are a series of definable options and tolerances which need to be carefully chosen so that the calculations performed provide an accurate model of the system, without being unnecessarily expensive. Among the most important choices we must define, we have:

1. the Hamiltonian used
2. features of the basis sets
3. limits imposed on the orbital-orbital interactions included
4. the density of the grid which samples reciprocal space

The first and second choices are often due to the QM codes available to perform the calculations, since each will allow a limited choice of Hamiltonians and basis functions. The CRYSTAL program used in this work has the ability to use several different Hamiltonians, many of which were used in the course of this work; however all calculations must make use of atom-centred contractions of Gaussians as the atomic basis functions.

Once the Hamiltonian and basis set are defined, in CRYSTAL calculations, the next most important tolerance is the limit imposed on the number of orbital-orbital interactions which are explicitly examined in the calculations. The 'size' of an orbital overlap is easily visualised by the region indicated in figure 4.3; in the calculation, any overlap which is greater than a given threshold is calculated and used in the evaluation of the internal energy. The calculated overlap between AO's also form the elements of the overlap (S) matrix, in equations (2.21) and (2.22).

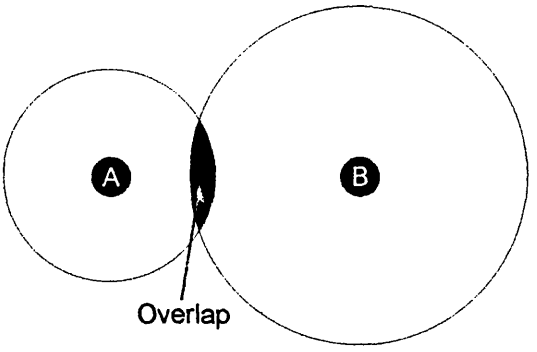

Figure 4.3:The shaded region illustrates the 'orbital overlap' area for orbital A interacting with orbital B.

By decreasing the threshold we include into the calculations longer range interactions. Every overlap included helps to improve the overall accuracy of the calculation, however the CPU and storage requirements of the calculation increase dramatically as the number of included overlaps increase. However, as the value of the overlap decreases, then individual contributions to the total solution become negligible compared to the required accuracy of the calculated properties. In this study, I used the (standard) limits of 6,6,6,6,12 (meaning that integrals between AO's with overlaps lower than 10^{-6} are neglected); for higher tolerance calculations (and our DF calculations) the higher 7,7,7,7,14 limits were used instead.

In addition to the overlap tolerances, the criteria by which we consider the calculations to have converged must also be chosen. There are two alternatives:

1. the calculated internal energy of the system changes less that a specified tolerance ΔE, on subsequent SCF cycles.

2. the eigenvalues of the system change less than a given tolerance ΔC, between consecutive SCF cycles.

The values which we assigned to ΔE and ΔC are listed for reference in table 4.1. The limits for the DFT calculations are generally lower than those using the HF Hamiltonian due to the CRYSTAL implementation of DFT: the use of an auxiliary basis set to sample the calculated density matrix, in fact, may limit the accuracy of the calculation and increase the number of cycles required to achieve the SCF convergence. When the solution in subsequent SCF cycles shows only minor differences (mostly when the SCF

is close to convergence), the numerical noise due to the fitting may significantly affect the results, the calculations are therefore halted at a point when the SCF convergence is close to the numerical noise. This effect is even more important when performing numerical geometry optimisations using CRYSTAL: the use of lower convergence tolerances makes the calculations faster and improves the accuracy in the numerical estimate of the gradient.

Table 4.1: SCF tolerances for both HF and DFT calculations used in this thesis.

Hamiltonian	Quantity	Standard	High Tolerance
HF	ΔE	10^{-6}	10^{-7}
	ΔC	10^{-5}	10^{-6}
DFT	ΔE	10^{-5}	10^{-6}
	ΔC	$10^{-2} - 10^{-3}$	$10^{-3} - 10^{-4}$

The final tolerance parameter that can influence the quality of the calculated results (that I shall examine here), is the reciprocal space shrinking factor, that is the density of the *k*-space sampling grid. As was explained in section 2.5, the Hartree-Fock/Kohn-Sham Hamiltonian matrix for a solid is evaluated at a discrete grid of points spanning the whole of the irreducible Brillouin zone (which represents all of reciprocal space). The eigenstates at points other than those explicitly calculated can be determined by extrapolation from the collection of points available. Clearly, if the number of points in the grid is too small, then the extrapolation of the intermediate values will be highly inaccurate. Conversely, should the grid contain too many points, the time taken to evaluate the solution is too great, and extrapolation can provide an adequate description of the intermediate points much more cost-effectively.

If we wish to draw quantitative and qualitative conclusions from a comparison of the ceria and zirconia calculations, equivalent approximations must be used in both cases (in addition, of course, to the use of identical Hamiltonians, *k*-point sampling densities, and integration tolerances). If a small-core pseudopotential is to be used on cerium, then comparisons must be made to equivalent calculations using a small-core pseudopotential on zirconium. As small-core Hay-Wadt pseudopotentials are available for both Ce and Zr ions, their use here is ideal. Also, both materials make use of the 8-51G oxygen basis set (61) which has been used to model the structural and electronic properties of other metal oxide systems highly successfully (18,19).

4.3.1 Ceria

The fundamental starting point used in the derivation of the cerium basis set is that optimised for an isolated, uncharged, gaseous cerium atom using the Hay and Wadt small-core pseudopotential (62). The use of pseudopotentials in the description of the heavy metal ions is highly desirable to keep the overall cost to a minimum, the applicability of the pseudopotential approximation (and in particular the performance of the Hay and Wadt pseudopotentials) in solid state materials such as ceria and zirconia will be examined later in this discussion. From the isolated Ce atom, we first constructed a basis set to describe an isolated Ce^{4+} ion, as the difference in electronegativity between the metal and the oxygen ions lead us to expect the electronic distribution in the solid to be closer to an ionic model than to neutral atoms: the basis for the isolated gaseous ion is therefore a more accurate starting point to optimise the crystalline basis functions in CeO_2.

The Hay-Wadt pseudopotentials are originally derived for molecular HF calculations, i.e. codes such as Gaussian (30) and GAMESS (63) codes, but can be applied in the same format also for the periodic Hartree-Fock calculations in the CRYSTAL program (9,10). The primary difference in basis set requirements between molecular and crystalline systems is that the former require very diffuse functions to correctly represent the decay of the wavefunction away from the nuclei. In a periodic code, this decay is described by the basis functions associated with the neighbouring ions: inclusion of functions which are too diffuse may cause numerical instabilities when diagonalising the Hamiltonian matrix, with no appreciable increase in the overall accuracy of the calculation, and therefore is best avoided in solid-state calculations.

The second major difference in the basis-set requirements, and possibly the most important in the current discussion, is that the present version of CRYSTAL does not allow *f*-type functions to be included into either the effective core pseudopotential (ECP) or the valence basis functions. Because of this deficiency, we were forced to remove all *f*-functions before the isolated ion basis set can be used within CRYSTAL. As in the isolated ions the *s*, *p*, *d*, and *f*-functions are mutually orthogonal to one another, the optimised *s*, *p*, and *d* functions of the basis set are not affected by the removal of the *f* AO's (i.e. the optimal values for the parameters of the remaining orbitals is left unchanged during this operation).

After removal of the outermost unoccupied diffuse functions, the isolated ionic basis can be inserted into a description of the crystal at the experimentally determined geometry (a_{cub} = 5.411Å (38)) using the standard oxygen 8-51G set derived by Dovesi and Causá (61). A final basis set re-optimisation produced the fully optimised crystalline basis set for the Ce^{4+} ions.

The coefficients and exponents of the Gaussian shells were optimised using the same numerical procedure employed in the geometry optimisations (see section 2.7 for further detail), and were considered to have converged when the energy change on subsequent cycles became smaller than 10^{-7}Ha. After a full optimisation of the cerium basis set, the functions used on the oxygen ions were checked to ensure that they were optimal for use in ceria. The final basis set obtained for crystalline Ce ions is shown for reference in the appendix, in table A2 (on page 159); the oxygen 8-51G basis set is also listed in table A5.

4.3.2 Zirconia

The next stage in the basis set construction is the optimisation of a similar basis for zirconium ions. To ensure a qualitative and quantitative analysis can be performed using the calculated results, it was decided to base the zirconium basis set on the parameters already optimised for the crystalline cerium ions. To do this, the cerium lattice was altered to that of cubic zirconia by switching cerium for zirconium and reducing the lattice parameter, and the Hay and Wadt pseudopotential parameters changed to those reported for zirconium leaving the metal ion valence orbitals unchanged. Due to the degree of uncertainty in the 'true' experimental minimum energy structure, we took the midpoint of the experimental values as a 'best-guess' structure, thus the chosen lattice parameter for the cubic phase was a_{tet} = 5.15Å. The coefficients and exponents of the basis functions were then energy minimised in this structure to create the optimised crystalline Zr basis set, which is reported in table A3 (on page 160). The latter represents a crystalline Zr^{4+} ion, and by construction is qualitatively comparable to the Ce^{4+} basis set employed in ceria. The same oxygen basis set is also used in both oxides.

To verify the accuracy of our solid state calculations on ceria and zirconia, in the following sections we shall compare the calculated bulk properties obtained from the newly derived pseudopotential basis sets to results determined from experiment. In addition, comparisons to the results of similar calculations using optimised all-electron

(AE) basis functions were made. The Zr basis set used to do the latter comparison was kindly obtained from Roberto Dovesi, the Ce AE basis was created from the Zr basis in a similar way to the pseudopotential basis functions just described. The AE basis sets are listed for reference in tables A7 and A8 on page 162.

In addition, the suitability of the Hay-Wadt pseudopotentials employed has also been assessed: we were able to do this for zirconia only, by constructing a basis set of the same quality, but using instead the Stoll-Preuss pseudopotential (64) rather than the Hay-Wadt. This new basis set is given in table A4, on page 160. A corresponding cerium pseudopotential was not available at the time this work was performed, but the study of zirconia-only should be adequate for our needs.

Another interesting feature of the CRYSTAL program, which we have exploited in this work, is the ability to perform *ab initio* calculations using either the Hartree-Fock, or the Kohn-Sham (KS) Hamiltonian, the latter using a wide range of Density Functionals (DFs) in the Local Density Approximation (LDA), Generalized Gradient Approximation (GGA), or hybrid schemes such as B3LYP. A comparison of results on zirconia obtained with all the above Hamiltonians is given in chapter 5.

DFT calculations in CRYSTAL employ a somewhat unorthodox approach compared to the majority of pure DFT codes, since CRYSTAL is originally a HF code. In a DFT calculation the exchange and correlation forces are defined as functionals of the electron density, $E=f(\rho)$. The functional dependence requires us to know the value of the electrostatic density (LDA) and of its first derivatives (GGA) in each point of the primitive unit cell. Since the basis set in CRYSTAL describes the wavefunction and not the electron density, an accurate evaluation of the functionals required in the DFT calculations would be very demanding. To circumvent this problem and analytically represent ρ in the unit cell, a second basis set is defined in the DFT calculations, which we refer to as the "auxiliary basis set". This auxiliary basis set is constructed from a set of atom-centred even-tempered Gaussians, having an angular dependence based on those of the *s*, *p*, *d*, *f*, *g*, etc. solutions obtained for the hydrogen atom. At each SCF cycle, the calculated electron density is expanded onto the auxiliary basis set, and the coefficients of the even-tempered Gaussians are determined from a least squares fit. Calculating the density and the first derivatives needed for the DFT calculations in this

manner is extremely fast and straight-forward, although we must now define a suitable auxiliary basis set for the DFT calculations.

The atom-centred even-tempered auxiliary basis set is specified by giving the orbital type (*s*, *p*, *d*, etc), the number of Gaussians of this type to include in the set, and the smallest and largest exponents to be used. The exponents of the individual Gaussians are chosen to regularly span this range of exponents.

The production of an auxiliary basis set is extremely lengthy, and due to a lack of fine control in the individual Gaussian exponents it can appear to be rather arbitrary at times. It is often recommended (65) that the properties of the even tempered set be chosen so that the individual exponents differ by a factor of three: the properties of Gaussian functions ensure that this will produce maximum coverage with the minimum number of Gaussians, and the following calculations should therefore minimise the cost. The method used to optimise an auxiliary basis set is to manually determine the parameters which provide the lowest least squares fit from the calculated density. We considered satisfactory an error in the fit of 10^{-4}. The auxiliary basis sets optimised for zirconia are listed in table A9; we did not repeat this procedure for ceria.

Table 4.2 lists the calculated cubic lattice parameter and the independent elastic constants calculated for the cubic phase of ceria and zirconia, with experimental values collated from the literature given for comparison. From the experimental figures, we see that ceria and zirconia have remarkably similar elastic properties, although the limitations of ultrasonic techniques and the extrapolation used for zirconia may influence this comparison. It is, however, greatly encouraging to see that the calculated lattice parameters are remarkably close to experiment in both cases.

Table 4.2: A comparison of calculated properties of ceria and zirconia for basis set optimisation at the HF level. All use Hay and Wadt small-core pseudopotential and an oxygen 8-51G basis set. The values of C_{44} in parenthesis refer to fully relaxed values of C_{44}, as detailed later in the text.

	Ceria		Zirconia	
	Calculated	Experiment	Calculated	Experiment
a_{cub} (Å)	5.546	5.411†	5.130	5.121-5.191
C_{11} (GPa)	459	403	617	401
C_{12} (GPa)	102	105	97	163
C_{44} (GPa)	164 (119)	60	166 (128)	55

† See Reference (38)

The equilibrium lattice parameter indicates where the energy surface has a minima, and whether this is located at the appropriate point, but does not contain any further information on the profile of the energy surface around the minimum, and if the latter correctly models the properties of the material obtained from experiment. One simple way to ascertain if this is the case, is to examine the elastic properties and the bulk modulus of the materials: here the minimum energy geometry is deformed slightly by application of an external stress, as detailed in section 2.10. The elastic constant is directly proportional to the second derivative of the energy profile obtained as the magnitude of the applied force is varied. The agreement of the calculated bulk modulus, B, to that determined experimentally gives a clear indication of how well the calculations performed reproduce near-equilibrium conditions. The bulk modulus can be determined by more sophisticated Equations of State (EOS) proposed in the literature (16,31,66-70) or from a linear combination of the independent elastic constants: in cubic systems such as ceria and zirconia, $B_{cub} = (C_{11} + 2C_{12})/2$. In assessing the quality of our calculations, and to compare the results provided by difference computational settings, we shall make use not only of the calculated equilibrium lattice parameter, but also of the elastic constants and bulk modulus so as to obtain a more complete characterisation of the results.

Table 4.3 shows how the minimum (calculated) crystal energy and optimised lattice parameters vary as the number of k-points (shrinking factor) in ceria. From these values, we see that the variation in both the energy minimised lattice parameter and the calculated energy is effectively zero as a function of the k-point grid density: on changing the k-point sampling ratio from 4 to 10, the resulting change in energy is of the order of 10^{-5}Ha, and the change in predicted lattice constant of the order of 10^{-3}Å. A similar picture is obtained for zirconia whereby the minimum energy changes by ~10^{-6}Ha, even smaller than in ceria, and the lattice constant by 10^{-5}Å. We conclude that a shrinking factor of six or eight to be more than adequate in the bulk cubic systems to give converged results. The latter grid spacing corresponds to a sampling of the irreducible Brillouin zone with 29 symmetry unique k-points.

Table 4.3: This table reports the values obtained for the optimised lattice parameter and calculated minimum energy of the cubic phase of ceria and zirconia, for a range of *k*-space shrinking factors.

	Ceria		Zirconia	
shrinking factor	a_{cub} (Å)	E_{min} (Ha)	a_{cub} (Å)	E_{min} (Ha)
4	5.543770	-188.074385	5.130742	-196.160162
6	5.541864	-188.074444	5.130763	-196.160160
8	5.541853	-188.074445	5.130764	-196.160158
10	5.541853	-188.074452	5.130764	-196.160158

In this thesis we have defined the lattice energy of a crystal through equation (4.1), where $E_{crystal}^{calc}$ is the calculated energy (per formula unit) of the energy minimised crystal structure, and E_{atomic}^{calc} is the energy of an isolated atom (summed over all atoms in the formula unit).

$$E_{lattice}^{MO_2} = E_{crystal}^{MO_2} - \left(E_{atomic}^{M} + 2E_{atomic}^{O}\right) \tag{4.1}$$

4.3.3 Ceria Plane-Wave Calculations

The basis sets used in plane wave calculations are very different to the atom-centred Gaussian contractions just examined: instead the electron density is modelled using tens of thousands of periodic functions, spanning the entire unit cell. These individual plane waves are not localised onto any particular ion in the material, and the description of highly localised bonding features requires the combination of a great many plane waves. For this reason, such calculations are often used to model metallic systems in which the electrons in the valence band are not associated with any particular ion.

The core states of an ion form a set of very highly localised energy states – they are centred around its nucleus. To correctly describe core electrons using only plane waves would require a huge number of functions at great computational cost: instead the plane wave basis is augmented using a collection of atom-centred functions to describe the core states with electrons in the inter-ion regions of space described by the plane wave basis. By ensuring that the two types of function remain continuous as we move away from the nucleus the description of the system need not be reduced: usually the primary concern lies with the valence electrons, since these dictate the chemistry of the material.

This approach is similar to the pseudopotential method explained in section 2.3.3: the cost of the calculations is reduced through the use of multiple functional forms to describe the space used in the construction of the Hamiltonian matrix.

The CASTEP calculations performed here made use of an ultrasoft pseudopotential on both the metal and oxygen ions. The electronic configuration of the species present in these calculations were Ce ($5s^2 5p^6 4f^2 6s^2$) and O ($2s^2 2p^4$). The cut-off radius (r_{cut}) used in these calculations was dependent on the l-value of the orbital on the cerium ions: values of 1.60, 1.80 and 2.00 a.u. for the s, p, and f were employed here, on the oxygen ions a cut-off of 1.30 a.u. was used for all functions.

Optimisation of a plane wave basis set is very different to that detailed in the previous section: here we need to determine the minimum number of functions which must be included into the plane wave basis in order to correctly model the system. Often a series of calculations are performed with various plane wave cut-off points: each function has a unique periodicity in a similar way as the Bloch functions constructed in the CRYSTAL calculations.

This periodicity is associated with a given energy: functions with low periodicity represent low energy functions, while a high periodicity is associated with a large energy. By setting an upper limit on the periodicity of the wave, and defining the step in periodicity between adjacent functions, we can construct a set of N distinct plane waves to use as the basis for the following calculations. The higher this energy cut-off point lies, the greater the number of functions which need including into the set – improving the overall accuracy of the calculations but dramatically increasing the cost. To balance the two, a series of calculations are performed on the bulk phase using a range of energy cut-offs, the plot of calculated internal energy against this cut-off energy (an example of which is given in figure 4.4.

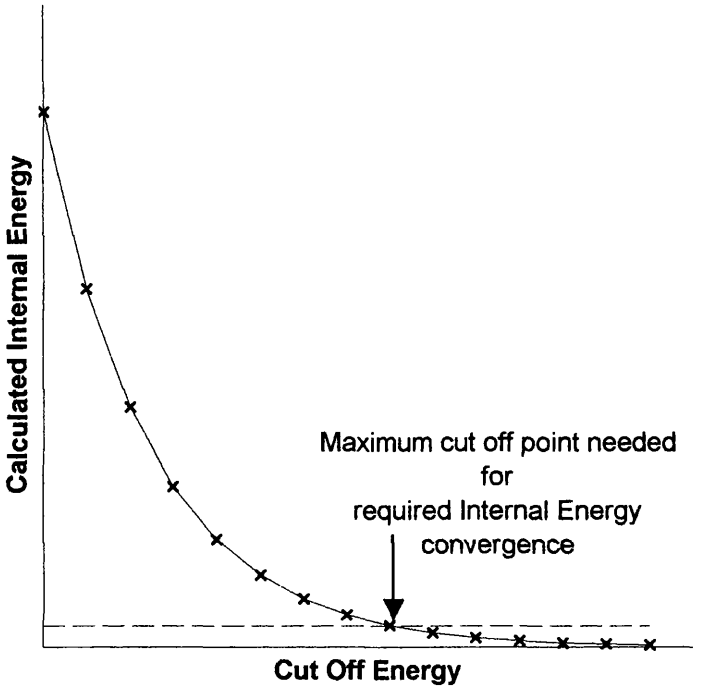

Figure 4.4: Typical internal energy versus plane wave energy cut-off plot. The internal energy is calculated for a series of cut-off energies, and the optimal configuration used in future calculations.

The point at which the calculated internal energy has converged (ensuring the other properties of the system are correctly described) is then used in future calculations as the optimal balance between the number of plane waves which must be included and the accuracy of the calculations. In addition to this, we have also to optimise the density of the grid sampling reciprocal space: periodic DFT calculations are solved in exactly the same way as the periodic HF, with the Kohn-Sham equations being solved at a discrete grid of points spanning the whole of the irreducible Brillouin zone.

Table 4.4: Energy minimised lattice parameter and internal energy calculated for a series of plane-wave cut-off energies.

Plane-wave cut-off energy (eV)	a_{cub} (Å)	E_{min} (eV)
370	5.4560	-7805.9059
400	5.4541	-7805.9523
415	5.4197	-7805.9882
430	5.4195	-7806.0108
445	5.4195	-7806.0443

Table 4.4 reports the energy minimised lattice parameter and calculated internal energy obtained for plane-wave cut-off energies from 370 eV to 445 eV, using a *k*-space sampling grid of 2×2×2 (corresponding to a *k*-point spacing of 0.05 $Å^{-1}$) and a GGA

Hamiltonian. We consider as converged the results obtained with a cut-off energy of 430 eV, and shall employ this value in all future bulk phase DFT calculations on ceria performed with the CASTEP code. We should note also that the energy minimised lattice parameter appears in excellent agreement to the experimental (room temperature) figure of 5.411 Å.

Table 4.5 reports the changes calculated in the equilibrium lattice parameter and internal energy for increasing *k*-space shrinking factors: we see from these results that the current grid of 2×2×2 is already converged in the bulk systems, and there are no benefits to increasing this any further.

Table 4.5: Energy minimised lattice parameter and internal energy calculated for a series of plane-wave cut-off energies..

k-space shrinking factor (*n*×*n*×*n* points)	a_{cub} (Å)	E_{min} (eV)
2	5.4195	-7806.0107612
4	5.4195	-7806.0107618
8	5.4195	-7806.0107676

4.4 Results and Discussion

In order that the predictions and conclusions made by detailed electronic structure calculations on ceria and zirconia can be considered accurate, reproduction of existing experimentally-determined properties is of paramount importance.

4.4.1 Ceria

Starting with bulk ceria, and using the pure Hartree-Fock (HF) Hamiltonian, the calculated energy-minimised cubic lattice parameter (given in table 4.6 for the complete range of available basis functions and Hamiltonians examined in this work) is overestimated by 2.5% compared to experiment (5.411 Å from reference (38)). It is widely accepted that calculations using a pure HF Hamiltonian overestimate equilibrium bond-distances by as much as 5%, due to the internal energy not including electron correlation contributions, a range that our calculated value is well within.

Using the "enhanced" 8-411dG oxygen basis set, constructed from the 8-51G detailed in section 2.3.2, the calculated lattice parameter is reduced to 5.525 Å, demonstrating the small binding effect that the oxygen *d*-functions have on the

structural properties of the stoichiometric bulk material, although this may not apply to surface or non-stoichiometric systems.

Table 4.6: The physical properties calculated for bulk stoichiometric CeO_2 at the HF and HF+C levels with a variety of ion basis sets. Results obtained through interatomic potential calculations are given for comparison, along with experimental data (collated as detailed in the text).

	Basis Set		a_{cub}	C_{11}	C_{12}	C_{44}	B
	Ce	O	(Å)	(GPa)	(GPa)	(GPa)	(GPa)
HF	HW	8-51	5.546	459	102	119	221
		8-411*	5.525	449	79	—	202
	AE	8-51	5.567	613	173	213	320
		8-411*	5.534	575	139	153	285
	Hill and Catlow (49)		5.385	—	—	—	357
HFC	HW	8-51	5.419	503	129	148	254
IP	Potential set 1		5.411	554	125	124	268
	Potential set 2		5.411	573	148	147	289
	Experiment (38,71)		5.411	403	105	60	204
	Experiment (39)		—	—	—	—	236

The two experimental determinations of the bulk modulus are 204 GPa from the elastic constants determined by Nakajima (71), and 236 GPa from Gerward *et al.* (39); the HF estimate of 221GPa, both as linear combinations of the C_{11} and C_{12} values, as well as from fitting the energy versus volume curve, lies within the two experimental measurements. The HF value of the C_{11} and C_{12} elastic constants and also of the bulk modulus, calculated as detailed earlier, agrees quite well to the experimental values these papers report.

Comparing the results of the all-electron and pseudopotential calculations, we notice in table 4.6 that the Hartree-Fock calculations yield a lattice parameter of 5.52-5.54Å when the Hay and Wadt pseudopotential basis set is used, or 5.53-5.57Å using an all-electron basis set. We believe that the small discrepancy of ~0.01 Å between these two values is due to relativistic effects, which are important for heavy atoms such as Ce. While the all-electron calculations do not include relativistic effects either, the derivation of the Hay and Wadt pseudopotential made use of a relativistic Hamiltonian which provides a slightly smaller effective radius for the core states. Comparison of the two values suggest therefore that the pseudopotential basis functions are a good approximation to the all-electron basis set, but also that the pseudopotential basis set optimised in this work provides a good representation of the properties of bulk ceria.

The energy minimised lattice parameter and the symmetry unique elastic constants of bulk ceria have also been calculated with the pseudopotential basis sets complementing the Hartree-Fock results with an *a posteriori* estimate of the correlation energy. This correction is evaluated using the correlation-only Perdew-Wang 91 (often referred to as the Perdew-91 functional) density functional (24) on the HF electron-density. This correlation contribution was not included self-consistently into the calculation of the ground state electronic wavefunction; instead, the energy minimisation of the cubic geometry was performed using the correlation-corrected energy rather than the pure Hartree-Fock energy as before. The *a posteriori* corrected calculations have been labelled as 'HFC' throughout this thesis.

When the estimate of the energy contribution due to electron correlation is included *a posteriori*, the modified energy surface has a minimum much closer to the experimental lattice structure: the calculated lattice parameter is in fact reduced to 5.419 Å. This result would tend to suggest that electron correlation effects are important in CeO_2, although it must be remembered that the Perdew-91 correlation function was not designed to be used in conjunction with the Hartree-Fock exchange.

When comparing calculated and experimental results we should finally take into account that experimental studies are conducted at high temperatures (usually room temperature or above), while the current *ab initio* calculations have been performed at an effective temperature of absolute zero, therefore thermal expansion ought to be taken into consideration.

Table 4.7: Comparison of various equations of state in determining the bulk modulus in CeO_2 at the Hartree-Fock level.

	a_{cub} (Å)	E_{min} (Ha)	B (GPa)
$(C_{11}+2C_{12})/3$	5.546	—	221
Parabola	5.546	-188.07163	218
Murnaghan (69)	5.546	-188.07164	227
2nd order Birch-Murnaghan (66)	5.546	-188.07164	223
3rd order Birch-Murnaghan (66)	5.546	-188.07164	227
3rd order Lagrangian	5.546	-188.07164	227
Davis and Gordon (68)	5.546	-188.07164	227
Bardeen (31)	5.546	-188.07164	227
Slater (16)	5.546	-188.07164	227
Brennan and Stacey (67)	5.546	-188.07164	227
Experiment	5.411 (38)	—	200-240 (39,71)

Often determination of the individual elastic constants for a material is an extremely lengthy computational process: the required deformation can involve rather complex stress tensors and internal relaxations in non-cubic systems in fact. This is a less severe problem in cubic crystals such as ceria, and we have exploited the structural simplicity of the unit cell to evaluate the three symmetry independent elastic constants C_{11}, C_{12} and C_{44}. Moreover, once the internal energy has been calculated as a function of unit cell volume, we can also employ one of the several different equations of state reported in the literature (66,69) for determining the minimum energy lattice parameter (16,31,67,68), and the corresponding bulk modulus, B, for the solid.

Results for ceria are presented in table 4.7. The bulk modulus, B, is directly proportional to the curvature of the energy surface surrounding the minima, with the actual value (and the functional dependence of the energy on the volume V) being defined by the equation of state in use. The general process corresponds to a fit of the parameters of the chosen equation of state to the calculated energy surface: $E=f(V)$. Table 4.7 lists the calculated bulk modulus as determined from a fit to eight different equations of state, as well as to the a simple parabola, and also from a linear combination of the C_{11} and C_{12} elastic constants as explained earlier in section 2.10.

It is clear from this table, that *all* equations of state considered provide the same value for the bulk modulus, minimum energy volume per CeO_2 formula unit (a direct measurement of the internal energy at the minimised cubic lattice parameter), and more importantly that a simple parabolic fit appears already of adequate accuracy in determining the minimum energy lattice parameter and bulk modulus.

Table 4.6 (on page 63) lists the physical properties calculated for bulk CeO_2 at the HF level, while table 4.18 (on page 84) lists the corresponding values calculated for *c*-ZrO_2. The calculated figure for C_{44} is quite considerably larger than experiment in both ceria and zirconia – because a rigid deformation of the unit cell, without allowing the fractional coordinates to relax, does not take into account that the metal-oxygen bond, lying along the <111> crystallographic direction, is able to stretch and deform during the C_{44} relaxation. This relaxation reduces the total energy and thus make the deformation 'easier' and softer than predicted from a strictly rigid model of the C_{44} deformation. To correctly account for this effect, it was necessary to fully relax the metal-oxygen separation for each magnitude of the applied external stress, and

determine the 'true' (i.e. relaxed) value of C_{44} from the curvature of the energy surface formed from these relaxed minimum energies, rather than the unrelaxed energies. Table 4.2 reports both of these figures, with the relaxed values being given in parenthesis.

The relaxation produces a significant reduction in the value of C_{44}, in ceria it is reduced from 164 GPa to 119 GPa (at the Hartree-Fock level), and from 166 GPa to 128 GPa in zirconia; a decrease of over 20%. In both materials the effect has a similar magnitude – hinting to a similar chemical behaviour of the metal-oxygen interaction in both ceria and zirconia in the fluorite structure. The amount of metal-oxygen relaxation was roughly identical in both cases: 0.03Å for an external strain tensor ($\boldsymbol{\varepsilon}$) with individual elements (defined in section 2.10) ranging between $-0.05 \leq \varepsilon_{ij} \leq 0.05$.

Even after this relaxation effect is included into the model, the calculated values of C_{44} are still around twice the experimental value. As we shall see later in the discussion of zirconia, extension of the oxygen basis set to allow for a better description of the oxygen ion polarisability by inclusion of *d*-orbitals further reduces this figure, although it continues to remain significantly larger than the experimental value.

Results of interatomic potential (IP) calculations on ceria are also reported in table 4.6, the agreement of such calculations to the current *ab initio* calculations is, in general, satisfactory for the optimised geometry of this cubic phase. The optimised geometry obtained with IPs reproduces closely the experimental structure, as we would expect since the equilibrium structure was among the experimental observables against which the parameters of the interatomic potential set were originally fitted. However, the agreement between the elastic constants calculated from IP calculations and their experimental and HF values is not as good, for either ceria potential set used, being on average 40% higher (C_{11}). This result implies that the interatomic potential parameters used here overestimate the rigidity of bulk ceria towards external deformation.

The minimal basis set of Hill and Catlow (49) predicted the bulk modulus of CeO_2 to be 357 GPa, in comparison to 221 GPa with the present split-valence quality basis functions. The poor representation of the O^{2-} ions with the minimal basis set clearly shows in the high calculated value of *B*: a minimal basis set does not allow a sufficient relaxation of the electronic distribution on changing the cell volume, thus resulting in a large overestimation of the calculated bulk modulus.

We shall now examine the metal-oxygen bonding properties of bulk ceria. This can be achieved in two ways: firstly by examining the dispersion of energy levels in reciprocal space (the band structure of the solid); and secondly by analysing the calculated electronic distribution.

If a crystal were composed of perfectly non-interacting ions, i.e. each ion has distinct and separate orbitals which do not combine to form molecular (crystalline) orbitals with neighbouring ions, then we would expect to find a set of dispersion-less energy levels in reciprocal space: i.e. if we plot the energy levels along a path in reciprocal space, they would be perfectly flat. In such a case, the material would be 100% ionic.

In practice, however, orbitals on the metal and oxygen ions do interact, and combine into crystalline orbitals. The energy levels change depending on the extent of the metal-oxygen hybridisation; the single atomic orbitals are converted to Bloch functions within CRYSTAL, each Bloch function being modulated by a wave-like coefficient $e^{i\mathbf{k}.\mathbf{r}}$: the extent of the metal-oxygen interaction will, in general, differ at different points of reciprocal space (**k**), giving rise to a dispersion of the energy levels in the band-structure. The deviation from perfectly flat bands allows us to examine the nature (and effectiveness) of the metal–oxygen interactions: as a general rule, the greater the energy dispersion, the more effectively metal and oxygen AOs are mixed in the crystalline wavefunction. In oxides where the metal has a formal electronic configuration of $d^{(0)}$, $f^{(0)}$, as is the case with ceria (and also zirconia), then metal-oxygen interactions are bonding in the valence band (VB), in which the O(2*p*) energy levels are stabilised relative to the perfectly ionic solution, while the conduction band (CB) contains anti-bonding combinations of the M(*d*) and O(2*p*) AOs.

In crystals where the interactions are highly directional, i.e. where the bonding is predominantly covalent, such as diamond, we observe very large deviations from a perfectly flat band as we move across bonding and non-bonding regions of the crystal. In contrast, in a perfectly ionic material there will be much smaller dispersions. We are therefore able to estimate the degree of ionicity in the crystal in a way complementary and independent from standard methods of analysis, such as the population analysis of the electronic density. Both techniques will be applied in this chapter to compare the metal-oxygen chemical bonding in ceria and zirconia.

Before examining the calculated band structures, it is important to mentions that HF calculations will overestimate the band gap compared to experiment; the difference being a factor of two or more in many cases. In our calculations we shall compare the features of the band structure for ceria and zirconia, in which we have used the same Hamiltonian, computational tolerances and oxygen basis set, and where the metal ion basis sets have an equivalent quality, all of which permit a meaningful comparison of the two materials, at least qualitatively.

Figure 4.5 illustrates the HF band structure calculated for ceria at the energy minimised geometry. Alongside the band structures, we also show the Density of States (DOS) calculated for the crystal. This is a plot of the relative number of orbitals in the crystal which have a particular energy: the width of a peak on the DOS plot indicates the extent of the dispersion of a set of energy bands in the same way the dispersion can be seen on the band structure plots. The total DOS includes *all* orbitals present in the system, in addition we are also able to plot the levels due only to a given set of bands in the band structure (for example, only the oxygen *d*-levels), creating a plot known as the Projected DOS (PDOS).

The DOS for ceria is shown in figure 4.6 and includes both the total calculated DOS and the individual projections (labelled as the PDOS plots in figure 4.6) of the total DOS onto the basis functions of the metal and the oxygen ions, as labelled. From the DOS, we clearly see that the levels immediately below the Fermi level (E_f, defined throughout this thesis as the highest occupied energy level) are due to the oxygen orbitals (more specifically, the $2p$ orbitals) and the first set of levels above E_f have important contributions from the metal ions (they are in fact the Ce $5d$ orbitals). This configuration is as we would intuitively expect, in the formation of the crystal from isolated gaseous atoms, electrons are transferred from the metal towards the oxygens: the oxygens therefore acquire a net negative charge, and the metal ions become positively charged.

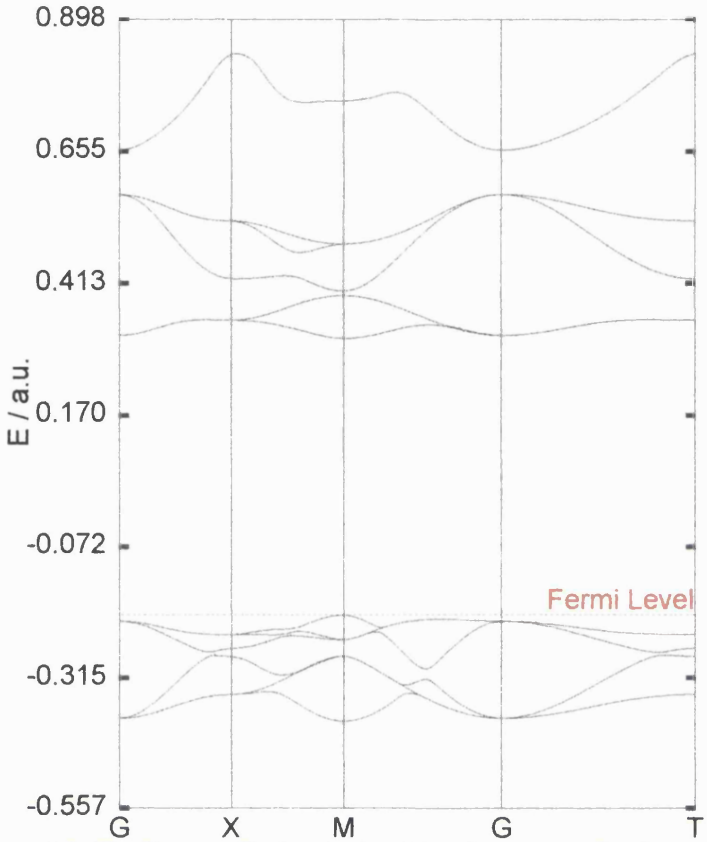

Figure 4.5: The Hartree-Fock calculated band structure for the energy minimised geometry of CeO_2.

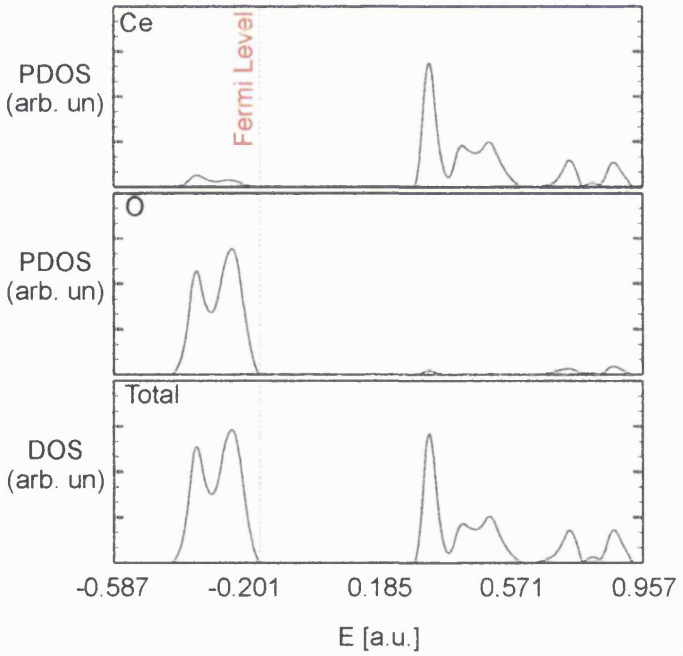

Figure 4.6: The Hartree-Fock calculated total Density of States (DOS) for CeO_2. Atomic projections (PDOS) onto the metal and oxygen ion basis functions are also shown.

The band structure shown in figure 4.5 is plotted for the path (across reciprocal space) illustrated in figure 4.7 – chosen to connect the origin of reciprocal space (G, or

Γ) with the three points (X, M, and T) on the edges of the first Brillouin zone. The labelling of the individual points used in the band structure is summarised in table 4.8, for reference. The minimum energy band gap is a direct transition occurring at the M point of reciprocal space; it corresponds to an energy difference of 14.01 eV between the oxygen 2*p* (located at E_f) and the cerium 5*d* levels. The experimental figure for the band gap is believed to lie in the range of 3-6 eV, a figure quoted by Nörenberg and Briggs (72,73) from an aggregation of the experimental works by Marabelli and Wachter (74), Butorin *et al.* (75), Pfau and Schierbaum (76) and Koelling, *et al.* (77).

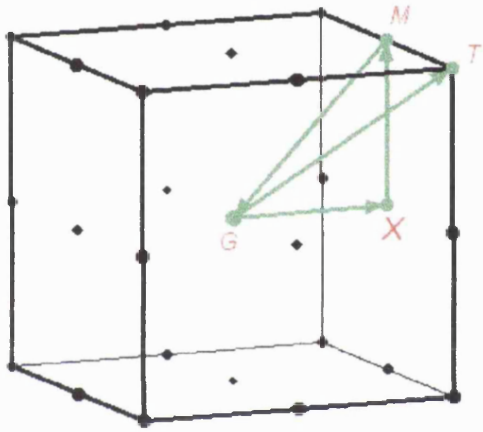

Figure 4.7: This figures illustrates graphically the path across the irreducible Brillouin zone used to plot the band structures shown in figure 4.5.

Table 4.8: Description of the labels used in plotting the cubic band structures.

Coordinates in Brillouin Zone	Label of Point
½[0, 0, 0]	G (the Γ point)
½[0, 0, 1]	X
½[0, 1, 1]	M
½[1, 1, 1]	T

The experimental difficulty in assigning a more precise value to the band gap is due to the presence of dopant ions in the bulk phase – obtaining a highly pure sample of CeO_2 is in fact extremely difficult. Even the smallest quantity of dopant materials may have a significant effect on the energy levels, since dopants and defects are likely to introduce defect levels in the band gap or close to the edges of the valence and conduction bands. It will therefore affect the measured band gap. The same dopants however, do not affect the other observables of bulk CeO_2, such as the lattice parameter: the cubic lattice parameter of ceria remains 5.411 Å even in systems with 20% of the Ce

ions substituted by dopant metals. Even accounting for dopant effects, the calculated figure of 14 eV is more than twice the accepted experimental value, as we expect from the HF calculations. The HF Hamiltonian in fact does not provide an accurate description of unoccupied orbitals, whose energies are much higher than we would normally expect. This phenomenon is a well understood and recognised failing of HF calculations. For comparison, the band gap determined by Hill and Catlow, 11.25 eV, is similar to that calculated here, and also overestimates the experimental value.

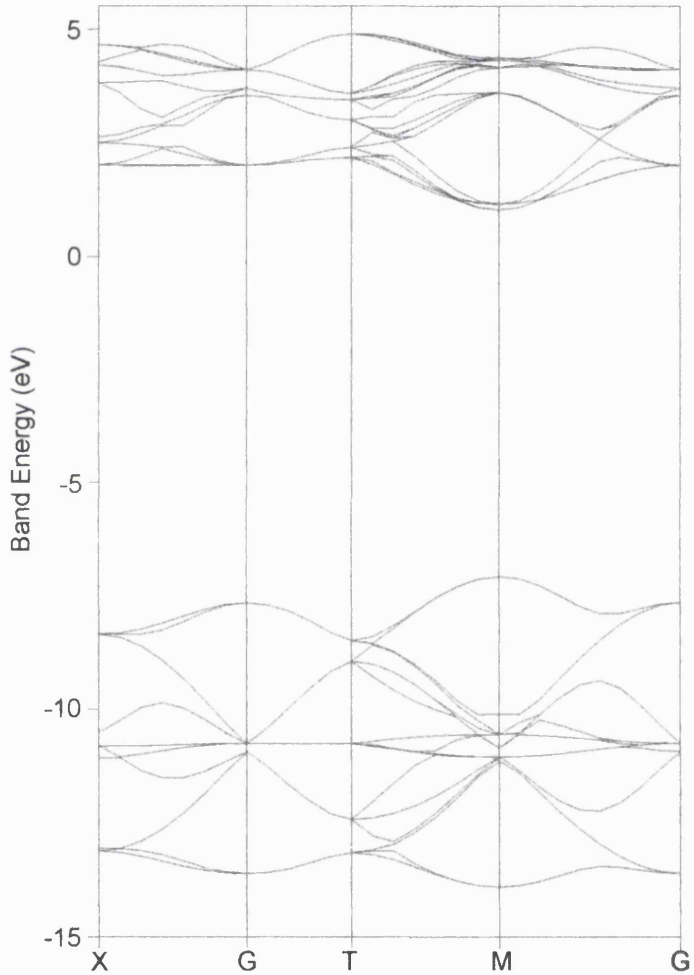

Figure 4.8: CASTEP calculated band structure of ceria (GGA).

DFT calculations, on the other hand predicted a band gap of 8.16 eV (GGA, CASTEP), a figure much closer to experimental observations. The CASTEP calculated GGA band structure and DOS are shown in figures 4.8 and 4.9. From analysis of the DOS, we can assign the levels in the conduction band mainly to the metal ion *d* and *f* functions, the *f* functions being slightly higher in energy than the *d* (and therefore the *d* levels will be occupied before the *f* levels, an important consideration that will be examined further in section 4.4.2). As in the CRYSTAL HF calculations, levels in the

valence band are mainly due to the oxygen 2*p* levels (in the DOS, the energy levels at -28 eV are due primarily to oxygen 2*s* states, which are not included in figure 4.8). It should be noted here that the CASTEP band structure is shown for the conventional unit cell, rather than the primitive unit cell which the CRYSTAL calculations make use of. This is the cause of the additional bands in figure 4.8.

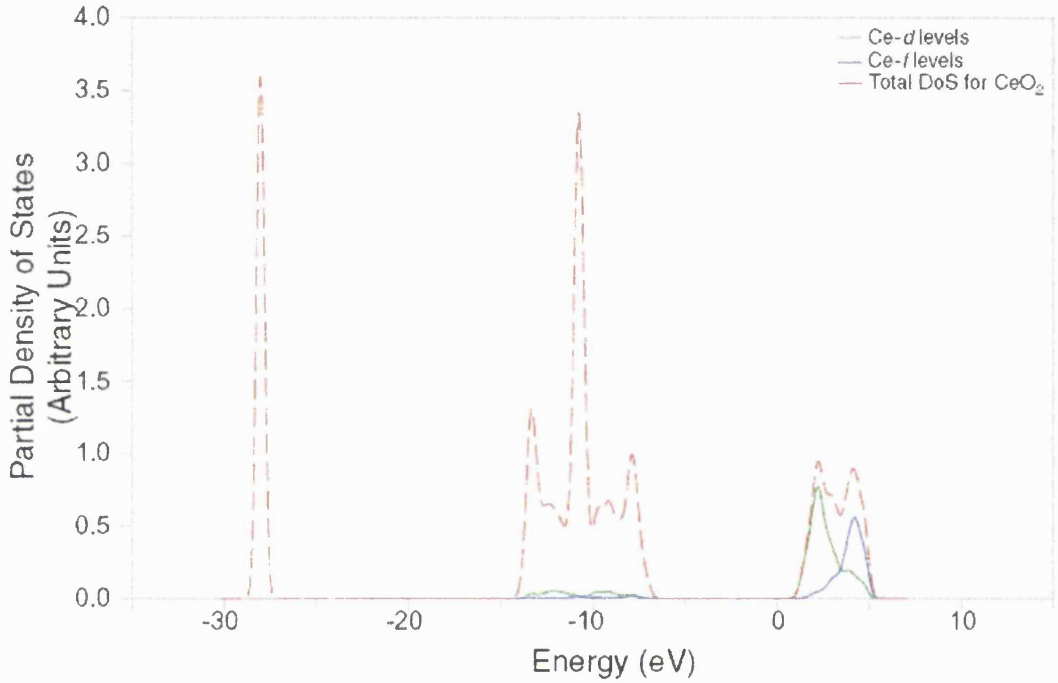

Figure 4.9: The calculated band structure obtained from the plane wave code CASTEP on the optimised structure of bulk CeO_2. The total density of states is indicated by the red dashed line, with the bands due to the metal ion *d* and *f*-levels indicated by the solid green and blue lines respectively. From this figure we can clearly see that the *d* levels are slightly lower in energy than the *f* levels in the stoichiometric oxide. The *f* levels are important for the description of the oxide, but in an ionic material such as the bulk phase they can be safely neglected without severely disrupting the calculated properties of the band structure.

In table 4.9 we have reported the calculated ionic charges for the energy minimised structure, assigned to the ions using a Mulliken scheme (78). In CRYSTAL, the Mulliken charge partitioning scheme simple splits the electrons in a particular crystalline orbital and assigns an amount of charge to every ion depending on the weighted proportion that the atomic orbitals on that ion contribute to the crystalline orbital. For example, if a crystalline orbital were found to be composed of 2×20% oxygen orbitals and 60% cerium orbitals, and contained a total charge of 0.1 electrons, then the Mulliken scheme would assign (0.1×20%) = 0.02 electrons to each oxygen ion, and the remaining 0.06 electrons to the metal ion. By summing over all crystalline

orbitals, we can attribute each and every electron present in the system to a particular ion.

Table 4.9: Mulliken charges, and bond populations calculated for bulk CeO_2, at the HF level.

		CRYSTAL Hay and Wadt/8-51G	CASTEP GGA	Hill and Catlow (49)
Mulliken (|e|)	Q(Ce)	+3.461	+1.410	+2.350
	Q_b(CeO)	-0.043	+0.200	+0.160
	Q(O)	-1.730	-0.705	-1.175
	Q_b(OO)	-0.030	-0.070	—
Band Width (eV)	Ce *d*	7.01	—	8.86
	O *p*	5.35	—	5.80
Band Gap (eV)		14.01	8.16	11.25

The situation is somewhat different in plane-wave codes such as CASTEP: plane waves are delocalised, and cannot be attributed to any particular ion in the material. Instead, the plane waves are projected onto the ions using a localised basis set according to the method proposed by Sanchez-Portal (79), and implemented into CASTEP by Segall *et al.* (80,81). Various atomic properties, such as the Mulliken charge or the local bond populations, can then be calculated using the localised basis rather than the complete set of plane waves. The atomic charges obtained from such an analysis will always be less accurate than those obtained from the CRYSTAL implementation, since the choice of localised basis set projection employed in CASTEP will greatly affect the final charges obtained.

In a perfectly ionic system, the ionic charge would be the formal charges: +4 for Ce, and -2 for O. The current HF calculations instead attribute +3.461 electrons to the metal ions and –1.730 electrons to the oxygens, demonstrating that this phase has a limited degree of covalency, but remains highly ionic in the current study.

In addition, a bond population analysis attributed a slightly negative electron population (-0.043 |e|) to the Ce-O bond in the current HF calculations. The bond population provides information regarding the number of shared electrons between the two ions, and therefore gives an indication as to the extent of covalency present in the material. In the current CRYSTAL HF calculations, both of the important ionic interactions (Ce-O and O-O) in the bulk material were assigned a negative bond population, indicating that the electrons associated with the 'bond' in question belong to

neither of the ions simultaneously – instead they belong to only one of the pair. This finding is interpreted as an ionic interaction, therefore the current HF bond analysis demonstrates the high ionicity of the bulk phase, but at first appears to disagree with the predictions of Hill and Catlow, and also of the current CASTEP calculations.

The CASTEP result can be explained quite simply: the use of non-local plane waves makes determination of localised phenomena such as bond populations rather arbitrary, a comparison to results from an atom-centred basis set will always differ, with the latter often providing the more realistic description of the solid. However, the results of Hill and Catlow are a different matter: the minimal basis set employed in their calculations is unable to provide a sufficient amount of variational freedom in the description of the material. A consequence of this effect, mentioned previously in this discussion, is that is becomes necessary for the unoccupied functions on the cations to be used to describe the valence electrons on the oxygen ions. This effect manifests itself as a spurious Ce-O covalence in the bond population analysis, as the orbitals on the metal ion now seem to contain electrons from the oxygen ions, and therefore have a positive bond population – however this is certainly not the case.

The shortcoming of the basis set of Reference (49) may also help to explain the understated cubic lattice parameter (compared to the experimental value) and also the significantly higher bulk modulus predicted: the spurious metal-oxygen interaction acts to 'bind' the two ions together more tightly than normal, reducing the lattice dimensions and increasing the rigidity of the bulk material.

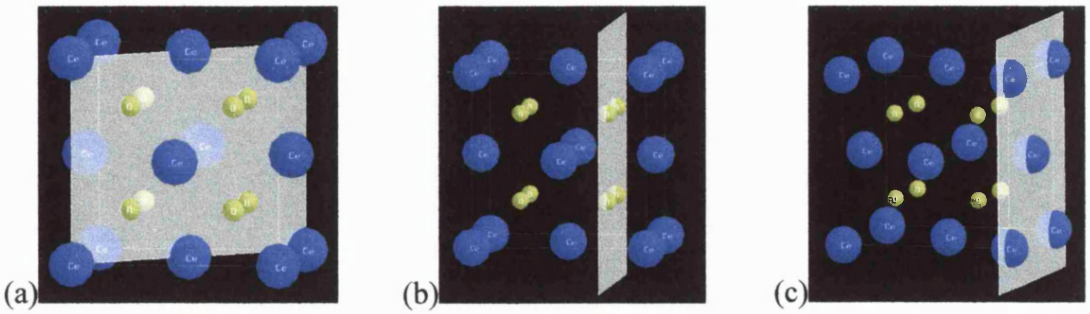

Figure 4.10: Location of electron density cross-sections in the fluorite unit cell. Figure (a) shows the {011} plane; the remaining figures show the two considered positions of the {001} plane, chosen to intersect (b) the oxygen ions; or (c) the metal ions.

In figures 4.11 and 4.12, we report difference electron density plots obtained from the current HF calculations across the {011} and {001} crystallographic planes. These images are produced by subtracting, from the calculated equilibrium electron density of the bulk material, the electron density which would have been obtained if completely non-interacting isolated ions were placed at each of the lattice sites. Such images therefore allow a clear assessment of the effects of covalence, and illustrate graphically any charge transfer which occurs on formation of the crystalline lattice from isolated gaseous ions. There are two distinct positions of interest for the {001} plane, either (a) intersecting the metal ions, or (b) intersecting the oxygen ions – both of which are examined in figure 4.12. For clarity, images illustrating the surfaces along which the electron density cross-sections are plotted are given in figure 4.10, which clearly distinguishes between the alternate choices used for the {001} plane.

Superimposed onto the electron density contour maps are the position of the ions in the material – the standard colours used throughout this thesis of blue cations and yellow anions is repeated here, although only for those ions intersected by the cross-section. The cations coloured in grey, and the anions coloured in green denoted the locations of ions close to the plane, but which do not intersect it.

The contours maps presented in these figures represent the change in electron density which occurs during the SCF part of the calculation, they are generated by taking the electron density created by non-interacting ions located at the appropriate sites in the crystal, and then subtracting this density away from the calculated density of the fully optimised crystal. Contour maps of this type provide a greater insight into the chemical properties of the crystal, and illustrate the electron transfer which must occur on formation of the crystal from the isolated gaseous ions. The individual contours in these images range from –0.05 |e| to +0.05 |e|, with 30 contours used to span the density range. The contours are coloured such that the lower end of the scale (close to –0.05 |e|) are plotted in the 'colder' colours: blue and purple, while contours at the high end of the scale are coloured 'warmer' colours: red and orange. Contours in the middle of the range are coloured from green (slightly negative) to yellow (slightly positive). Note that in an electron difference plot, regions which become electron-rich (negatively charged) during formation of the crystal (in comparison to the isolated atomic electronic structure) are indicated by the positive contours, since these have a higher electron

density. Conversely, regions which become electron-deficient (positively charged) are indicated by the negative contours.

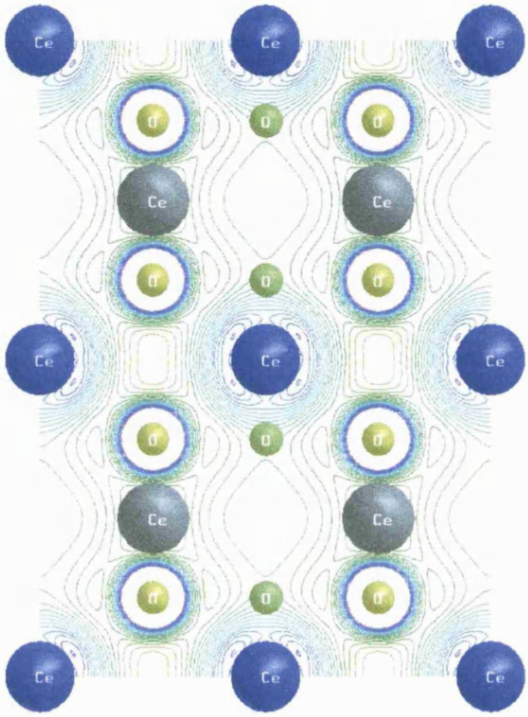

Figure 4.11: Difference HF electron density maps for the {011} plane in bulk ceria. Grey cations, and green anions are out of the plane examined, the blue cations and yellow anions lie in the plane.

We see from figures 4.11 and 4.12 that there is no significant electron transfer apparent in the bulk phase calculated here. Just a small back-donation of electrons from the (formally charged) O^{2-} ions into the *d*-levels of the Ce^{4+} can be seen, in agreement with results from the Mulliken population analysis. There are no significant cation-cation interactions visible, and only a small repulsion of electrons in the regions between neighbouring oxygen ions (see figure 4.11). This is as we would expect for a highly ionic material like ceria: the individual ions act as roughly hard spheres, interacting to a very small extent with the surrounding ions. For this reason, we believe that calculations using the IP Hamiltonian would be capable of providing a reasonably accurate model of this material.

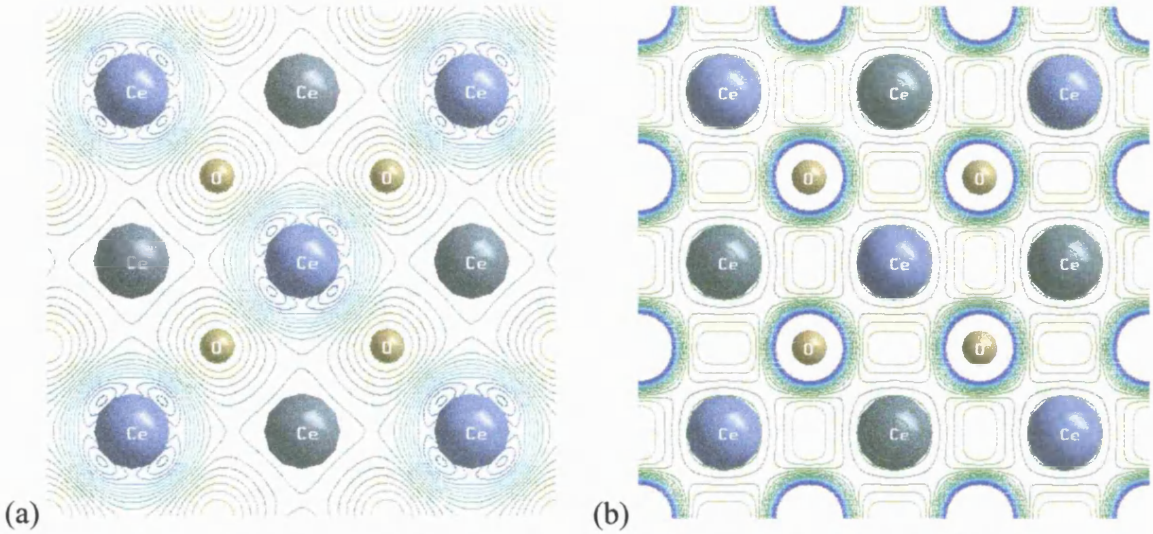

Figure 4.12: Difference HF electron density maps for the {001} plane in bulk CeO_2. Figure (a) intersects the metal ions, while figure (b) intersects the oxygen ions (shown in figure 4.10). Grey cations, and green anions are out of the plane examined, the blue cations and yellow anions lie in the plane.

4.4.2 Importance of the Ce *f*-levels in bulk CeO_2

It was remarked earlier in this thesis that the CRYSTAL program does not currently permit the atomic basis sets to include *f*-type functions in either the valance Gaussian contractions, or the pseudopotentials used on the heavy metal ions. For the purpose of the calculations reported so far, it has been assumed that the *4f* levels present on the Cerium ions are unoccupied in the (highly ionic) bulk phase of CeO_2. The results presented in the previous section appear to suggest that this necessary assumption is valid, although here we aim to quantitatively demonstrate that this is the case.

The precise electronic configuration of Ce(IV) in the solid state has been a pertinent question for quite some time: several experimental studies have attempted to ascertain the 'true' description, and in so doing begin to explain some of the more uncharacteristic properties of CeO_2.

The common viewpoint among many is that proposed by Wuilloud *et al.* (52) in which the *f*-levels are completely unoccupied in the bulk phase. The same situation does not hold for non-stoichiometric samples, since Wuilloud's experiments revealed a series of completely unoccupied *f*-levels within the band gap, while the conduction band demonstrated non-negligible *f*-character. Therefore, in an appropriately doped sample

we would expect back-donation of electrons onto the metal ions, which we would expect to occupy the lowest energy *f*-levels just described.

To further verify Wuilloud's model, we performed additional calculations on the bulk and {011} surface of ceria using the molecular HF code Gaussian94 (30), which allows us to use the same Hay–Wadt pseudopotential and a similar set of valence functions as the CRYSTAL calculations.

In the Gaussian94 calculations, the {011} surface is represented by the Ce_6O_{12} cluster illustrated in figure 4.10, while the bulk phase was modelled by a cluster of 21 ions (12×Ce, 9×O) representing the bulk unit cell as shown in figure 4.1. These ions are then embedded in a grid of point charges, used to represent the Madelung potential of the infinite crystal and its effect on the ions in the cluster.

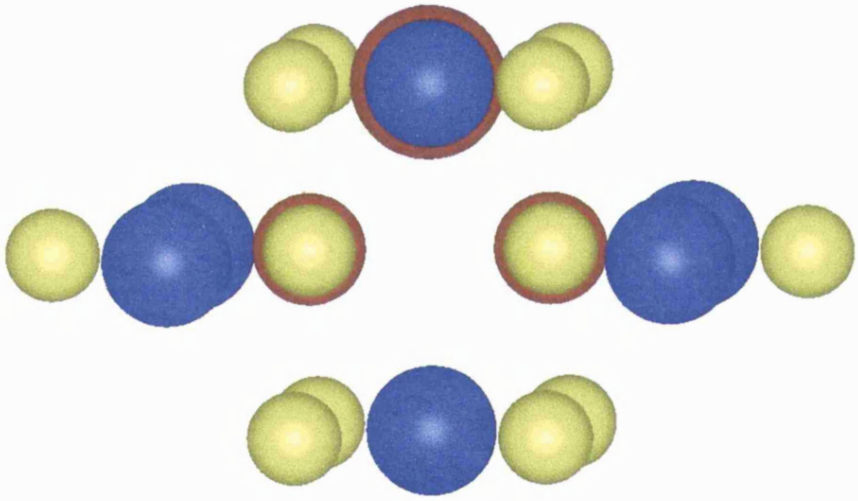

Figure 4.10: The Ce_6O_{12} {011} surface cluster used in the Gaussian[94] cluster calculations. The cluster is surrounded by an array of ~7000 point charges to simulate the infinite crystal, and the central CeO_2 atoms in this cluster (highlighted by the red halo in the figure) were relaxed to a minimum energy configuration.

The optimised geometry of the bulk and surface systems obtained with two different cerium basis sets (one containing *f*-states and a second in which they had been removed) were compared to one another in an attempt to determine the effect that the *f*-levels have on the electronic and structural properties of stoichiometric CeO_2, in both bulk and surface environments. In the surface calculations, the positions of the ions highlighted in red were energy minimised, all remaining ions were kept stationary in their bulk equivalent lattice positions.

Table 4.13: Summary of results from Gaussian and CASTEP bulk ceria calculations compared to CRYSTAL results.

	Gaussian with *f*	Gaussian no *f*	CRYSTAL HF/8-51	CASTEP GGA (PW-91)	Experiment
r_{CeO} (Å)	2.344	2.343	2.401	2.347	2.343
a_{cub} (Å)	5.413	5.411	5.546	5.449	5.411
Q_{Ce} (|e|)	+3.242	+3.390	+3.461	+1.41	
Q_O (|e|)	-1.621	-1.677	-1.730	-0.710	
$Q_b(CeO)$	—	—	-1.730	-0.705	—
$Q_b(OO)$	—	—	-0.030	-0.070	—
$Q_p^{Ce}(f)$ (|e|)	0.06	—	—	0.860	0 (52)

This test with molecular calculations has been extended to the full cluster of figure 4.10, since metal ions lying on a surface are expected to possess a higher electron population than equivalent ions in the bulk due to the lower Madelung field at the surface. Surface ions are therefore more likely to have occupied *f*-levels than the corresponding bulk species, and the test employing the surface cluster is more stringent than the corresponding bulk-like cluster. It is also important for the CRYSTAL surface calculations reported in chapter 6 that the *f*-electron effect be negligible in such simulations, as well as in the bulk phase.

Table 4.14: Summary of results from the Gaussian and CASTEP surface {011} calculations compared to the six layer CRYSTAL calculations. *r(CeO)* refers to the distance from the surface Ce ion to the oxygen in the sub-surface layer (the ions relaxed in the Gaussian calculations).

		Gaussian HF		CRYSTAL
		With F	No F	(HF/8–51)
Surface Layer	Q_{Ce}	+2.16	+2.37	+3.05
	Q_O	-1.32	-1.49	-1.54
	$Q(Ce\text{-}f)$	0.17	—	—
	$r(CeO)$ (Å)	2.228	2.229	2.272
Central Layer	Q_{Ce}	+3.24	+3.39	+3.45
	Q_O	-1.59	-1.68	-1.72
	$Q(Ce\text{-}f)$	0.06	—	—

The surface calculations show the metal ion *f*-levels to contain just 0.17 electrons on the outermost surface ions, falling to 0.06 electrons on metal ions deep in the bulk material. In all cases examined here, the population of the *d*-levels was greater than that of the *f*-levels, suggesting that these are more important than the *f*-levels in the stoichiometric bulk and surfaces examined here. Most importantly, the changes in the

energy minimised configuration of the bulk and surface clusters studied here after inclusion of the Ce *f*-levels was negligible in comparison to the accuracy of the calculations themselves, being well within the background noise expected from a change of basis set: the Ce-O bond in the surface cluster for instance was shortened by less than 0.001 Å when *f*-states were included in the Ce basis set.

These results are in agreement with the conclusions reported by Wuilloud *et al*: in stoichiometric ceria, the *f*-levels remain completely unoccupied. This situation will not hold, however, for non-stoichiometric ceria in which the Ce^{4+} ions are reduced to Ce^{3+}.

4.4.3 Zirconia

In contrast to CeO_2, the experimentally determined properties of *c*-ZrO_2 are less well-defined, due to the experimental difficulties encountered in studying the pure cubic phase – *c*-ZrO_2 is stable only at temperatures above 2600K, as can be seen in the schematic of the phase diagram shown earlier in figure 4.2. For this reason, there is a large uncertainty in the experimental values, even for simple observations like the lattice parameter of the pure cubic phase. Two distinct experimental techniques have been used to attempt to determine the lattice parameter:

1. X-ray diffraction (XRD) studies of pure ZrO_2, performed at extremely high temperatures. The observed lattice parameter is then corrected for thermal expansion to provide a room temperature equivalent. At such high temperatures, thermal motion of the ions produces a significant broadening of the measured spectra, causing great difficulties in accurately refining the geometry.

2. XRD studies are performed on samples of Y_2O_3-stablised *c*-ZrO_2, having varying concentrations of Y_2O_3. Experimental work by Gluskhova *et al.* (82) determined that the cubic phase is stabilised when the dopant concentration is greater than 8 mol%. The lattice parameter of pure ZrO_2 is determined by extrapolating the value obtained for the doped materials to the limit of zero dopant concentration, assumed to represent the undoped ZrO_2 crystal. The elastic constants of cubic zirconia reported in this thesis were obtained with this technique by Kandil, *et al.* (43).

The generally accepted lattice parameter of *c*-ZrO_2, as rationalised in the discussion by Mackrodt and Woodrow (42), lies in the range of values from 5.1–5.2Å;. We commonly take the mid point, 5.15 Å, for convenience in some of the following calculations.

In the following discussion, HW shall refer to calculations performed using the small-core pseudopotential by Hay and Wadt, while SP refer to those using the pseudopotential by Stoll and Preuss; the label 'AE' is used to denote the use of an all-electron basis set. Table 4.17 lists the optimised lattice parameter and bulk modulus of the cubic phase calculated with several Hamiltonians (in the current work) in comparison to several similar *ab initio* calculations (and the IP study by Balducci *et* al.) performed in recent times, and the available experimental data.

It has been mentioned several times in this thesis, that the minimum energy configuration of the material is determined through a parabolic fit on the calculated internal energy surface of the material, using the chosen basis set and Hamiltonian in question. Clearly, if accurate results are to be obtained, the quality of this fitting must be high – and therefore we must be sure that:

(a) a parabolic fit forms a sufficient model of the calculated energy profile, and

(b) the number of points used to sample the energy surface span a sufficiently wide range to be able to reproduce accurately the internal energy profile of the solid.

To assess both of these factors, the fitting is performed using a series of polynomials ranging from a parabola (a polynomial of order two) through to the more complex sixth order function. A collection of eleven data points were chosen, with the central point being the minimum energy configuration; the energy profile for a collection of eleven, nine, seven and five data points are used to calculate the coefficients of the polynomials used here, and the minimum point calculated. In addition, the bulk modulus of the solid – being directly proportional to the rate of curvature of the energy surface at the minima, can be reported for the same set of data points. In tables 4.15 and 4.16 we report the calculated minimum energy lattice parameter and the corresponding bulk modulus for each of these cases (using a strain tensor with components δ=-0.05...0.05).

Table 4.15: Determination of a_{cub} in zirconia (HayWadt/8-51G) by a fit to various polynomials

Order of Polynomial	Number of Data Points			
	11	9	7	5
2	5.149	5.150	5.150	5.152
3	5.147	5.147	5.147	5.147
4	5.147	5.147	5.147	5.147
5	5.147	5.147	5.147	—
6	5.147	5.147	5.147	—

Table 4.16: Determination of B_{cub} in zirconia (HayWadt/8-51G) by a fit to various polynomials

Order of Polynomial	Number of Data Points			
	11	9	7	5
2	269	262	257	253
3	274	274	274	273
4	273	273	273	274
5	272	272	271	—
6	274	274	274	—

There is a clear 'central' region in these tables, where the calculated minimum energy lattice parameter and the predicted bulk modulus of the material are invariant of both the number of data points used in the fit and the order of the function used in the fitting, being 5.15 Å and 270 GPa. We can conclude from this that a parabolic fit to the calculated energies is a close enough representation to the lattice parameter and the predicted bulk modulus for our requirements, compared to the experimental values, provided (or course) that enough points are included in the fitting.

Use of a higher order polynomial in the fitting provides a smaller lattice parameter (and therefore a larger bulk modulus) than the simple parabola, although all remain well within the experimental range of values and there appears little to be gained from use of a higher order polynomial.

Table 4.17: Geometric data obtained from a geometry optimisation of the cubic phase of ZrO_2. Results from the GW approach (Králik, *et al*) (83), experiment and the large-core pseudopotential used by Orlando *et al* (51) are given for comparison.

		a (Å)	V/atom	B (GPa)
Current Work	HF HW	5.125	11.22	273
	HF AE	5.130	11.25	285
	HFC HW	5.010	10.48	325
	LDA HW	5.067	10.84	273
	GGA HW	5.150	11.38	241
	B3LYP HW	5.145	11.34	244
	Orlando (51)	5.035	10.64	222
	Stapper (58)	5.078	10.91	268
	Fabris TB (56)	5.020	10.54	310
	Finnis LMTO (57)	4.996	10.39	—
	Králik (83)	5.035	10.64	—
	Balducci (44)	5.050	10.73	285
	Experiment (42,84)	5.121 - 5.191	11.19 - 11.66	194 - 254

The study by Králik *et al.* makes use of a GW extension to traditional DFT calculations: the DFT calculated band structure is modified through use of a quasiparticle approximation to the electron. Such a technique is rather new and extremely difficult to apply, although it is believed to replicate the salient features of the band structure more accurately then either HF or DFT currently can.

We see from this table that all of the current calculations, either HF or DFT provide remarkably similar values for the optimal geometry of this material, more importantly which are also in good agreement to the other quoted results. A more comprehensive listing of the individual elastic constants determined in several of these studies are given in table 4.18, in which one of the most important results to note is the good correspondence of the all-electron calculations to those using the two pseudopotentials studied here. All calculations using the standard 8-51G oxygen basis set are in good agreement when we examine the optimised geometry of the cubic phase, as are those performed using the enhanced 8-411dG set. In addition, the predicted energy minimised lattice parameter is within the range of data observed experimentally.

Table 4.18: The physical properties calculated for bulk stoichiometric *c*-ZrO_2 at the HF and HFC levels, with a variety of ion basis sets.

	Basis Set		a_{cub}	C_{11}	C_{12}	C_{44}	B
	Zr	O	(Å)	(GPa)	(GPa)	(GPa)	(GPa)
HF	HW	8-51	5.130	617	97	128	270
		8-411*	5.125	617	84	91	262
	SP	8-51	5.136	611	88	124	263
		8-411*	5.136	617	80	84	259
	AE	8-51	5.152	645	110	143	290
		8-411*	5.131	660	107	98	286
	Orlando *et al.* (51)		5.035	628	19	82	222
HFC	HW	8-51	5.030	666	119	202	301
		8-411*	5.015	—	—	—	325
IP	Balducci *et al.* (44)		5.035	616	120	101	285
	Mackrodt and Woodrow (42)		5.121	841	162	75	388
Experiment (42)			5.191	401	163	55	242
Experiment (43)			—	417	82	47	194

The figures for the currently calculated bulk moduli reported in tables 4.17 and 4.18 were determined in the same manner as previously used in ceria: the calculated internal energy was determined as a function of cell volume and then fitted to a collection of equations of state in the literature, a sample of which (for the HW/8-51G calculations) is listed in table 4.19. We see here that all equations of state provide a similar value both the lattice parameter and the bulk modulus, thus reinforcing our confidence in values reported here.

Table 4.19: Comparison of various equations of state in determining the bulk modulus in ZrO_2 at the Hartree-Fock level.

	a_{cub} (Å)	E_{min} (Ha)	B (GPa)
$(C_{11}+2C_{12})/3$	5.130	—	270
Polynomial (see tables 4.15 and 4.16)	5.147	-196.12782	273
Murnaghan (69)	5.147	-196.12776	272
2nd order Birch- Murnaghan (66)	5.147	-196.12777	274
3rd order Birch- Murnaghan (66)	5.147	-196.12776	273
3rd order Lagrangian	5.147	-196.12778	275
Davis and Gordon (68)	5.147	-196.12776	273
Bardeen (31)	5.147	-196.12776	273
Slater (16)	5.147	-196.12776	273
Brennan and Stacey (67)	5.147	-196.12776	273
Experiment (42,43)	5.121-5.191	—	220-245

The reported experimental elastic constants determined by Kandil *et al.* (43) are also replicated with reasonable accuracy in table 4.18: the calculated value of C_{11}

(>600 GPa) is, however, significantly higher than the observed 417 GPa although we must remember that the experimental data refers to an extrapolation of doped systems to the limit of the pure sample – addition of yttria increases the equilibrium oxygen vacancy concentration of the bulk phase, which is likely to alter the elastic response of the material under tensile strain quite substantially and in a non-linear manner. The work of Kandil used zirconia samples having yttria concentrations between 8 mol% up to almost 18 mol%, with the cubic-phase stabilisation effect noticeable only above 8 mol%. The trend in measured elastic properties across the 8 mol% barrier is unlikely to be linear, and the extent of the extrapolation is extremely large given the span of the experimental observations.

The values of C_{12} and C_{44} however are much closer to those determined such a technique: a response which may arise as the C_{12} and C_{44} deformations require application of shear strains, and are therefore more dependent upon the torsional properties of the metal-oxygen (and oxygen-oxygen) interactions, rather than the compressibility of the material.

We obtained several different sets of interatomic potential parameters from the literature (44,48) which are listed in tables 6.1-6.3. Although we are able to compare the predicted elastic properties obtained from IP calculations, we must always remember that such parameters are often used in the initial derivation of the potential parameters, in particular the bulk modulus. We therefore expect our IP calculations to accurately reproduce the experimental bulk modulus. The agreement of the individual elastic constants may not be as good, unless such parameters were also used in the fitting. In the zirconia IP calculations (reported in table 4.18), this does appear to be the case; the calculated elastic properties from the two ceria potential sets are much better, suggesting that these constants were used to derive the potential sets. We believe that the discrepancy between the IP and experimental elastic constants is caused by the IP Hamiltonian being unable to provide an inadequate representation of the oxygen polarisability in the calculations, which then overestimates the rigidity of the material under external stresses. The predicted elastic constants are therefore much larger than experiment, as observed.

For this effect to be the case, we would expect that in the current *ab initio* HF calculations, the calculated value of the elastic constants would decrease as the

description of the oxygen ion basis is improved to include polarisation functions. In table 4.18 this is the observed result. On changing the oxygen basis from the standard 8-51G to the extended 8-411dG set, the calculated value of C_{12} and C_{44} decreases quite significantly, thus confirming our conclusions regarding the IP calculations.

The previous work by Orlando *et al.* (51), was also performed at the HF level and using the CRYSTAL code, but the authors employed a large-core pseudopotential on the metal ions, leaving two *sp* shells and two sets of *d* functions; the oxygen basis used here was the same 8-51G set used in the current calculations.. On closer examination of their results, it was noted that they obtained the unusually small value for C_{12} of 19 GPa, much lower than the experimental value of 83 GPa (or 163 GPa in the Mackrodt and Woodrow paper (42)). To attempt to understand why they obtained a value so small, we performed a Mulliken population analysis using the basis functions and optimised geometry which they had obtained, reported in table 4.20.

Table 4.20: Mulliken orbital populations of the Orlando *et al.* study of bulk *c*-ZrO_2.

	s (|e|)	*sp* (|e|)	*d* (|e|)	Total Ion Population (|e|)
Zr	—	-0.006, -0.754	0.354, 0.747	0.342
O	2.006	4.668	3.156	9.829

The results of this Mulliken analysis attribute an appreciably negative electron population of –0.760 electrons to the inner two zirconium *sp* contractions: which tends to suggest that these functions overlap appreciably with the region of space described by the large-core ECP, which is likely to create nodal planes in the calculated wavefunction. We believe that the appearance of such a small value of C_{12} is caused by this spurious description of the metal-oxygen interaction. The current high quality QM studies provide a figure for C_{12} in excellent agreement to the figure quoted by Kandil.

The polarisation of the oxygen ions is believed to be an important factor in correctly modelling the non-cubic phases of zirconia, and in particular the energetics of the cubic to tetragonal phase transition – the problem studied by Orlando in reference (51), and the application of basis functions providing a description of the metal-oxygen interaction as observed above could only provide misleading results.

All theoretical studies performed on both ceria and zirconia so far have overestimated the value of C_{44} quite considerably compared to the experimental values. Inclusion of polarisation functions on the oxygen ions in the current study reduced the calculated value of C_{44} substantially. Results using the large core ECP (Orlando *et al.*) gave an even smaller value for C_{44}, indicating that their chosen basis set, and in particular the large-core ECP underestimate the short-range repulsion with the Zr outer core electrons compared to the small-core ECP and all-electron basis sets employed in the current study. Due to this, we believe that the calculations of Orlando *et al.* in. reference (51) overestimated the polarisability of the oxygen ions through use of the metal ion basis functions as extensions to the anion basis.

As noted with the IP calculations earlier in this section, a correct description of the oxygen polarisability is of great importance in correctly describing the elastic properties of the bulk material. The anomalous description of the oxygen polarisation functions in the work by Orlando greatly reduces the calculated elastic properties, as was observed here on changing the oxygen basis set from the 8-51G to the 8-411dG set, however it is not a true property of the material – rather an inadequacy in the basis functions provided.

Table 4.21 lists the ground state atomic energies calculated for Zr and oxygen with a variety of Hamiltonians – these figures are used in the determination of the enthalpy of formation of the crystal – $\Delta E_{lattice}$, also known as the lattice energy of the solid, using equation (4.1). Figures for the calculations including the *a posteriori* correlation energy are not included here, since the correlation correction is not included self-consistently into the calculated wavefunction, so the atomic energies reported would not be appropriate for a correlation corrected Hamiltonian.

Table 4.21: These are the calculated atomic energies for each of the Zr basis sets employed, and each of the Hamiltonians studied here (all calculations use an 8-411G* oxygen basis set).

		Atomic Energy (Ha)			
Hamiltonian	Zr Basis Set	Zr	O	E_{calc} (Ha)	ΔE (Ha)
HF	AE	-3538.946464	-74.801129	-3689.113020	-0.5643
HF	HW	-45.978518	-74.801129	-196.160129	-0.5794
LDA	HW	-46.276408	-74.511115	-196.270884	-0.9722
GGA	HW	-46.443886	-75.075623	-197.403341	-0.8082
B3LYP	HW	-46.383686	-75.059191	-197.280801	-0.7787
Králik (GW) (83)		—	—	—	-0.7665

We shall now examine the electronic structure properties calculated for the bulk phase. A Mulliken population analysis, given in table 4.22 shows that the charge on the metal ions is predicted to range from ~+2.2 |e| in the current DFT calculations to around +2.8 |e| in the HF calculations, a trend commonly observed between the different Hamiltonian schemes. We expect little difference between the traditional HF calculations and those including an *a posteriori* correlation correction, as the correlation correction is not included self-consistently into the wavefunction explicitly, its only influence being due to the contraction of the lattice parameter from the pure HF calculations (from 5.125 Å to 5.010 Å) which will produce a small change in the effectiveness of the metal-oxygen hybridisation: the shorted ionic separation will allow a more effective mixing of the two orbitals, producing a negligibly higher electron transfer of around 0.04 |e| per cation.

Table 4.22: Electronic structure data obtained from a geometry optimisation of the cubic phase of ZrO_2.

					Band Width (eV)		
	Q(Zr)	Q(O)	Q_b(ZrO)	Q_b(OO)	Zr	O	Band Gap (eV)
HF AE	+3.331	-1.666	-0.017	-0.101	—	—	—
HF HW	+2.788	-1.394	0.038	-0.054	7.05	7.54	13.36
HFC HW	+2.751	-1.375	0.031	-0.073	7.23	7.61	13.62
LDA HW	+2.127	-1.063	0.063	-0.050	6.35	6.16	3.18
GGA HW	+2.205	-1.102	0.066	-0.034	5.63	5.76	3.15
B3LYP HW	+2.330	-1.165	0.061	-0.041	6.01	6.16	4.92
Králik GW (83)	—	—	—	—	—	6.50	5.55
Orlando (51)	+3.658	-1.829	-0.049	-0.063	—	7.97	12.30
Stapper (58)	—	—	—	—	—	—	—
Experiment (42)	—	—	—	—	—	—	4-6

We note here that in zirconia, the bond population for the shortest metal-oxygen interaction is approximately 0.04 |e| in the HF calculations, and 0.06-0.07 |e| in the DFT calculations. This positive bond population reinforces our belief that this material has a limited degree of covalency, while still remaining largely ionic. Again, the inadequate basis set employed in the study by Orlando leads to a misleading Mulliken population analysis of the bulk phase: here the material is predicted to be almost perfectly ionic, possessing both a substantially negative Zr-O bond population but also extremely high ionic charges, which are very close to the formal +IV and –II charges. As with the Hill

and Catlow study detailed in section 4.4.1, this effect is *not* a property of the material, but rather a limitation of the basis sets.

A sample band structure, and corresponding density of states is illustrated in figure 4.11, calculated here with the HW/8-51G basis sets – the path used is the same as in ceria, illustrated in figure 4.7 and with the point labels as listed in table 4.8. The band gap is again a direct transition occurring at the M point, with the corresponding band gap energy this time being calculated as 13.36 eV.

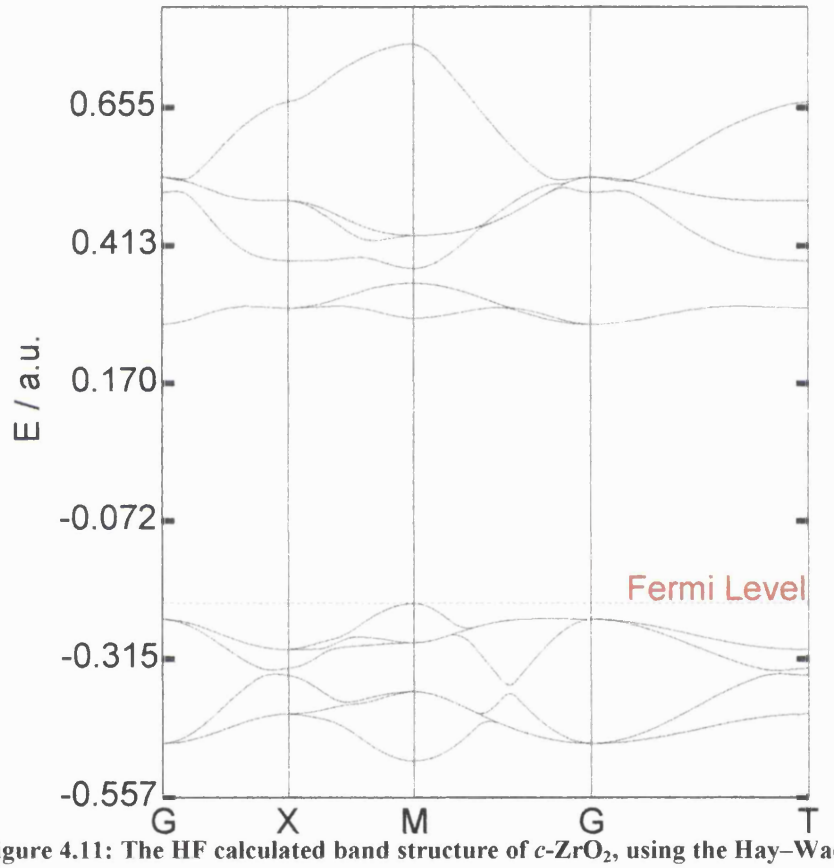

Figure 4.11: The HF calculated band structure of *c*-ZrO_2, using the Hay–Wadt pseudopotential and the oxygen 8-51G basis set.

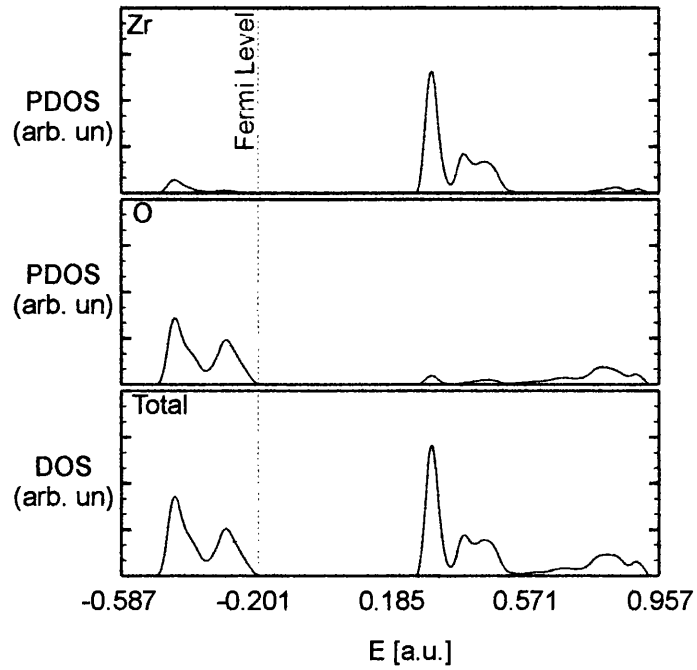

Figure 4.12: The HF calculated density of states of *c*-ZrO_2, using the Hay–Wadt pseudopotential and the oxygen 8-51G basis set. Projections onto the metal and oxygen ion basis functions are also reported, as labelled in this figure.

The calculated DOS shown here demonstrates that levels immediately below the Fermi level are almost entirely due to states on the oxygen ions (the 2*p* orbitals), while the first set of empty levels above the Fermi level are due primarily to levels on the metal ions (the 4*d* orbitals in this case). These same features were also observed in the band structure calculated for ceria, in which we also note that the topology of the energy levels is identical in both cases.

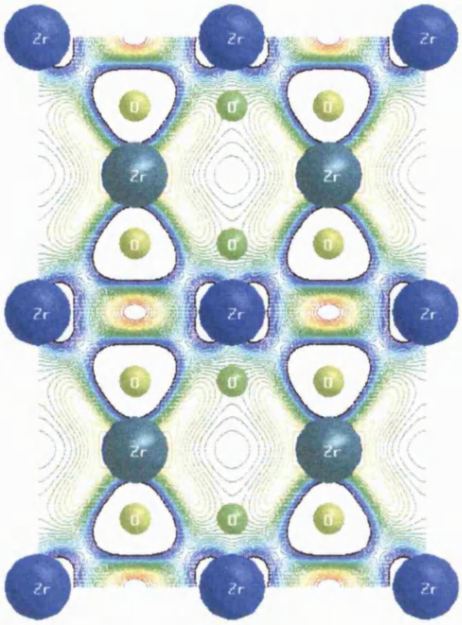

Figure 4.23: Difference HF electron density maps for the {011} plane in bulk cubic-zirconia. Grey cations, and green anions are out of the plane examined, the blue cations and yellow anions lie in the plane.

In figure 4.23, we report the contour maps illustrating the equilibrium electron density for the bulk phases along the {011} crystallographic plane, which cuts the cubic interstice occupied by the metal ions along the diagonal. This images represents the difference obtained when the electron density due to isolated M^{4+} and O^{2-} ions is subtracted from the total density, and therefore represents the backdonation of electrons from the filled O(2*p*) to the empty M(*d*) AOs caused by covalence effects. The contours in this image range from -0.005 |e| to +0.005 |e|, with the thirty contours shown spaced linearly across this whole range. The contours are again coloured such that the 'cooler' colours (blue and purple) represent the highly negative end of the difference density range, while the 'warmer' colours (red and yellow) represent the highly positive end of the range. Note that since these images are *difference* density plots, areas indicated as positive represent regions which become more positive on formation of the crystal lattice, i.e. electrons are moved away from the regions with red/orange contours, while the blue/purple areas indicate regions which receive electrons.

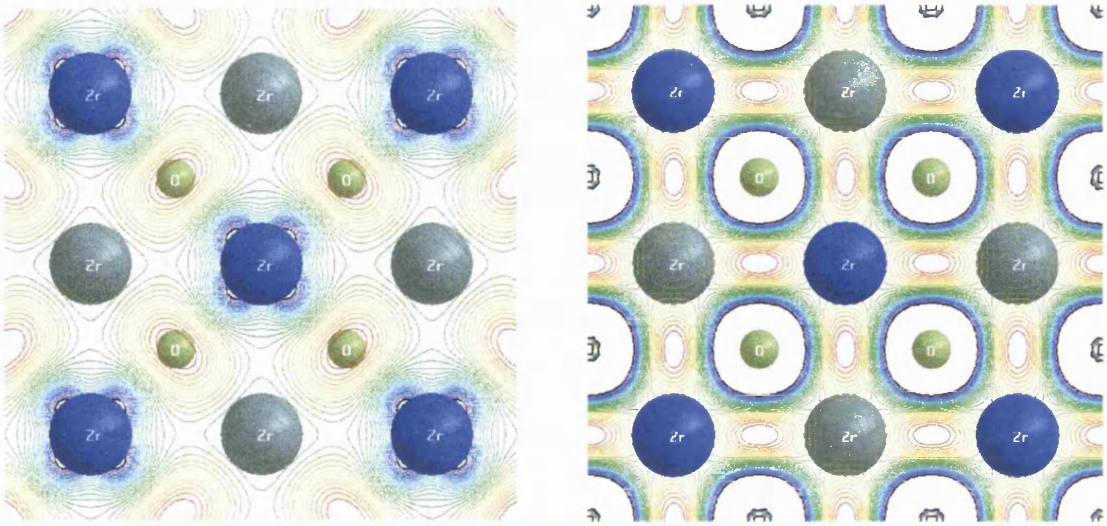

Figure 4.24: Difference HF electron density maps for the {001} plane in bulk *c*-ZrO_2. Figure (a) intersects the metal ions, while figure (b) intersects the oxygen ions (shown in figure 4.10). Grey cations, and green anions are out of the plane examined, the blue cations and yellow anions lie in the plane.

These density maps confirm that zirconia is significantly more covalent than ceria: the electronic density on the metal ions is in fact higher in zirconia than in ceria; furthermore the difference electron density has a region of negative values between nearest neighbour Ce and O ions in CeO_2, excluding appreciable sharing of electrons in the internuclear (bond) region, whereas in the difference electron density plot of zirconia there is a positive electron difference between metal and oxygen nuclei, indicative of a more effective sharing of electrons in the Zr-O bonds compared to the Ce-O bonds.

In figure 4.24 it is important to note the depletion of electron density (represented by the red contours, since such regions will be positively charged in comparison to the atomic density) in the regions between neighbouring oxygen ions, especially between the oxygens around a common metal ion. This effect is much larger in zirconia than previously observed in ceria, as was suggested earlier during the analysis of the band structures; we attribute this to the smaller lattice parameter of zirconia resulting in the neighbouring oxygen ions being closer to one another, and therefore interacting to a greater extent. The above interactions, both metal-oxygen covalence and the oxygen-oxygen repulsion was also quantified by the results of the Mulliken population analysis on the bulk electronic distribution, discussed earlier in this chapter. We note, in particular, the highly ionic nature of both materials studied, which is even greater in

ceria than in zirconia. The net charge attributed to the cerium ions is +3.46 |e|, very close to the formal charge of +4 |e|, while the zirconium net charge is +2.99 |e|. Furthermore, the population of the metal-oxygen bonds in ceria is negative, confirming the highly ionic nature of the cerium-oxygen interaction, while in zirconia it assumes a positive value, due to the more effective covalent hybridisation of the frontier atomic orbitals on the zirconium and oxygen ions. The inter-oxygen repulsion manifests itself in the highly negative population of the oxygen-oxygen bond, calculated as -0.068 |e| in zirconia and in ceria as -0.030 |e|.

4.5 A Comparison of the Two Materials

ZrO_2 has a considerably smaller lattice parameter than CeO_2, 5.14Å compared to 5.55Å at the HF level, and in good agreement with experiment. The difference is obviously caused by the larger ionic dimension of the Ce^{4+} ions (r_{ionic} = 101pm (85)) when compared to the Zr^{4+} ions (r_{ionic} = 86pm (85)); ceria therefore requires larger interstices in the oxygen sublattice, and an increase in the oxygen-oxygen spacing in the crystal in order for the larger cerium ions to be accommodated. Given the shorter metal-oxygen, the calculated bulk modulus of ZrO_2 is larger than that of CeO_2: deformation of the crystal is more difficult as the interaction itself is more effective, thus strengthening the bond.

This finding is confirmed by experiment, the experimentally determined bulk modulus of ZrO_2 is in fact larger than that of CeO_2 (242 versus 204 or 236 GPa), but the calculated difference (270 versus 221 GPa) appears slightly overestimated.

A closer examination of the elastic constants C_{11} and C_{12}, reported in tables 4.6 and 4.18, shows that in ceria both of the calculated values (and therefore the value of the bulk modulus) are close to the measured ones; in zirconia, C_{11} is systematically overestimated in all of the calculations, both *ab initio* and interatomic potential. The calculated value of C_{12} is always smaller than the measured ones. Improving the basis set used in the calculations, by using instead the 8-411dG oxygen basis set does not modify the description of C_{11} and C_{12}. Where the extended oxygen basis set considerably improves the results is in the description of the third elastic constant, C_{44}. As noted in the previous section, neighbouring oxygen ions relax towards one another during the C_{44} distortion, and we therefore expect an accurate description of the oxygen

polarisation to be especially important in reproducing this "softer" distortion of the material.

Since the improved oxygen basis set introduced little change in the calculated equilibrium geometry and in the C_{11} and C_{12} elastic constants, in the remainder of the study we shall use only the Hay and Wadt ECP and the simpler 8-51G oxygen basis set; this choice minimises the computational requirements, which is especially important for the surface studies.

Figures 4.5 and 4.11 give the CRYSTAL HF calculated band structures for CeO_2 and c-ZrO_2 respectively; the path along which this band structure is calculated is illustrated in figure 4.7 – passing through the four high symmetry points present in the fluorite structure: the origin, [1,0,0], and [1,1,0] and [1,1,1].

It is clear in these band structures that the topology of the energy bands in reciprocal space is identical in both ceria and zirconia, which suggests that they have similar qualitative features to the metal-oxygen interactions. Quantitatively, however, we expect them to differ: in particular the hybridisation of the metal and oxygen valence orbitals due to the increased covalence of zirconia in comparison to ceria.

Zirconia is calculated to have a slightly smaller band gap than ceria (13.21 eV versus 14.01 eV), as expected since the Zr 4*d* orbitals are closer in energy to the oxygen 2*p* atomic orbitals than the cerium 5*d* orbitals are. In reality, the band gap of ceria is less than that of zirconia, due to an oxygen 2*p* to Ce 4*f* transition. We recall however that we represented the Ce^{4+} as a f^0 ion, and the Ce(4*f*) bands, which are the lowest unoccupied levels in the solid, are not present in our calculations; nevertheless the latter are not expected to influence strongly the bonding in the solid as the *f* electrons are highly localised on the metal sites. Due to the lower $p \rightarrow d$ band gap, the hybridisation of the metal *d* and oxygen 2*p*-orbitals is more effective in zirconia, making it a more covalent material than ceria. This latter effect is apparent in the much larger calculated valence band-width of zirconia compared to ceria (7.43 eV and 5.35 eV, respectively).

The oxygen-oxygen interactions overlap the effect of metal-oxygen covalence in the valence band (VB); interoxygen repulsion, if present, causes the top of the VB to be shifted to higher energy levels. If we examine the band structures of bulk ceria and zirconia (in figures 4.5 and 4.11), we can see that this latter effect is indeed present, and

is much larger in ZrO_2 than it is in CeO_2. The uppermost energy level of the valence band at the *M* point (0,1,1) of reciprocal space is in fact destabilised in energy due to anti-bonding combinations of the 2*p* levels on neighbouring oxygens.

4.6 Conclusions

The calculations reported in this chapter have demonstrated that both ceria and zirconia are largely covalent materials, with ceria being more ionic than zirconia. The calculated HF Mulliken charge of the Ce ions in stoichiometric ceria was +3.461 |e|, while that of the Zr ions was +2.788 |e|. The greater degree of covalence present in zirconia was also evident in the electron density plots reported here, and in the calculated (HF) band structure of the bulk phase: even though the topology of the energy levels in reciprocal space was identical in both materials, the degree of dispersion in the oxygen 2*p* bands in ZrO_2 was much greater than that observed in CeO_2. The HF Hamiltonian greatly exaggerates the calculated band gap of the material, as is always the case, with the bang gap of ceria being calculated as 14 eV and that of zirconia as 13.4 eV. The experimental band gaps for both materials lies in the range of 4-6 eV.

In addition, the calculated Density of States (and the associated projections onto the metal and oxygen ions) provided evidence that the energy states immediately below the Fermi level were due mostly to the oxygen 2*p* levels, while those immediately above the Fermi level were due to the metal *d* bands, in both ceria and zirconia. The DOS calculated with the plane wave code CASTEP illustrated that the Ce *f* levels, which cannot be included into the CRYSTAL calculations at present, lie slightly higher in energy than the *d* levels, and are therefore expected to remain unoccupied in the bulk material.

We also observed that the expansion of the oxygen basis set to the 8-411dG set, which includes additional polarisation functions compared to the standard 8-51G basis set, did not significantly alter the properties of the bulk cubic phase, although it did greatly improve the reproduction of the C_{44} elastic deformation in the material when metal ion relaxation (along the <111> direction) were included. This suggests that the oxygen polarisation functions may play an important role in the displacive cubic-tetragonal phase transition which we shall examine in the following chapter.

5 Ambient pressure phases of zirconia

The previous chapter was concerned with the high symmetry cubic phase that is common to both ceria and zirconia. In the following chapter, I shall examine the two remaining ambient pressure structures assumed by zirconia: the tetragonal (t-ZrO_2), and the monoclinic phases (m-ZrO_2).

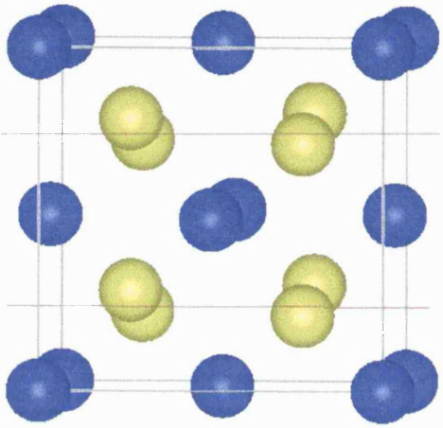

Figure 5.1: A graphical overview of the tetragonal assumed by ZrO_2 under ambient pressure conditions between 1440K and 2600K.

As the temperature begins to fall below 2600K, two distinct processes occur. First the unit cell deforms, with the cell volume increasing by approximately 4% and the c_{tet}/a_{tet} ratio increasing from the value of $\sqrt{2}$ (1.414) observed in the cubic phase. The second process is a uniaxial displacement of the oxygen ions along the [001] direction, by a small amount d_z. Experimental investigations by Aldebert and Traverse (86) determined that the c_{tet}/a_{tet} ratio increases to 1.451, and the oxygen ions displace by $0.057c_{tet}$. In the cubic structure, the vertical position of the oxygens (O_z) is $\frac{1}{2}c_{tet}$.

There is still a great deal of debate as to the true nature of this transformation, and experimental investigations are hampered by the formation of a metastable tetragonal phase on quenching of non-stoichiometric samples of zirconia. This metastable structure has the same space group as the true tetragonal phase, but the presence of the impurities alters the composition of the material and greatly affects experimental observations of the phase transformation. Rather than the simplistic overview of the cubic-tetragonal (c-t) transformation just presented, the formation of the metastable phase is not considered in the investigations of the pure phase in this thesis.

The tetragonal phase is characterised by $a_{tet} = b_{tet} = 3.64$Å, and $c_{tet} = 5.25$Å (86) and the newly formed primitive tetragonal unit cell contains two ZrO_2 formula units (twice as large as the cubic) and is illustrated in figure 5.1. In this image, the red horizontal lines represent the planes $z = \pm ¼\ a_{cub}$, which correspond to the location of the oxygen ions in the cubic fluorite phase.

The volume change accompanying the *c-t* transition is highly undesirable in commercial applications of zirconia – if such an expansion were to occur during the normal heating/cooling cycles experienced in SOFC applications (for example), the device would eventually destroy itself, or at least cause any external coatings to spall away. It is therefore often desirable to prevent such a phase transition from ever occurring, often achieved by using an artificially stabilised phase which is stable over the entire operating temperature range. In addition, ZrO_2 is most often used in Oxygen Storage (or transport) applications, whereby vacancies are introduced onto the oxygen cubic sublattice by doping the material with lower valent cations (often Y_2O_3, CaO, or CeO_2). The process of doping the material also has the additional advantage in that it stabilises the cubic phase at much lower temperatures than present in the stoichiometric ZrO_2 – often as low as room temperature in some cases, as well as significantly improving the mechanical strength and toughness of the material.

5.1 The Idealised c-t Phase Transition

As previously mentioned, the *c-t* phase transition can be fully characterised by a displacement of the oxygen ions away from their high symmetry cubic lattice sites, and subsequent relaxation in both the unit cell volume and the c_{tet}/a_{tet} ratio. To attempt to better understand the chemical effects which help stabilise the tetragonal phase (with respect to the cubic phase), we examined at great length the physical and electronic changes which occur in the material on transformation from the cubic phase. A model of the full deformation is somewhat complex, so it was decided to perform an initial analysis of an 'idealised' cubic-to-tetragonal transformation, in which the cell volume and c_{tet}/a_{tet} ratio were kept fixed at their optimised cubic values, although the oxygen ions were slowly displaced away from their high symmetry sites. The cubic structure can be represented in the tetragonal structure space group by setting the c_{tet}/a_{tet} ratio to $\sqrt{2}$ and having $c_{tet}=a_{cub}$.

Although such a model is not able to provide a quantitative analysis of the transformation, it is our belief that the displacement of the oxygen ions is the key process in better understanding the relative stabilities of the two phases.

Figure 5.2: The energy changes observed during the idealised cubic-tetragonal phase transition.

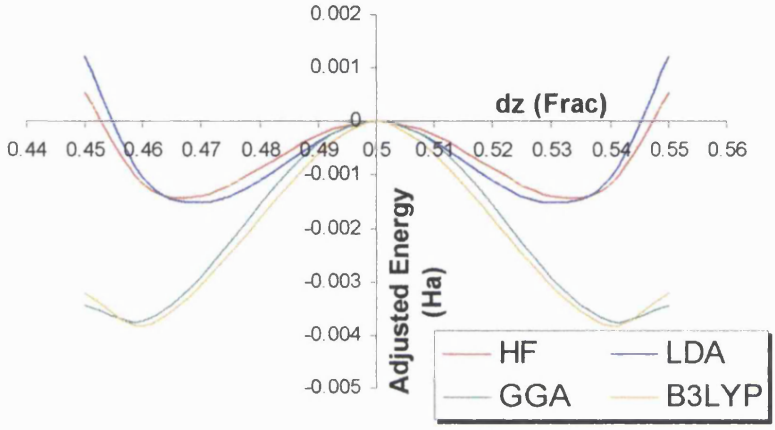

The simplest property which we can study in our idealised model is the changes in the internal energy of the system as the deformation begins: for the transformation to occur naturally, there must be an overall reduction in the internal energy as the oxygen ions displace (by an amount d_z) away from their equivalent positions in the cubic phase. Figure 5.2 shows graphically the energy double well obtained in our model from calculations using both the HF and DFT Hamiltonians;* a similar profile was originally obtained from the Full potential Linear Augmented Plane-Wave (FLAPW) LDA calculations by Jansen in collaboration with Gardner (87), and again later in Reference (88). A similar profile is obtained in all high quality *ab initio* studies performed today and is generally well accepted.

In this figure, the internal energy obtained from each of the four Hamiltonians examined was normalised so that the zero of the energy was that of the geometry optimised cubic phase, in order that the four schemes may be better compared to each other. Negative values on this scale correspond to configurations having lower energies

* All calculations in this section shall make use of the Hay and Wadt small-core pseudopotential and oxygen 8-411dG basis sets unless stated otherwise.

than the cubic structure, and are therefore thermodynamically more stable. The presence of a minimum energy point for oxygen away from the central $d_z = ½$ point confirms that the tetragonal phase is predicted to be (thermodynamically) more stable than the cubic in our idealised model. Since this model only represents a small part of the total transformation, the energy changes reported in figure 5.2 are much smaller than we would expect from a complete transformation (see section 5.1 for the fully optimised tetragonal phases), however qualitatively the analysis is appropriate.

Figure 5.2 shows an obvious discrepancy between the HF/LDA calculations and the GGA/B3LYP calculations, with the GGA-based Hamiltonians providing a much larger energy change, and a slightly greater minimum energy oxygen ion displacement than the HF or LDA calculations.

In the work by Fabris, *et al* (56), tight binding parameters were derived to model the cubic-tetragonal phase transition. They found that an additional polarisation parameter was required on the oxygen ions in order to correctly model the transition; their study provided an optimised geometry in good agreement to the GGA/B3LYP Hamiltonians in our current work. On removal of this additional polarisation parameter, the geometry of the fully relaxed tetragonal phase in this case was more like the HF/LDA situation found here; a result which suggested that the HF and LDA Hamiltonians were providing an inadequate description of the oxygen polarisation in our present model.

To determine if this was the case, we examined the change in the dipole moment on the oxygen ions during the idealised cubic-tetragonal phase transition: as we can see from figure 5.3, there is no discernable difference between the different Hamiltonians – suggesting that each level of theory provides an equally good representation of the oxygen polarisability and that the difference between the HF/LDA and GGA/B3LYP schemes must be due to some other factor.

Figure 5.3: The change in the oxygen dipole moment observed during the idealised *c-t* phase transition.

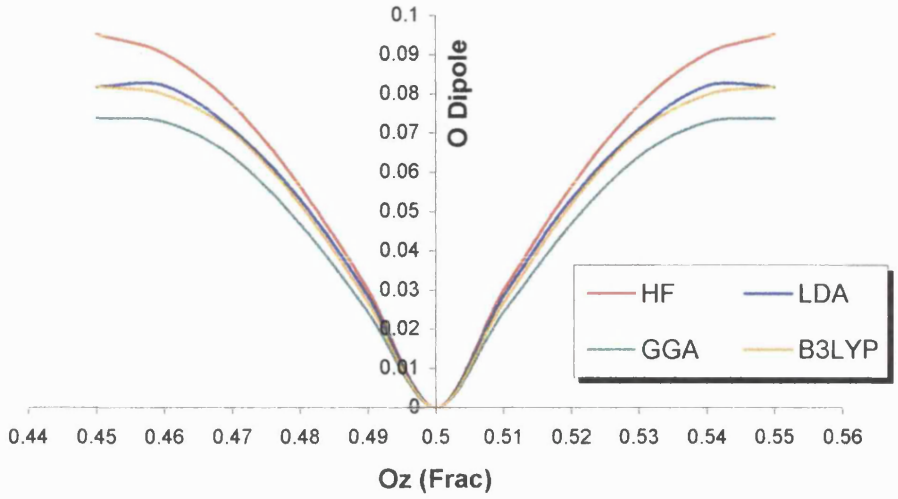

Table 5.1: Electronic properties of the energy minimised tetragonal structure, as obtained from each of the Hamiltonians studied.

	HF	LDA	GGA	B3LYP
Zr Mulliken	+2.793	+2.120	+2.182	+2.341
O Mulliken	-1.397	-1.060	-1.091	-1.170
Zr–O Overlap (short)	+0.034 (2.137Å)	+0.070 (2.110Å)	+0.077 (2.118Å)	+0.067 (2.116Å)
Zr–O Overlap (long)	+0.035 (2.315Å)	+0.052 (2.285Å)	+0.050 (2.355Å)	+0.046 (2.353Å)
O–O Overlap (short)	-0.057 (2.567Å)	-0.048 (2.534Å)	-0.032 (2.575Å)	-0.039 (2.572Å)
O–O Overlap (long)	-0.052 (2.585Å)	-0.045 (2.552Å)	-0.027 (2.608Å)	-0.033 (2.605Å)

In calculations performed using the 8-51G basis set, the cubic phase was found to be more stable than the tetragonal, which we attributed to an inadequate description of the oxygen polarisability. Table 5.1 lists the calculated bond populations determined using the Mulliken analysis in this idealised tetragonal structure; while results of this analysis as the idealised distortion progresses are shown graphically in figure 5.4 for the shortest O-O interaction; the longer O-O interaction is in the direction of the ion displacement; this separation remains unchanged during the phase transition. For reference, the equivalent table for the fully optimised tetragonal structure is given in the following section, in table 5.3. We note that the ionic Mulliken charge is approximately equal in both the idealised and fully optimised structures, and only minor discrepancies exists

between the bond populations predicted in each case. From this we can conclude that the idealised model of the phase transition is of a sufficient accuracy to enable a detailed examination of the phase transition to be performed.

In figure 5.4, the bond population has been normalised so that the cubic phase lies at the zero point. We see a clear distinction between the DFT calculations and those performed using the HF Hamiltonian: O-O interactions under the HF Hamiltonian become more negative as the distortion progresses, or as the cubic phase distorts. This suggests that short-range hard-ion repulsion effects may be influencing the displacement of the oxygen ions: in effect the oxygen ions are already impacting upon one another in the cubic structure and any reduction in their separation is greatly unfavourable on energetic terms. If this is the case, it would clearly restrict the stabilisation of the tetragonal phase and lead to the negative Mulliken O-O bond populations observed here.

Figure 5.4: Variation in O-O bond population with idealised c-t transition. Results for the shortest O-O band are shown.

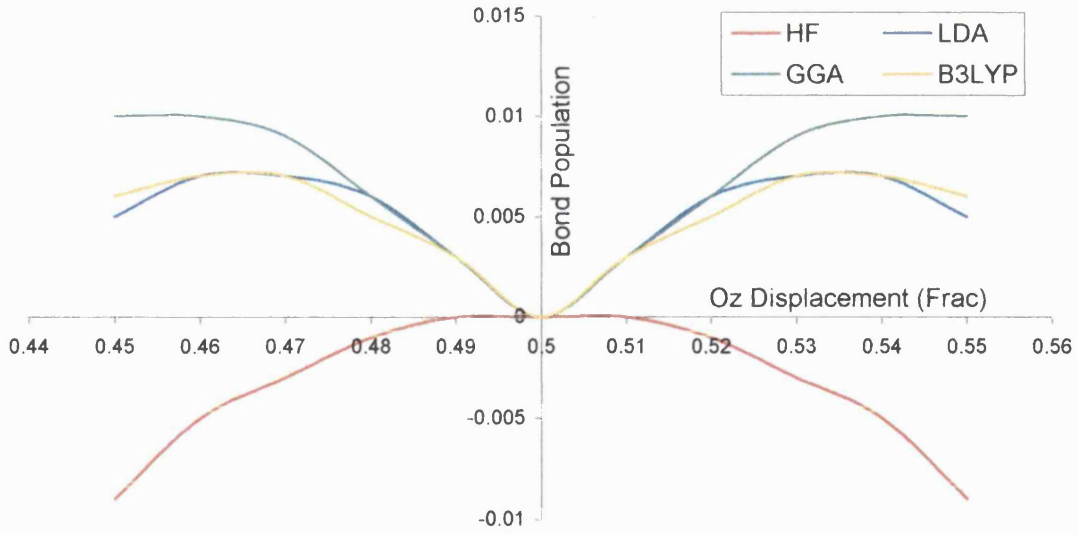

We also note that there was no evidence of this effect in any of the DFT calculations performed here, including those using LDA. As the optimal lattice parameters of the LDA structures are less than the experimental (a common trend), we could expect that this effect would be the cause of the close agreement between the HF and the LDA idealised *c-t* energetics (in figure 5.2). However, we found no evidence of this in the calculations performed, suggesting the correlation to be merely coincidental, although

the smaller cell volume of LDA calculations is believed to be the most probably cause for the low energy barrier between the two phases: as the LDA Hamiltonian underestimates the bulk lattice parameter, the displacement of ions in such a compressed structure is energetically unfavourable compared to the much larger geometries obtained from the other Hamiltonians studied.

5.1.1 The Stability of Tetragonal Ceria

In this section I aim to briefly outline the stability of ceria in a similar tetragonal phase as zirconia. Experimentally there is just a single structure for CeO_2, the common deviation from this being the formation of the reduced oxide Ce_2O_3. It is our belief that the simplest deformation which could occur in CeO_2 is that of the *c-t* transition, and so in a similar manner to the zirconia study just examined, we displaced the oxygen ions in the fluorite structure away from their high symmetry positions. The resulting energy profile (obtained using the Hay-Wadt pseudopotential and oxygen 8-411dG basis set) is shown below in figure 5.5.

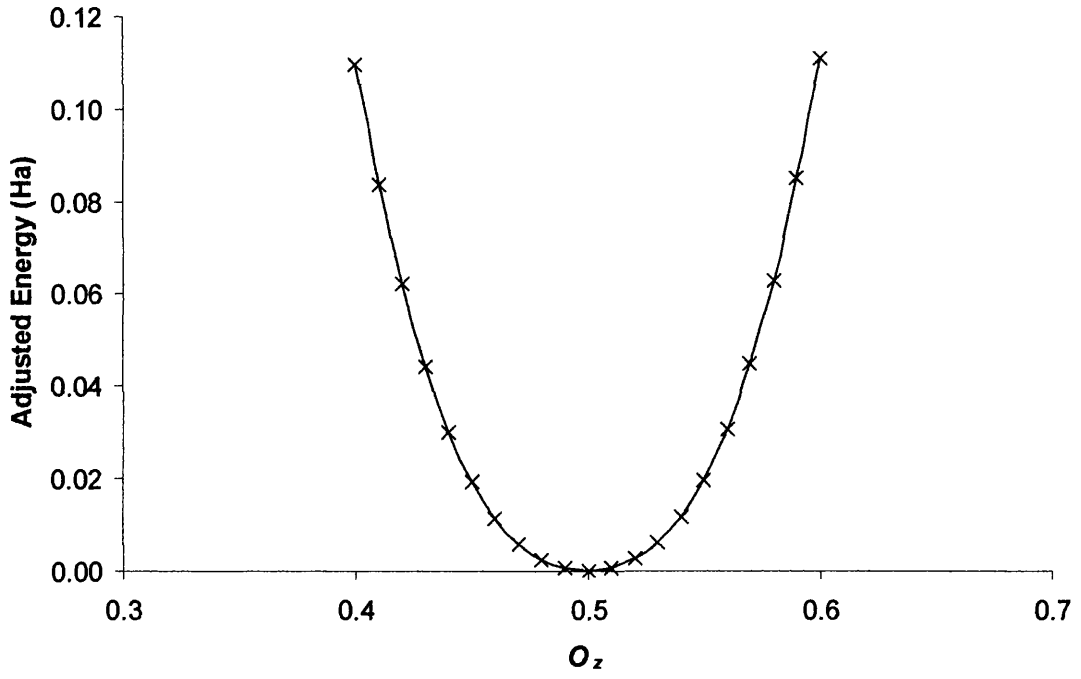

Figure 5.5: Energy surface obtained for the distortion of (cubic) ceria to the tetragonal structure. Energies are normalised so that the cubic phase is zero, and positive values are higher energy configurations. The cubic phase is characterised by $O_z = ½$ ($d_z = 0$).

By comparison to the profile obtained with zirconia (see figure 5.2), we immediately note that absence of the 'double well', first predicted by Jansen (87,88), in the model of the deformation analysed here. The minimum energy configuration of ceria is in fact predicted to be the cubic fluorite phase. The gradient of the energy surface is quite steep, an oxygen ion displacement of $0.05c_{tet}$ (close to the minima observed in zirconia) would result in an increase in the internal energy of around 0.06 Ha in ceria, and the energy continues to increase rapidly as the oxygen ions are further displaced, presenting a significant barrier to the formation of the tetragonal phase – a result in line with the experimental observation that this phase is not thermodynamically stable.

5.2 Tetragonal ZrO_2

In this section I shall present results from a complete geometry optimisation of the tetragonal phase using both HF and DFT Hamiltonians in the CRYSTAL code.

Table 5.2: Optimised parameters for the tetragonal phase of ZrO_2.

QM Functional	a_{tet}/c_{tet} (–)	O_z (fractional)	ΔV ($Å^3/ZrO_2$)	B (GPa)	ΔE (mHa/ZrO_2)
HF/8-411d HW	1.427	0.035	0.6241	266	0.58
HF/8-51d HW	1.415	0.003	0.3363	—	-0.03
HF/8-51d SP	1.417	0.006	0.0696	—	0.50
LDA/8-411d HW	1.424	0.035	0.4444	260	0.87
GGA/8-411d HW	1.441	0.048	0.7849	236	2.83
B3LYP/8-411d HW	1.440	0.049	0.7016	250	2.80
Orlando HF (51)	1.478	0.065	1.3706	236	7.30
Stapper PW (58)	1.435	0.042	0.6624	197	1.76
Carter PW (59)	—	0.033	<1%	—	>0
Jansen FLAPW (87,88)	1.425	0.029	—	—	2.20
Finnis LMTO (57)	1.434	0.051	0.7157	—	1.80
Fabris TB (56)	1.442	0.047	0.6416	—	1.51
Cohen PIB (89)	—	—	—	179	—
Jomard PW/LDA (90)	1.456	0.050	0.8800	—	0.75
Jomard PW/GGA (90)	1.468	0.060	1.3600	—	2.97
Experiment (86)	1.451	0.057	0.7650	—	—
Experiment (43,91,92)	1.426	0.057	—	151-194	2.10

KEY:
FLAPW — Full potential Linear Augmented Plane Wave. Jansen's work in References (88) used an LDA Hamiltonian
LMTO — Linear Muffin-Tin Orbital
TB — Tight Binding
PIB — Potential Induced Breathing
PW — Plane Wave
HW Hay and Wadt small-core Zr pseudopotential
SP Stoll and Preuss small-core Zr pseudopotential

In order to fully model the *c-t* phase transition, the changes in unit cell volume and c_{tet}/a_{tet} ratio must be examined in addition to the oxygen ion displacement studied in the idealised model. Table 5.2 lists the optimised parameters for the tetragonal phase determined with each of the Hamiltonians studied here, in comparison to the optimised geometries determined in other theoretical and experimental studies.

In table 5.2, we have defined the energy difference for the cubic-tetragonal transformation through equation (5.1), as the change in the internal energy between the two fully optimised structures. In this notation positive values of ΔE represent a cubic phase higher in energy than the tetragonal, and therefore less thermodynamically stable. With the exception of the HF/8-51G calculations, all of the studies reported in table 5.2 correctly place the cubic phase higher in energy than the tetragonal, in line with the zirconia phase diagram (see figure 4.2).

$$\Delta E = E_{cubic} - E_{tetragonal} \qquad (5.1)$$

We note a clear correspondence of the HF and LDA optimised geometries, while the GGA/B3LYP schemes provide much larger distortions of the cubic cell during the relaxations. The restricted relaxation in the HF/LDA calculations results in a calculated energy difference between the cubic and tetragonal phases which is much smaller than determined in the other theoretical and experimental studies which are available to us, with the sole exception of the results reported by Jomard *et al.* (90) who performed plane wave calculations using both the LDA and GGA Hamiltonians in the VASP (93) program. Although Jomards' LDA calculations yielded larger changes in both the value of c_{tet}/a_{tet} and the equilibrium oxygen displacement than either the current LDA calculations or the early LDA work by Jansen (87,88), the energy change predicted for the transformation by Jomard is, in fact, remarkably similar to the value which was obtained in our own LDA calculations.

It should also be noted that the GGA/B3LYP calculations provide a very good agreement to the optimised plane-wave geometries obtained by Stapper *et al.* (58), Carter *et al.* (59), and also to the tight-binding (TB) calculations of Fabris *et al.* (56)

Table 5.3: Electronic properties of the optimised tetragonal phase with each of the Hamiltonians studied.

	HF	LDA	GGA	B3LYP
Zr Mulliken	+2.805	+2.123	+2.185	+2.338
O Mulliken	-1.403	-1.061	-1.092	-1.169
Zr–O Overlap (short)	+0.026 (2.133Å)	+0.072 (2.105Å)	+0.081 (2.110Å)	+0.068 (2.106Å)
Zr–O Overlap (long)	+0.026 (2.343Å)	+0.051 (2.312Å)	+0.047 (2.403Å)	+0.044 (2.378Å)
O–O Overlap (short)	-0.096 (2.594Å)	-0.042 (2.557Å)	-0.023 (2.627Å)	-0.034 (2.595Å)
O–O Overlap (long)	-0.095 (2.596Å)	-0.041 (2.564Å)	-0.023 (2.627Å)	-0.031 (2.615Å)

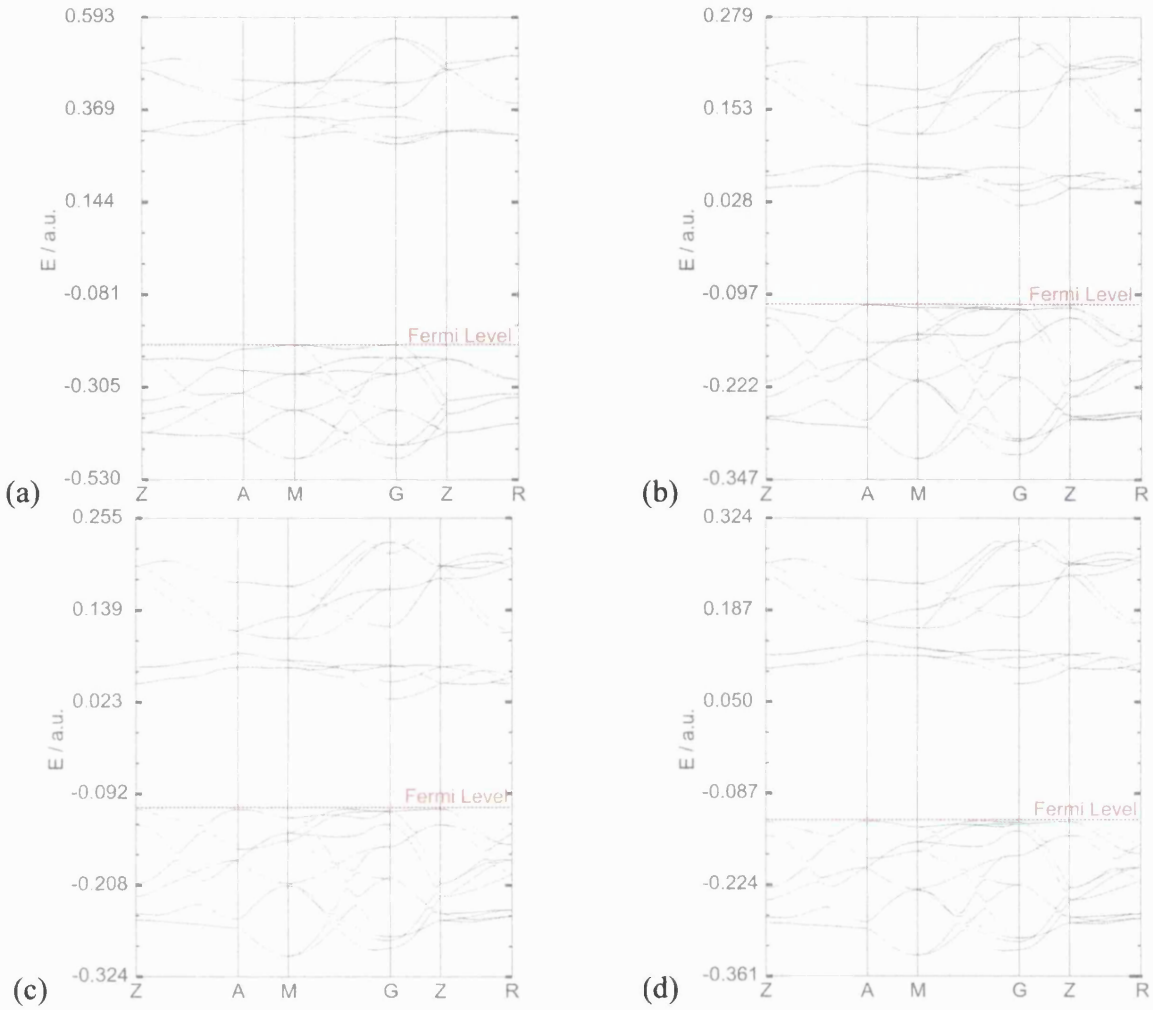

Figure 5.6: Calculated band structures obtained from the fully optimised tetragonal zirconia structures using (a) Hartree-Fock, (b) LDA, (c) GGA and (d) B3LYP Hamiltonians in the CRYSTAL program.

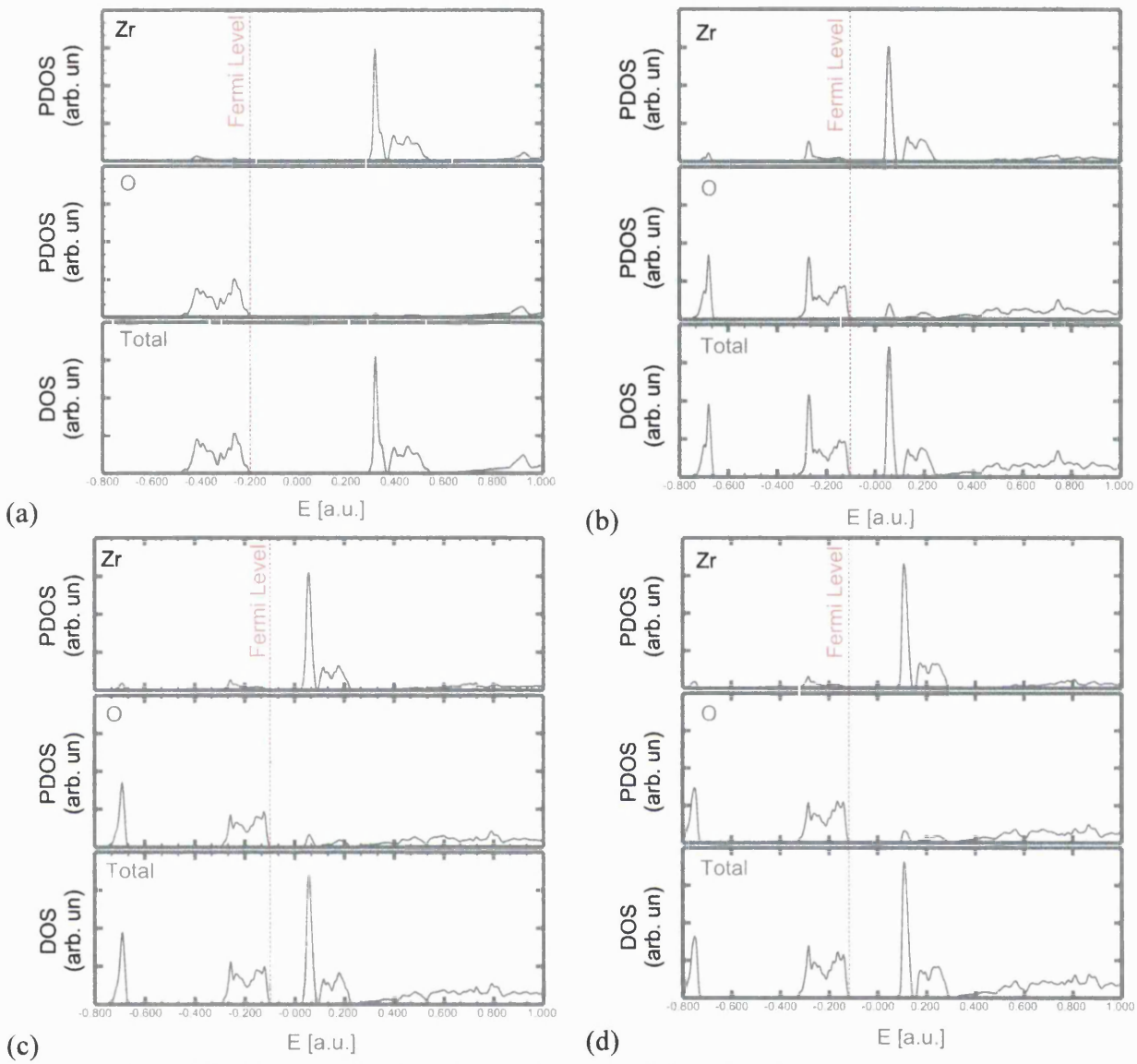

Figure 5.7: Calculated density of states of tetragonal zirconia, using (a) Hartree-Fock, (b) LDA, (c) GGA and (d) B3LYP Hamiltonians in the CRYSTAL program. For each Hamiltonian, we report the total DOS and its projections onto the oxygen and zirconium basis sets, as labelled.

The calculated band structures for t-ZrO_2 are given in figure 5.6, and the corresponding DOS plots in figure 5.7. A summary of the points in reciprocal space used in the band structure plots is shown for reference in table 5.4. On examining figure 5.6, we note initially, that the topology of the energy levels predicted by all the Hamiltonians employed to study the tetragonal phase appears identical, although the energy scales of these plots differs greatly in each case. The calculated electronic properties for each of the Hamiltonians available are listed in table 5.5, and clearly show the Hartree-Fock calculations as providing a theoretical band gap energy very much

greater than any DFT study, although in good agreement with the previous HF study by Orlando *et al.* of around 13.3 eV. This overestimation is expected from the Hartree-Fock Hamiltonian, as mentioned in the previous chapter; the LDA calculations show instead the opposite behaviour and underestimate the experimental band gap – which varies between 4 and 6 eV, depending on the purity of the sample used and the method used to measure the band gap. The agreement between our current LDA calculations and the plane-wave LDA calculations by Jomard again confirms this is a systematic feature of the LDA Hamiltonian, rather than a particular deficiency in the CRYSTAL calculations.

The calculated DOS confirms that, as in the cubic phase, the energy bands immediately beneath the Fermi level are due primarily to the oxygen (i.e. 2*p*) levels, while the first set immediately above the Fermi level are due mainly to the Zr levels (i.e. 4*d*), a configuration we would expect to observe in a largely ionic material. The calculated HF band gap of this phase is remarkably similar to that calculated for the cubic phase, as we would expect given the similarities between the two materials and the poor performance of the HF Hamiltonian on the calculated band gap; of the DFT Hamiltonians studied here, the tetragonal band gap is slightly higher than that calculated for the cubic phase (see table 4.22 on page 88 for the calculated band gaps of the cubic phase). In both phases, LDA and GGA provide a roughly equal band gap, ~3.7 eV in the tetragonal, and ~3.2 eV in the cubic phase; a similar trend is observed in the B3LYP calculations, where the band gap is 4.9 eV in the cubic phase and 5.6 eV in the tetragonal phase. From these results we conclude that the band gap of the tetragonal structure is approximately 0.5 eV higher than that of the cubic phase.

Table 5.4: Description of the labels used in plotting the tetragonal band structures.

Coordinates in Brillouin Zone	Label of Point
½[0, 0, 0]	G (the Γ point)
½[0, 0, 1]	Z
½[1, 1, 1]	A
½[1, 1, 0]	M
½[1, 0, 1]	R

Table 5.5: Electronic properties of optimised tetragonal ZrO_2 with each of the Hamiltonians studied.

QM Functional	*Q(Zr)* (|e|)	*Q(O)* (|e|)	*Qb(ZrO)* (|e|)	*Qb(OO)* (|e|)	*Band Gap* (eV)
HF/8-411d HW	+2.991	-1.496	+0.012	-0.070	13.28
HF/8-51 HW	+2.991	-1.495	+0.012	-0.071	13.33
HF/8-51 SP	+2.926	-1.463	+0.007	-0.073	13.28
LDA HW	+2.123	-1.061	+0.072	-0.042	3.67
GGA HW	+2.185	-1.092	+0.081	-0.023	3.78
B3LYP HW	+2.338	-1.669	+0.068	-0.034	5.60
Orlando HF (51)	+3.285	-1.642	-0.010	-0.036	13.30
Carter (PS-B) (59)	1.020	-1.440	—	—	—
Jansen (87,88)	+2.820	-1.470	—	—	—
Králik GW (83)	—	—	—	—	6.40
Jomard LDA (90)	—	—	—	—	3.90
Experiment	—	—	—	—	5.78 (94) 4.2 (95)

It is of interest to note the close correspondence of the B3LYP calculated band gap energy (5.60 eV) to that obtained by Králik *et al.* Although Králik initially used an LDA scheme to obtain the original band structure, he made a modification to the calculated energy levels using a recent GW quasiparticle approximation. Limited experience exists as to the applicability of this modification in situations such as these, although theoretically the quasiparticle approach should provide the best description of the electronic band structure which we can hope to produce in any *ab initio* calculation. As the figure reported by Králik is within the range of figures determined by experiment, then this would appear to be the case. The current B3LYP calculations also provide a remarkably similar band gap energy to this, suggesting the B3LYP Hamiltonian does perform better than was originally anticipated in zirconia.

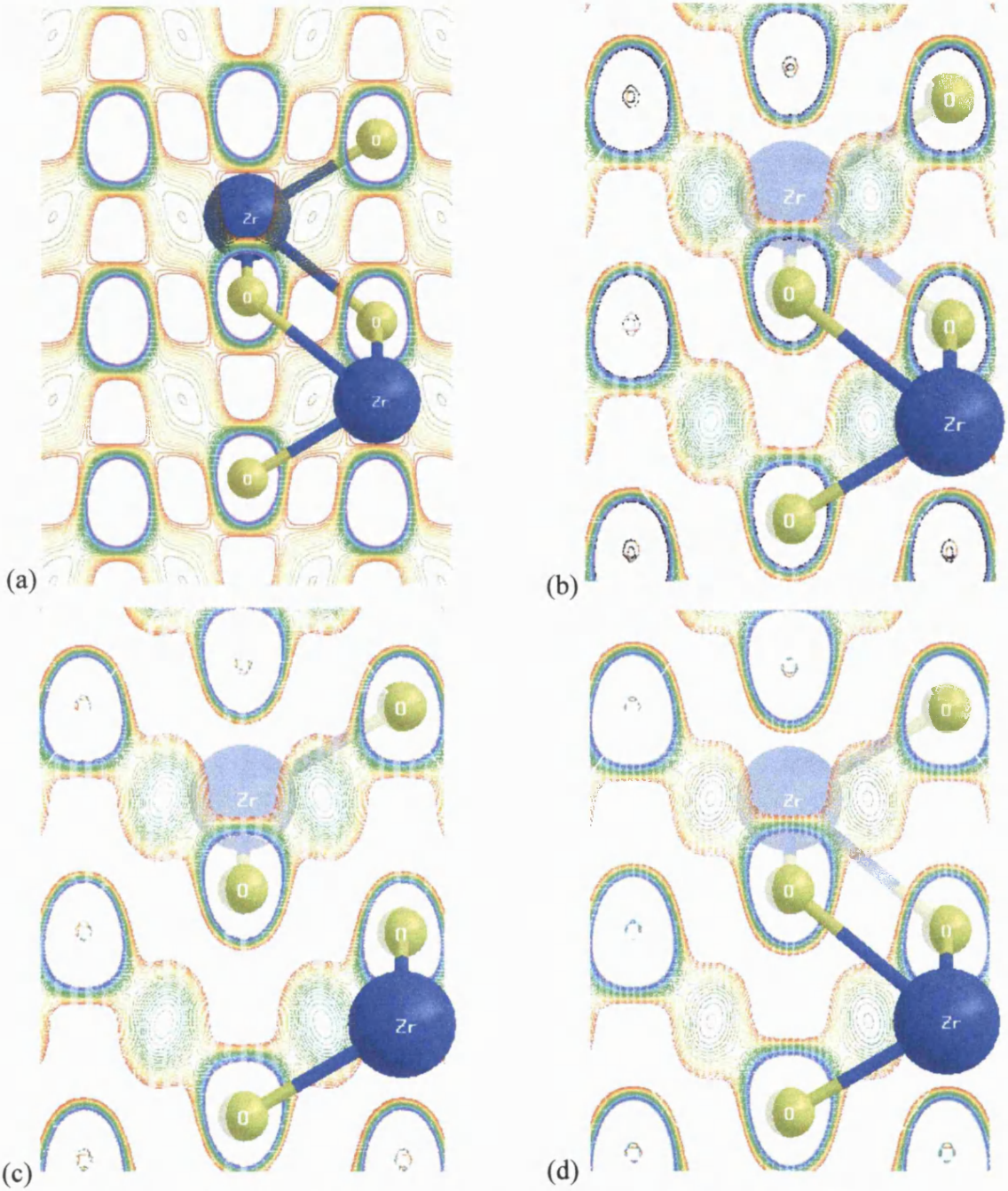

Figure 5.8: Calculated electron density difference plots calculated for tetragonal zirconia, using (a) Hartree-Fock, (b) LDA, (c) GGA and (d) B3LYP Hamiltonians. The cross-section shown here is taken parallel to the {001} plane, intersecting the oxygen ions. The coloration of the contours is the same as for all previous electron density plots, and the contours range from -0.005 |e| to 0.005 |e|, with 30 contours being used to evenly span this range.

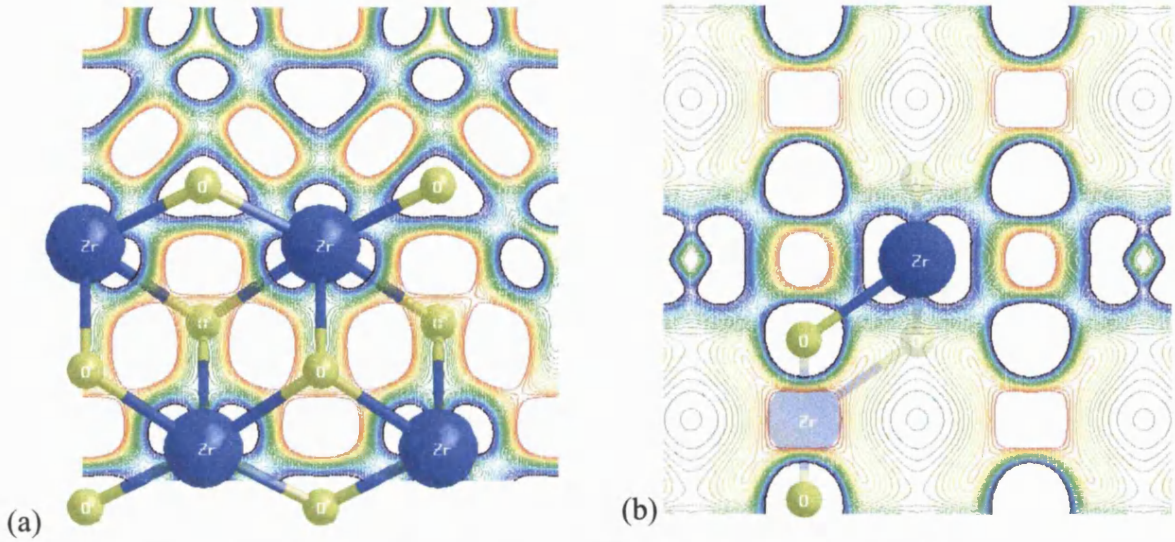

Figure 5.9: Calculated electron density difference plots calculated for tetragonal zirconia, using the cross-section taken parallel to the (a) the {001} plane, intersecting the metal ions, and (b) {011} plane, intersecting both metal and oxygen ions.

Electron density plots (which again have the electron density due to isolated ions at the lattice sites subtracted from the total calculated electron density) of the tetragonal zirconia phase are given in figures 5.8 and 5.9, for the HF, LDA, GGA and B3LYP optimised tetragonal structures. All of these images use the same contour range and spacing: the blue/purple contours indicate zones of highly negative difference electron density (-0.005 |e|), while the red/orange contours represent the larger positive densities (+0.005 |e|); the range was then spanned linearly by thirty individual contours.

Figure 5.8 shows the electron density across the oxygen-oxygen {001} plane; the zirconium ions illustrated here lie above and below the plane through which the electron density is calculated (but are given in the figure for reference). There is a clear anisotropy between the two distinct oxygen-oxygen bond lengths: the *c-t* phase transition involves a shortening of half the oxygen-oxygen bonds and a lengthening of the remaining half; as schematic illustrated in this figure, the phase transition involves the oxygen ions moving vertically in the plane of the image: the two left hand oxygens move upwards and the two right hand oxygens move downwards.

The shortened oxygen-oxygen separation is clearly indicated by the greatly increased electron density in the [110] direction in this plane, the dense region of negative (cyan/green) contours indicates that charge is transferred into the inter-oxygen region during formation of the crystal (relative to isolated gaseous ions), compared to the cubic

phase (which showed a more restricted oxygen repulsion in the same region, see figure 4.24). Ion separation in the vertical direction remains relatively unchanged from that of the cubic, only increasing slightly due to the volume increase in the c_{tet}/a_{tet} deformation.

5.3 Monoclinic ZrO_2

The monoclinic polymorph, shown in figure 5.10, cannot be characterised by a simple structural distortion from the other two ambient pressure phases; it is formed instead during a reconstructive phase transition from the tetragonal phase. It is also rather unusual in that it contains a seven-fold coordinated Zr ion and a three-fold coordinated oxygen ion (labelled A in figure 5.10) in its primitive unit cell, which contains four ZrO_2 formula units and is therefore four times as large as that of the cubic structure. The affinity which Zr(IV) appear to have for lower-coordinate geometries is caused by the relative size of the Zr(IV) ion in comparison to the lattice site it occupies. Using a simplistic 'radius-rules' approach, the Zr ion appears slightly too small for a pure fluorite structure, but yet too large for a rutile structure as observed in SnO_2. This effect could explain the appearance of the seven-coordinate metal ions in the monoclinic phase and its unexpected stability over the high symmetry cubic or tetragonal phases.

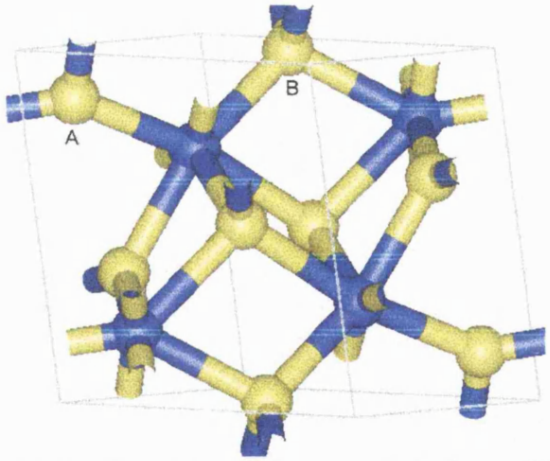

Figure 5.10: A graphical overview of the monoclinic phase of ZrO_2 stable for temperatures below 1440K.

Experimental work by Teufer (96) found that the monoclinic phase is characterised by a_{mono} = 5.15Å, b_{mono} = 5.27 Å, c_{mono} = 5.67 Å, γ_{mono} = 99.23°(internal ion coordinates, are listed in table 5.6). Until recent *ab initio* studies became practical to perform, no theoretical study (the majority being based on IP methods) had been able to predict the

correct order of stability of the three phases. In this thesis, the energy difference between the monoclinic and the cubic phase has been defined through equation (5.2), where all calculated internal energies are quoted per formula unit. This definition is such that positive values of $\Delta E_{c\to m}$ refer to schemes in which the monoclinic phase is predicted to be thermodynamically more stable than the cubic (the experimental observation).

$$\Delta E_{c\to m} = E_{cubic} - E_{monoclinic} \tag{5.2}$$

The monoclinic phase has been optimised here using both Hartree-Fock and DFT Hamiltonians, the latter employing LDA, GGA and B3LYP formulations of the exchange and correlation energies. The work reported here is the only many-Hamiltonian study of the monoclinic phase .Due to the complexity of this phase, it was found that the auxiliary basis sets used on ions in the earlier density functional calculations required an additional set of *f* and *g*-type orbitals in order to accurately sample the calculated electron density in the DF fitting. These additional orbitals were completely unused in the cubic and tetragonal systems due to the symmetry of the crystal, preventing polarisation effects that required their presence. This was checked and confirmed in order to validate our use of the simpler auxiliary basis in the earlier calculations.

Table 5.6: The optimised parameters obtained for the monoclinic phase. $\Delta E_{m\to c}$ is the energy difference (in mHa) between the monoclinic phase and the cubic, the sign of $\Delta E_{m\to c}$ is detailed in the text.

	Current Work				
	HF	GGA	B3LYP	LDA	Experiment (86,97)
a_{mono}	5.2370	5.2433	5.2468	5.1794	5.1505
b_{mono}	5.2482	5.2632	5.2563	5.1936	5.2710
c_{mono}	5.3638	5.4016	5.4019	5.3049	5.6717
γ_{mono}	99.230	99.229	99.229	99.228	99.23
x_{Zr}	0.2733	0.2757	0.2752	0.3047	0.2754
y_{Zr}	0.0383	0.0438	0.0417	0.0546	0.0395
z_{Zr}	0.2082	0.2115	0.2098	0.2156	0.2083
x_O	0.0669	0.0673	0.0649	0.0565	0.0700
y_O	0.3244	0.3289	0.3237	0.3252	0.3317
z_O	0.3553	0.3493	0.3534	0.3457	0.3447
$x_{O'}$	0.4555	0.4548	0.4550	0.4500	0.4496
$y_{O'}$	0.7549	0.7573	0.7569	0.7572	0.7569
$z_{O'}$	0.4785	0.4756	0.4779	0.4773	0.4792
$\Delta E_{c\to m}$ (mHa)	+1.98	+3.07	+4.78	+0.61	+4.41

Table 5.7: Parameters obtained for the monoclinic phase in previous theoretical studies.

		Fabris (56)	Finnis (57)	
	Stapper (58)§	LMTO	TB	Králik (83)
a_{mono}	—	4.983	5.076	5.086
b_{mono}	—	5.163	5.081	5.208
c_{mono}	—	5.267	5.172	5.226
γ_{mono}	—	98.57	98.0	99.21
x_{Zr}	0.277	0.274	0.272	0.278
y_{Zr}	0.043	0.040	0.027	0.042
z_{Zr}	0.210	0.212	0.217	0.210
x_O	0.064	0.069	0.078	0.077
y_O	0.324	0.339	0.336	0.349
z_O	0.352	0.338	0.342	0.331
$x_{O'}$	0.450	0.448	0.452	0.447
$y_{O'}$	0.756	0.753	0.752	0.759
$z_{O'}$	0.479	0.478	0.472	0.483
$\Delta E_{c\to m}$ (mHa)	+4.05	+3.85	+3.70	+4.40

§ The study by Stapper et al. did not optimise the cell volume of the monoclinic phase, only the internal coordinates of the ions. They used the experimental lattice parameters determined by Howard et al. (97) listed above.

Table 5.6 lists the optimised values of the 13 adjustable variables in the monoclinic structure, while table 5.7 shows a comparison to those available in the literature. The extensive plane-wave study by Stapper *et al.* did not allow the monoclinic unit cell volume to relax, instead they optimised only the internal coordinates of the ions beginning with the experimental data provided from the Teufer paper in reference (96).

It is important to note that the current series of calculations have all established the correct order or stability of these ambient pressure phases: $m \rightarrow t \rightarrow c$. The energy difference between the cubic and monoclinic phases, at the Hartree-Fock level was approximately 2 mHa, or 0.054 eV; in tables 5.6 and 5.7, a negative value of $\Delta E_{m \rightarrow c}$ indicates that the monoclinic phase has a lower energy than the cubic – all figures reported here correctly predict that the monoclinic phase is the most thermodynamically stable, in comparison to the cubic. It is interesting to note that the previous theoretical studies of the monoclinic phase by Stapper *et al.* (58), Fabris *et al.* (56), Finnis *et al.* (57) and Králik *et al.* (83) using a variety of Hamiltonians all provide monoclinic-cubic energy differences of around 4 mHa, reasonably similar to the value predicted in the current GGA and B3LYP calculations and in rather good agreement to the experimentally determined 4.41 mHa.

All studies shown here produce values for the internal ion coordinates in excellent agreement to the experimental values, regardless of the method used to study the material. We recall that the work by Stapper did not permit the monoclinic cell to deform from the experimentally determined values, taken from Reference. (97); for this reason we have not quoted those figure in table 5.7. Of the remaining calculations, all appear to predict correctly the cell angle γ, to within 1° of the experimental value. In Reference (57), Fabris and Finnis conclude that it is the covalency of the material which acts to stabilise the monoclinic phase relative to the cubic, rather than the subtle polarisation effects believed to help stabilise the tetragonal phase. The current calculations have determined that the Zr and O ions in the monoclinic phase have lower charges (attributed using the Mulliken scheme and reported in table 5.8) than in the cubic and tetragonal phases, while all metal-oxygen bond populations in *m*-ZrO_2 have large positive values – indicating that the electrons associated with the interactions are most definitely shared between the ions.

Table 5.8: Mulliken population analysis of monoclinic zirconia. $O^{(4)}$ refer to the four coordinate oxygen ions, while $O^{(3)}$ to the three-coordinate oxygens.

Hamiltonian	Zr	$O^{(4)}$	Zr-$O^{(4)}$	$O^{(3)}$	Zr-$O^{(3)}$
HF	+2.792	-1.450	+0.045	-1.342	+0.035
LDA	+2.091	-0.995	+0.088	-1.096	+0.062
GGA	+2.141	-1.122	+0.097	-1.020	+0.068
B3LYP	+2.308	-1.206	+0.088	-1.101	+0.058

Calculations performed at the HF level, and using the smaller 8-51G basis set for oxygen were not able to correctly place the monoclinic phase as the most stable; it is our belief that this is due to the additional degree of freedom allowed by the 8-411G basis to the outer *sp* functions, rather than an inclusion of *d*-polarisation functions into the basis set. In all Hamiltonians studied here, the Mulliken population of the oxygen *d*-levels was at most 0.020 |e| (in the GGA calculations), a negligible amount; in all other cases the *d*-shell population was much lower than this.

Table 5.9: Comparison of the oxygen orbital population in monoclinic zirconia with the 8-51G and 8-411dG basis sets at the HF level.

Oxygen Basis	*Coordination*	*s*	*sp*	*sp*	*sp*	*d*	*Total*
8-51G	3	2.006	4.693	—	2.694	—	9.393
	4	2.006	4.653	—	2.863	—	9.522
8-411dG	3	1.996	2.630	2.639	2.069	0.008	9.342
	4	1.996	2.634	2.556	2.258	0.006	9.450

To test this hypothesis, calculations were performed using both the 8-411dG oxygen basis set, and a 8-411G set constructed by simply removing the additional *d*-functions from the enhanced set. Both predicted an almost identical energy minimised structure, and also that the monoclinic phase is lower in energy than the cubic, the energy difference being approximately 2 mHa with both basis sets. The same result was observed with all four Hamiltonians studied here. On the contrary, we saw in the previous section that polarisation functions on the oxygens are more crucial to describe the phase transition between the cubic and tetragonal structures. Calculations with an inadequate representation of the oxygen basis functions, in fact, did not correctly establish the tetragonal phase as the most stable. The latter results, therefore, appear to confirm the conclusions made by Finnis *et al.*, i.e. that polarisation effects are more important in the tetragonal phase.

In the HF calculations, the Mulliken population of the orbitals in the oxygen basis are listed in table 5.9, and clearly show that the population of the oxygen *d*-functions is negligible, while the major differences are localised into the outer *sp* shells. The addition of the second set of *sp* shells seems to allow the '41' split set to contain a greater electron density than a single set of '5' Gaussians.

Table 5.10: Description of the labels used in plotting the monoclinic band structures.

Coordinates in Brillouin Zone	Label of Point
½[0, 0, 0]	G (the Γ point)
½[0, 0, 1]	Z
½[0, 1, 0]	Y
½[-1, 1, 0]	A
½[-1, 0, 0]	B
½[0, 1, 1]	C
½[-1, 0, 1]	D
½[-1, 1, 1]	E

Table 5.10 details the eight high symmetry points of the monoclinic reciprocal lattice through which the band structures shown in figure 5.11 are plotted. The corresponding DOS for this phase calculated here is given in figure 5.12. The topology of the calculated band structures with all Hamiltonians studied here, using the relevant optimised geometry, were identical and so only that obtained for the HF Hamiltonian is shown in figure 5.11. This plot shows a great many individual energy levels, many more than the previous band structures on the cubic and tetragonal phases; the reason for this is that the monoclinic unit cell contains four formula units, and therefore here we show the four times as many energy levels as was given in the cubic band structure. The DOS plots show that the energy levels immediately below the Fermi level are due to the oxygen levels, while those above are due to the zirconium level: the same trend as was found in the other two ambient pressure phases.

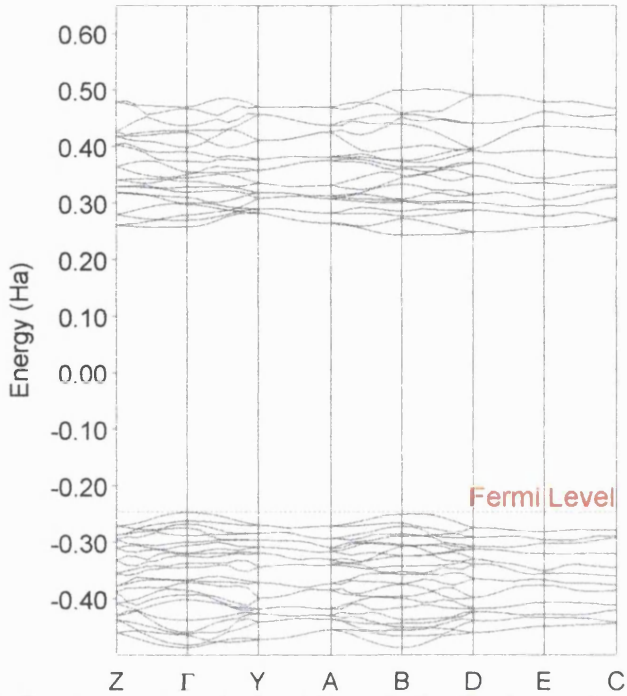

Figure 5.11: Band structure calculated for *m*-ZrO_2. The image shown here was obtained from the geometry optimised using the HF Hamiltonian.

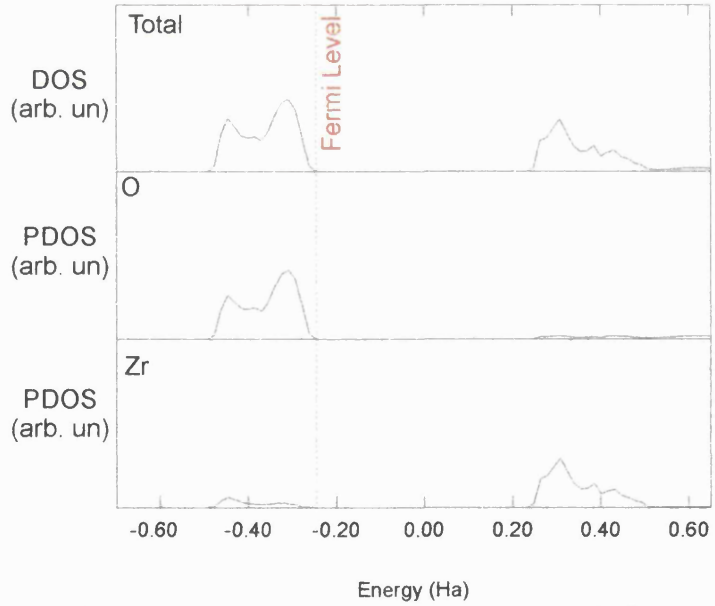

Figure 5.12: Density of States calculated for *m*-ZrO_2.

The calculated band gap obtained with each of the Hamiltonians studied in the course of this work are reported in table 5.11, where again we see the exaggeration so common with the HF Hamiltonian. In comparison to the band gaps which were obtained for the two remaining ambient pressure phases, the calculated band gaps of the monoclinic

phase are greater than those predicted for the cubic structure (using the equivalent Hamiltonian), but less than those of the tetragonal structure. Jomard *et al.* (90) calculated the monoclinic band gap energy to be 3.42 eV (GGA) and 3.51 eV (LDA) in his work, in good agreement with the results calculated here.

Table 5.11: The calculated band gap of *m*-ZrO_2, obtained with all Hamiltonians studied here.

Hamiltonian	Calculated Band Gap (eV)
HF	13.36
LDA	3.56
GGA	3.36
B3LYP	5.13
Jomard LDA (90)	3.51
Jomard GGA (90)	3.42
Králik GW (83)	5.42
Experiment (94)	5.83-7.09

5.4 Conclusions

The work reported in this chapter has demonstrated several important results regarding the ambient pressure phases of zirconia. Most importantly, throughout this work, the correct order of stability of these three phases is in line with the experimental phase diagram observed (shown previously in figure 4.2): the monoclinic phase is predicted to be the most stable of all three phases studied here, with the tetragonal being higher in energy, and the cubic even more so.

Many studies are able to correctly predict the monoclinic phase as more stable than the tetragonal, using either *ab initio* or interatomic potential methods; the subtleties of the cubic-tetragonal displacive phase transition are, however, much more difficult to replicate. To my knowledge, there are no zirconia potential sets capable of correctly reproducing the *c-t* transition, and establishing the tetragonal phase as the most stable. The precise energetics of the *c-t* transition are in good agreement to those observed experimentally (91) or in the many theoretical studies reported in table 5.2 (on page 104).

Furthermore, the quality of the oxygen basis set appears a key component in correctly modelling the transition, calculations performed using our standard 8-51G oxygen basis set did not correctly model the phase transition – the extended 8-411dG basis set was required. We believe that, since IP schemes include polarisation effects

through the (somewhat crude) shell model, that this is one plausible reason for their failings in modelling the tetragonal structure.

The monoclinic phase appears less sensitive to the oxygen basis, suggesting that the stability of this phase is caused by some other factor, the lower coordination of the metal ion could be a significant driving force for the phase transition – as the size of the zirconium ion appears too large for the fluorite/tetragonal structures and too large for the rutile structure, using a simple 'radius-rules' approach.

The calculated band gaps of the three phases have been reported throughout the previous two chapters, and although the HF Hamiltonian greatly exaggerates the calculated band gap, our parallel DFT calculations allow close comparison to other theoretical studies. The tetragonal phase is predicted to have the largest band gap (5.60 eV with the B3LYP Hamiltonian), in comparison to the quasiparticle GW calculations performed by Králik *et al.* (6.40 eV). The monoclinic band gap (5.13 eV) is slightly larger than that of the cubic phase (4.92 eV), while Králik *et al.* calculated the reverse. Due to the experimental difficulties in examining the cubic phase, the only reported experimental value for the cubic band gap is between 4-6 eV, a range the current predictions lie within.

From these calculations, we are able to conclude that the current parameter set is capable of describing the three ambient pressure phases remarkably well, and also describe the details of electronic processes which occur during the *c-t* phase transition. A wide range of Hamiltonians have been studied, and the calculated properties and energetics of each being in line with those determined with equivalent Hamiltonians in other reported theoretical studies.

6 Surfaces of Ceria and Zirconia

By definition, a catalyst is a material which increases the overall rate of a particular chemical process by providing the system with an alternate pathway to form the required end product(s). The key to this process often involves creation of an intermediate species, which possesses a lower energy barrier to formation than the reaction process that normally occurs with no catalyst present.

It is therefore of great desire that the catalyst is able to interact both electronically and sterically with the reagents in the most efficient way possible. In practical applications involving the use of ceria and zirconia, the reagents are usually gaseous – so in order to obtain a greater insight into the mechanisms by which these materials are able to catalyse such processes, a detailed understanding of the local surface features, including the electronic properties of the surface which are likely to dominate any solid-gas chemical interactions, will be of great assistance to efforts in improving the design and efficiency of such heterogeneous catalysts.

By optimising the nature of the surface, with respect to the steric and electronic requirements for the active site in the material to function at its best, it may be possible to reduce the operating temperatures (or the time taken to reach peak performance) for catalysis – and may one day lead to cost-effective SOFC power stations, or greatly improved exhaust catalysis becoming a reality.

6.1 General Introduction to Surface Modelling

All calculations reported in the previous chapters have been periodic in three dimensions of a bulk crystal – for surface structures this is no longer the case. The methods used to model surfaces in the current series of calculations were detailed at great length earlier in this thesis, in section 2.9.

In the slab model, a supercell is generated which has one face parallel to the chosen surface, and a finite height equal to the specified slab thickness. This slab is periodic in two-dimensions, and finite in the third. We therefore generate two symmetry equivalent surfaces in this model, at the upper and lower ends of the supercell; the height of the slab is (often) measured in the number of atomic planes which are used. We must take great care to ensure that any perturbations created by the upper and lower surfaces do

not interfere in the bulk of the slab, and so the thickness of the slab is carefully chosen to ensure that both the electronic and physical properties of the surface are correctly reproduced whilst also minimising the overall cost of the calculations. To make certain that this was the case here, the convergence of any ionic relaxations, the calculated surface energy, and the electronic structure were examined as a function of slab thickness.

We have chosen to study only surfaces of the pure cubic materials; surfaces of the *t*- and *m*-ZrO_2 phases were examined in the paper by Christensen and Carter (59). Although we expect these phases to possess surfaces which are more stable thermodynamically than those of the cubic phase, they are not be considered here for several reasons:

(1) Even though the fluorite structure is not the most stable (thermodynamically), this phase is often the most desirable form of zirconia in many commercial applications. Any phase changes which occur during the normal heating and cooling cycles during operation of the device involve volume changes which can crack the ceramic itself, or result in expensive active coatings to break away. This will ultimately destroying the operation of the device. By using an artificially stabilised cubic phase over the entire range of temperatures which the device functions, we ensure that this is not the case. In such a system, any surface-gas interfaces will now be those of a (stabilised) fluorite structure, rather than tetragonal or monoclinic. The additional effects caused by compositional changes which occur in the stabilisation of the cubic phase are not examined here for reasons of cost.

(2) Ceria exists only in the fluorite structure. Examination of only cubic zirconia surfaces permits a more direct comparison of the two materials.

(3) Surface calculations are significantly more expensive than those of the bulk material due to the reduction in symmetry on moving to a two-dimensional unit cell. Surfaces of tetragonal or monoclinic systems are beyond the current computational resources available for the CRYSTAL code (at the time of writing – the rate of increase in computing power means this will no longer be the case in the future!).

This work shall only consider the two surfaces shown to be the most thermodynamically stable during the earlier study (on ceria) by Vyas *et al.* (45,46,48) and separately in the study of ceria/zirconia mixtures by Balducci *et al.* (47) using interatomic potentials. These two surfaces are the {011} and the {111}, and will be discussed in the remainder of this chapter.

One of the most important quantities used to characterise a surface is the surface energy – defined as the amount of energy (per unit area) required to cleave the bulk material along a selected crystallographic face. In this thesis, the surface energy is defined by the relationship given in equation (2.29) (detailed in section 2.9).

After cleavage of a surface from the bulk, the internal energy of the slab may be reduced quite substantially from its 'just-cleaved' (unrelaxed) value by displacement of the ions away from the positions which they occupy in the bulk lattice. This relaxation becomes possible because a number of symmetry operators present in the bulk are destroyed in the generation of the slab. In order that our calculations remained viable given the limited time and resources available, it was necessary to restrict these ionic relaxations to only those which maintain all remaining symmetry operators of the slab. This assumption, although intuitive, was validated through both interatomic potential studies, and the independent plane wave calculations by Alfredsson *et al.* (98) using the CASTEP (99) and VASP (93) codes.

6.2 Interatomic Potential Surface Calculations

To complement the current *ab initio* investigations, and also assess the applicability of interatomic potentials studies in surfaces of these materials, an additional series of IP calculations were performed on selected surfaces of these two materials. Potential Sets 1 and 2 (ceria) by Vyas *et al.* (48) listed in tables 6.1 and 6.2, and the zirconia potential set derived by Dwivedi and Cormack (100) listed in table 6.3, used in the work by Balducci *et al.*, (44) on mixed ceria and zirconia systems were employed here.

Table 6.1: CeO_2 Interatomic Potential Parameters for Potential Set 1 (48)

Interaction	A (eV/Å)	ρ (Å^{-1})	C (Å^6)	k (eV Å^{-2})	Y (e)	Cut Off (Å)
O^{2-} — O^{2-}	9547.92	0.2192	32.00	9.3	-2.04	12.0
Ce^{4+} — O^{2-}	1809.68	0.3547	20.40	177.84	-0.20	12.0

Table 6.2: CeO_2 Interatomic Potential Parameters for Potential Set 2 (48)

Interaction	A (eV/Å)	ρ (Å^{-1})	C (Å^6)	k (eV Å^{-2})	Y (e)	Cut Off (Å)
O^{2-} — O^{2-}	9547.92	0.2192	32.00	10.3	-2.04	12.0
Ce^{4+} — O^{2-}	2531.5	0.335	20.40	177.84	-0.20	12.0

Table 6.3: ZrO_2 Interatomic Potential Parameters (44,47,60,100)

Interaction	A (eV/Å)	ρ (Å^{-1})	C (Å^6)	k (eV Å^{-2})	Y (e)	Cut Off (Å)
O^{2-} — O^{2-}	22764.3	0.149	27.89	27.29	-2.077	12.0
Zr^{4+} — O^{2-}	985.869	0.376	0.0	169.617	1.35	12.0

In IP surface modelling, a slab model similar to that used in the current CRYSTAL calculations is employed. However, the IP slab is divided into two separate regions, as shown in figure 6.1: ions forming region I are explicitly relaxed to minimise the internal forces using the Buckingham equations, while ions forming region II are kept stationary at all times. Region II exists to recreate the effects of the infinite crystalline field of the lattice on the ions moving in region I.

Figure 6.1: The Interatomic Potential Slab model. This figure illustrates the distinction between Region I and Region II ions in the IP slab model.

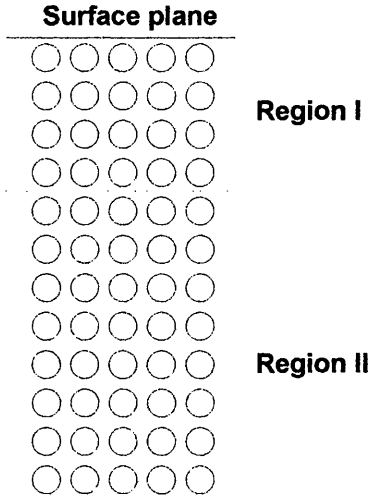

In the present study, region II ions were *not* included in the calculations. This approach was taken because the resulting slabs are analogous to the slab geometries examined in the *ab initio* calculations – the use of a region II model to include the

Coulombic effects of an infinite crystal lattice on the examined section cannot be replicated in the present *ab initio* calculations. Surface energies for infinite slabs were calculated using the full two region approach to provide data to compare to that from smaller slabs

The aim of these IP calculations is to permit a more direct comparison of the *ab initio* and the interatomic potential calculations. These IP potentials also allow the convergence of the (limited) *ab initio* calculations regarding the calculated surface properties (e.g. the surface energy, or ion relaxation) to be assessed, by permitting investigation of much larger slabs than is possible with the current QM calculations.

6.3 The {011} Surface

Even though the {011} surface is found to be thermodynamically less stable than the {111} surface, it shall be discussed first since the results obtained proved to have a more interesting and relevant consequences to the catalytic application of these two oxides.

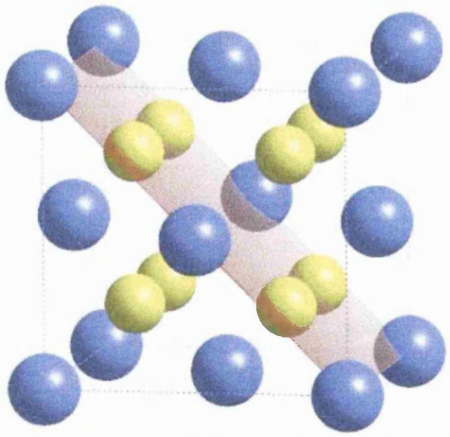

Figure 6.2: Graphic illustrating the location of the {011} surface in the fluorite structure.

The {011} plane in the fluorite unit cell is shown for reference in figure 6.2. During the construction of the *ab initio* slabs, the symmetry of the system requires that the centre of the slab be a mirror plane. In slabs containing an odd number of layers (like the five layer slab shown in figure 6.3(a)), then the central atomic layer must belong to this mirror plane, and any ions within this layer may be displaced parallel to the surface normal without destroying the slabs mirror symmetry. However, in slabs containing an even number of atomic layers (such as the six layer slab shown in figure 6.3(b)), then all

ions present may be displaced along the [001] (plane normal) direction with no loss of symmetry.

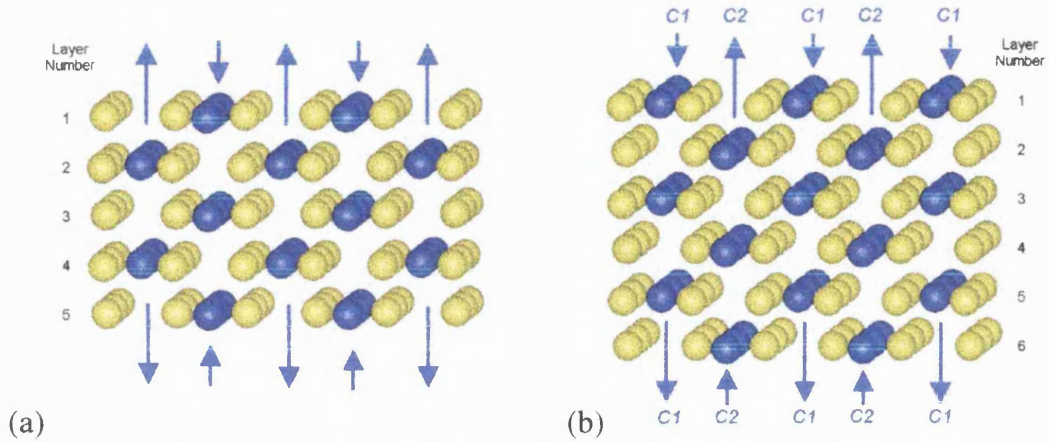

(a) (b)

Figure 6.3: A graphical overview of the {011} surface of fluorite-structured CeO_2 and *c*-ZrO_2. Surface structural relaxations were permitted in the present series of calculations, and the two possible surface geometries obtained from this construction are shown here: (a) an odd number of layers, where the central plane of atoms is a mirror plan in the slab height; (b) an even number of surface layers.

In the unrelaxed ('just-cleaved') slabs we observe little difference between the slabs having an even number, or an odd number of atomic planes. For example, table 6.4 lists the calculated Mulliken charges on the metal and oxygen ions in a five, and again in a six-layered slab. As these results are for the unrelaxed slabs, there can be no structural differences between the two, other than the obvious additional layer in the six-layered slab. We clearly see in table 6.4 that both slabs provide an almost identical electronic description of the unrelaxed surfaces throughout the entire depth of the material, and also note that ions at the centre of either slab possess an electronic configuration which we would expect (from the previous calculations examined in chapter 4) for ions forming part of the bulk material. We should also mention that even though the only data reported here is for ceria, an identical result was obtained for zirconia.

Table 6.4: A comparison of the calculated Mulliken properties of unrelaxed slabs containing an odd and an even number of layers in the CeO_2 system.

	Five Layers	Six Layers	Bulk
$Q^{surface}(Ce)$	+3.023	+3.024	—
$Q^{surface}(O)$	-1.536	-1.536	—
$Q^{centre}(Ce)$	+3.427	+3.427	+3.461
$Q^{centre}(O)$	-1.686	-1.686	-1.730

On the {011} surface, the metal ion coordination is reduced to six, and the oxygen ion coordination to three; for reference, in the bulk the metal ions are eight-fold coordinated and the oxygens four-fold. The {011} surface may be viewed as being constructed from repeated oxygen-metal-oxygen platelets, with each platelet separated from the next by a row of interstitial sites in the plane of the surface. These surface interstitials alter the environment surrounding the surface oxygen ions to one which is more representative of a surface defect or a kink site, rather than that expected of a flat surface. This may be an important property of the {011} surface, as numerous independent studies on a wide range of materials have shown that such surface defects can function as centres for surface catalysis, especially in heterogeneous systems like the SOFC or an automobile exhaust catalytic converter. In addition, these interstitial sites may play a highly important role in situations where the material is used as a ceramic support for some other active species, often a noble metal. One such example of this is in the automobile three-way exhaust catalytic converter, in which the active element is platinum (or alternatively rhodium) metal deposited onto a ceria/alumina support: these surface interstitials could assist the deposition of the metal by acting as open 'docking' sites on the surface in which the metal atoms can adsorb.

For future reference in the following discussion, I shall mention now that the metal ions in the {011} slabs appear to lie in two independent columns running through the thickness of the slab, perpendicular to the plane of the surface. The first of these columns, labelled as *C1* in figure 6.3, contains the outermost surface cations and all metal ions belonging to the odd-numbered atomic layers; the second, labelled as *C2* in figure 6.3, contains all cations in the even-numbered atomic layers, and is a symmetry inversion of *C1* around the centre of the slab. As we shall see in the following sections, the relaxation induced by creation of the surface appears to involve a large correlation in the displacement of ions in these two columns.

6.3.1 Slab Relaxation

As previously mentioned, the cubic phase of zirconia is thermodynamically unstable at low temperatures, and undergoes a phase transition to a tetragonal structure by displacement of the oxygen ions along the <001> direction. It is therefore natural to assume that since the surface is initially cleaved from a cubic lattice, ions on the surface would revert to a geometry corresponding to one of the lower symmetry phases during

surface relaxation, rather than maintaining a cubic-like symmetry. For this reason, in their recent paper on the bulk and surface structures of ZrO_2, Christensen and Carter (59) did not calculate relaxed surface configurations for cubic-ZrO_2 systems.

In order to ascertain if the *c-t* phase transition could be represented in our current calculations, we need to establish whether or not this transition can be modelled by oxygen ion displacements which do not create further loss of symmetry in the newly-cleaved slab. Figure 6.4(a) illustrates the direction ions must move to revert to a tetragonal structure, while figure 6.4(b) shows the directions permitted for ions on this surface in order to maintain symmetry. The two are clearly unequal, and thus we conclude that our relaxed {011} surface configurations do in fact refer to the cubic phase at all times, and that the ionic relaxations cannot be form the tetragonal phase in the process.

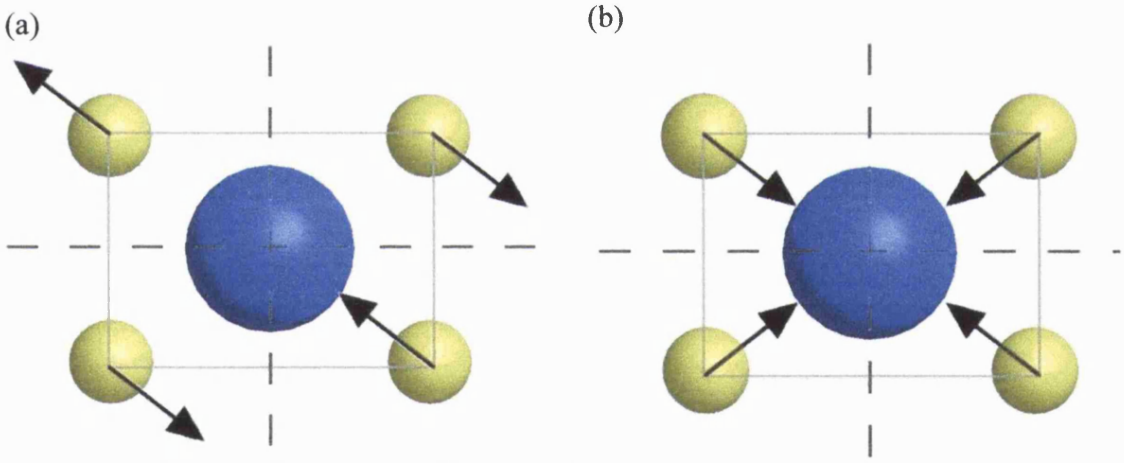

Figure 6.4: Image (a) shows the ion displacements which occur during the *c-t* phase transition in a {011} surface unit cell. Figure (b) shows the symmetry permitted oxygen ion relaxations. The two perpendicular mirror planes (dashed lines) bisect the unit cell and force all oxygens to relax either inwards or outwards to maintain symmetry. It clear from these figures that the phase transition is forbidden in the present calculations.

Confirmation of this result may be found by examining the calculated ion displacements at various depths through the slab. If a phase transition were to occur, it would involve relaxation of all oxygen ions in a similar manner, regardless of their position in the slab. The calculated displacements, listed in table 6.7, decrease in magnitude on moving from the surface to the lower surface, and are therefore not associated with the *c-t* transition. The relaxations associated with the experimentally measured phase transition by Fukuhara *et al.* (86) and also by Kisi *et al.* (92) were $0.057c_{tet} = 0.3$ Å, a figure much larger than the oxygen relaxation observed here in the

centre of the slab. The calculated oxygen displacements reported in table 5.2 (on page 104), and are somewhat smaller than this experimental value – corresponding to an oxygen ion relaxation of approximately 0.2 Å. Although this figure is similar to the relaxations predicted for the outermost surface oxygen ions, it is significantly larger than those at the slab's centre, and therefore cannot be associated with a global phase transformation.

The symmetry operators present in the {011} (and also in the {111} slabs) are therefore sufficient to prevent the occurrence of the *c-t* phase transition, and therefore the slabs studied here do in fact correspond to those of a cubic phase at all times.

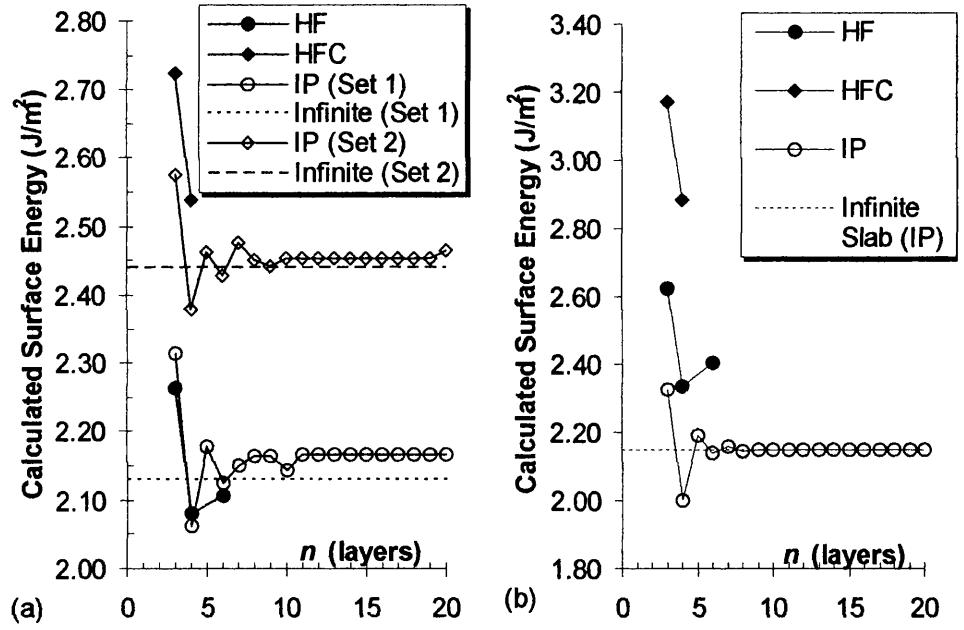

Figure 6.5: The trend in relaxed (calculated) {011} surface energies with slab thickness for (a) ceria, and (b) zirconia {011} slabs. HF are calculations performed at the Hartree-Fock level, HFC include an *a posteriori* estimate of the electron correlation energy, while interatomic-potential calculations are given for comparison.

We have performed *ab initio* calculations on {011} slabs containing three, four, and six atomic layers (*n*); and furthermore have complemented these using interatomic potential calculations on {011} slabs containing up to twenty atomic layers (using the region I only model detailed earlier in this chapter). The calculated relaxed and unrelaxed {011} surface energies of such slabs are illustrated graphically as a function of slab thickness in figure 6.5, and are also listed in table 6.5.

Table 6.5: Calculated {011} surface energies of CeO_2 and ZrO_2, for increasing slab thickness, *n* (in number of atomic layers).

		CeO_2 (J/m^2)		ZrO_2 (J/m^2)	
	n	Unrelaxed	Relaxed	Unrelaxed	Relaxed
HF	3	2.669	2.264	3.038	2.625
	4	2.648	2.082	3.033	2.335
	6	2.624	2.106	3.035	2.406
HFC	3	2.983	2.724	3.533	3.170
	4	2.970	2.538	3.524	2.886
IP Set 1	3	3.563	2.314	3.642	2.327
	4	3.559	2.062	3.636	2.001
	6	3.560	2.125	3.638	2.137
	20	3.560	2.166	3.638	2.147
	∞	3.560	2.130	3.638	2.148
IP Set 2	3	3.781	2.576		
	4	3.776	2.378		
	6	3.777	2.427		
	20	3.777	2.464		
	∞	3.780	2.440		

Concentrating on the ceria slabs for the moment, we immediately see a close correlation between the *ab initio* and interatomic potential calculations: potential set 1 closely reproduces the *ab initio* calculations performed using a pure HF Hamiltonian, while potential set 2 reproduces the calculations including the Perdew-91 (101,102) estimate of correlation *a posteriori* on the Hartree-Fock density during the numerical optimisation.

It should be noted that the agreement between the two sets of calculations is quantitative, as well as qualitative; both interatomic potential and *ab initio* calculations provide an {011} surface energy of approximately 2.1 – 2.4 J/m^2; I am unaware of any published experimental studies reporting surface energies of ceria with which to compare, however the IP ceria study by Sayle, *et al.* (103) and the investigations by Conesa (104) provide {011} surface configurations and energetics which are in good agreement with those calculated here.

The IP surface study by Balducci (47) predicted an {011} surface energy of 2.40 J/m^2 for ceria, and approximately 2.10 J/m^2 for zirconia, figures in excellent agreement to the current range predicted. They also observed a similar reduction in the surface energy on relaxation of the surface ions, with their reported unrelaxed surface energies ranging from 3.5 J/m^2 (CeO_2) to 3.6 J/m^2 (ZrO_2). A significant discrepancy is

often tolerated in reported values of surface energies, due primarily to the intrinsic experimental difficulties which need to be overcome in order to quantify such a highly subjective surface property, a variation of 0.3 J/m^2 between the results reported here is of little importance, and can be easily disregarded.

The agreement of interatomic potential studies to the current *ab initio* results is highly encouraging, given the prohibitive nature of quantum mechanical calculations, although is not entirely unexpected. Our previous studies on the bulk phases (see chapters 4 and 5 for further details) have shown these materials to have a highly ionic nature: Ce having a calculated charge of +3.46, Zr of +2.99, in comparison to the formal charge of +IV. Interatomic potential studies are well known to accurately model both bulk and surface systems in which the interactions are highly characterised as either highly ionic, or largely covalent, rather than an intermediate state.

We observe from figure 6.5 and table 6.5, that inclusion of electron correlation into the internal energy minimisation causes the calculated surface energy to increase. It is important to remember that surface energies calculated at the HF-only level of theory are fully consistent with the Hamiltonian used, something which is not the case for the HFC energies in which the electronic distribution at the surface cannot adapt to correlation effects being included. The two-step approach used in the HFC studies has been applied in several investigations on bulk materials (18,19,105,106), and generally improves the quality of the calculated properties, especially for the heat of formation of the solid. However, there is little experience on the validity of such an approach to studies of surface in the manner we have used here. As a consequence, we expect the HFC calculations to underestimate the electronic relaxation introduced by formation of the surface from the bulk crystal, and therefore to overestimate the predicted surface energies. If the effects of correlation were to be included self-consistently in the Hamiltonian, as was the case in the LDA calculations by Christensen and Carter (59) then we expect the calculated HFC surface energy to decrease.

Although Christensen and Carter did not calculate the relaxed geometries of cubic-zirconia slabs, they did report relaxations observed in the tetragonal and monoclinic surfaces studied. In general, they observed (averaged) relaxations of 0.1-0.3 Å on all their examined surfaces; the observed relaxations in the current work (~0.2 Å) are of a similar magnitude, suggesting the two studies are in qualitative

agreement with one another. Christensen and Carter calculated the unrelaxed surface energy of the cubic {011} surface as 2.29 J/m^2. When the effects of electron correlation were included *a posteriori* into the current HF surface calculations, then the predicted {011} surface energy increased by approximately 0.50 J/m^2, although the energy change introduced by relaxation of the ions remained unchanged at 20% of the unrelaxed energy.

On comparing ceria and zirconia, we find that (in the *ab initio* calculations) the calculated surface energy of ceria is approximately 10% smaller than that of zirconia, using both the HF and the HFC Hamiltonians. Zirconia has slightly more covalent bonding than ceria – due no doubt to the smaller ionic radius of the Zr(IV) cations increasing the degree of interaction to neighbouring anions which results in zirconia possessing a higher lattice energy than ceria. Clearly, more energy will be required to cleave a Zr–O bond than is needed to cleave a Ce–O bond, and so we expect zirconia to have a higher surface energy than ceria, although this effect may be masked by the reduction in surface energy caused by ion relaxations.

This trend is not observed in the (unrelaxed) interatomic potential calculations, which instead predict that the surface energies of both materials should be at best identical (using CeO_2 potential set 1), or even lower in zirconia (using CeO_2 potential set 2). This is believed to be because such calculations are only able to take into account the electrostatic potential between two ions, and not the subtleties permitted by *ab initio* calculations.

Table 6.6: Calculated relaxation (in Å) of the outermost cerium ions at the {011} ceria surface. The ions have been separated into columns C1 and C2, as labelled in figure 6.3(b).* The sign of these relaxations is such that a positive displacement is towards the upper surface of the slab, and a negative towards the lower.

		6 layers						20 layers			
	Atomic Layer	HF		IP Set 1		IP Set 2		IP Set 1		IP Set 2	
		C1	C2	C1	C2	C1	C2	C1	C2	C1	C2
Top half of slab	1		-0.17		-0.23		-0.21		-0.21		-0.20
	2	+0.09		+0.17		+0.13		+0.16		+0.14	
	3		-0.04		-0.07		-0.04		-0.03		-0.02
	4	—		—		—		+0.03		+0.02	
Bottom half of slab	4	—		—		—			-0.02		-0.02
	3	+0.04		+0.07		+0.04		+0.03		+0.02	
	2		-0.09		-0.17		-0.13		-0.15		-0.14
	1	+0.17		+0.23		+0.21		+0.21		+0.20	

We shall now examine the convergence of the calculated surface energies on increasing the slab thickness. In figure 6.5 we observe that the surface energy oscillates as a function of slab thickness; in particular slabs having an odd number of atomic layers have larger surface energies than slabs containing an even number of layers. We can explain this result by a closer examination of the physical nature of the ionic relaxations which occur in each slab.

Table 6.7: Calculated relaxations (in Å) of the Zr ions at the {011} surface. The sign of the ionic displacements is the same as in table 6.6.

		Number of layers in slab					
		6 layers				20 layers	
		HF		IP		IP	
	Atomic Layer	C1	C2	C1	C2	C1	C2
Top half of slab	1		-0.21		-0.18		-0.18
	2	+0.10		+0.14		+0.13	
	3		-0.07		-0.06		-0.03
	4	—		—		+0.02	
Bottom half of slab	4	—		—			-0.02
	3	+0.07		+0.06		+0.03	
	2		-0.10		-0.14		-0.13
	1	+0.21		+0.18		+0.18	

* Note that in the six layer slab, atomic layer number four is a symmetry reflection of atomic layer number three.

The calculated magnitudes of the cation relaxations are reported in tables 6.6 (CeO_2) and 6.7 (ZrO_2), in the remainder of this discussion we denote those relaxations directed away from the centre of the slab as positive, and those relaxations directed towards the slab centre as negative. In tables 6.6 and 6.7, for clarity, the ions have been separated into the two distinct columns labelled as *C1* and *C2* in figure 6.3.

Although only cation displacements along the direction perpendicular to the surface were permitted (by symmetry), the oxygen ions could also relax horizontally in the way illustrated in figure 6.4(b). During the relaxation of the bulk-terminated surface, the anionic movements can be described as a "rolling" of the oxygen around the metal ions, maintaining a roughly constant metal-oxygen separation near the surface. This was further verified through the use of plane wave calculations by Alfredsson (98), and by interatomic potential calculations, in which all ions in the slab were allowed to relax fully.

The vertical cation relaxation appears to have a strong correlation in each of the columns *C1* and *C2*. The metal ions in column *C1* (of a slab with an even number of layers) displace away form the upper surface and towards the lower surface, while ions belonging to *C2* do the reverse. In slabs with an odd number of layers, this effect is destroyed since the central layer may not be displaced along the plane normal, and instead the ions relax either away from the central layer (if the half-column is surface-terminated) or towards it (if the column terminates on the subsurface layer). This effect is indicated by the arrows on figure 6.3(a) and (b).

The extra stabilisation caused by the columnar relaxation explains why the surface energy calculated with slabs having an even number of atomic layers is always lower than that for slabs with an odd number of layers. When we examine the unrelaxed surface energies for the same slabs (given in table 6.5) we see a much smoother behaviour as the thickness of the slab is increased – confirming that the oscillation in relaxed surface energy relates entirely to the ionic relaxation.

Concentrating now on the cation relaxations in CeO_2 (table 6.6), we note that in the six layer {011} slab, the relaxations predicted by interatomic potentials in each atomic layer are remarkably similar to those determined in the *ab initio* study. The displacement of the outermost atomic layers obtained using twenty-layer IP slabs are

also shown for comparison; it can be clearly seen that even though the magnitude of the relaxations does decrease (by approximately 0.01-0.02 Å), such a reduction appears negligible. There will therefore be only a small gain in the accuracy of the predicted relaxations by using *ab initio* slabs thicker than six atomic layers.

The calculated values for zirconia (listed in table 6.7) show a similar pattern. The potential set used to describe ZrO_2 provides a less satisfactory quantitative agreement with the *ab initio* results for the surface energy; however, appears to work well when describing the ionic relaxation at the surface.

During the course of this work, the computing power available meant that *ab initio* calculations could be performed on slabs possessing up to six atomic {011} layers (which corresponds to an irreducible unit cell containing 18 atoms). Given the good correspondence of results between *ab initio* and interatomic potential calculations, we have extended the study to slabs of up to twenty atomic layers. When the thickness of the slab becomes large enough for ions in the centre to be unaffected by the surface, both halves of the slab can fully relax without influencing each other. We see in figure 6.5 that at this point, the calculated surface energy becomes invariant of slab thickness. Comparing this trend in calculated surface energies, we estimate that eight {011} atomic layers would be the minimum slab thickness required to fully converge the calculated surface energy; the atomic relaxations calculated with the six layer slabs are however already very similar to the twenty layer slabs, such that even a six layer {011} slab represents (with sufficient accuracy) the equilibrium energy minimised surface structure and energetics.

Table 6.8: Mulliken charges as a function of slab thickness (*n*, in atomic layers) for the {011} surfaces of ceria and zirconia. Results relating to the bulk structures are also reported for comparison. 'Depth' refers to the position of the atomic layer within the slab ('1' is the uppermost surface, '3' is three atomic layers below layer '1'). Q(M) and Q(O) are the net charges of the metal (M) and O ions in the specified layer, while Q_b(MO) and Q_b(OO) are the bond populations (in |e|) for the MO and OO interactions.

			Depth			
	n		*1*	*2*	*3*	*Bulk*
CeO_2	3	*Q(Ce)*	+3.046	+3.405	–	+3.461
		Q_b*(CeO)*	+0.006	-0.072	–	-0.043
		Q(O)	-1.541	-1.667	–	-1.730
		Q_b*(OO)*	-0.076	-0.028	–	-0.030
	4	*Q(Ce)*	+3.042	+3.395	–	–
		Q_b*(CeO)*	-0.004	-0.050	–	–
		Q(O)	-1.538	-1.680	–	–
		Q_b*(OO)*	-0.072	-0.030	–	–
	6	*Q(Ce)*	+3.045	+3.410	+3.448	–
		Q_b*(CeO)*	-0.002	-0.007	-0.039	–
		Q(O)	-1.542	-1.693	-1.717	–
		Q_b*(OO)*	-0.073	-0.039	-0.031	–
ZrO_2	3	*Q(Zr)*	+2.773	+2.948	–	+2.992
		Q_b*(ZrO)*	+0.053	-0.018	–	+0.012
		Q(O)	-1.379	-1.490	–	-1.496
		Q_b*(OO)*	-0.104	-0.065	–	-0.070
	4	*Q(Zr)*	+2.755	+2.925	–	–
		Q_b*(ZrO)*	+0.042	+0.002	–	–
		Q(O)	-1.362	-1.478	–	–
		Q_b*(OO)*	-0.103	-0.068	–	–
	6	*Q(Zr)*	+2.762	+2.945	+2.982	–
		Q_b*(ZrO)*	+0.045	-0.002	+0.016	–
		Q(O)	-1.367	-1.487	-1.490	–
		Q_b*(OO)*	-0.101	-0.069	-0.071	–

A Mulliken population analysis on the electronic distribution for ions at the surface and in the centre of the slab (the results of which are given in table 6.8) shows that surface ions are more polarised and have a lower ionic charge than their equivalent ions in the bulk, as we would intuitively expect. The Mulliken charges appear to have converged for slabs with more than four atomic layers; the difference between the Mulliken population of ions in the central layer of the six layer slab and that calculated for the bulk material is just 0.010 |e| in zirconia, or 0.013 |e| in ceria – sample calculations on an eight layer slab (which did not include a complete relaxation of the ions in the slab) demonstrated that there was little change in the Mulliken populations

from the six layer slab, although the cost of calculations on these slabs were extremely prohibitive at the time.

Electron density maps calculated through the fully relaxed {011} slabs are shown in figures 6.6 and 6.8 for a variety of cross-sections slicing through the upper half of a fully-relaxed six layer slab: the plane of figure 6.6 shows the electron density within the metal ion column *C1*, while figure 6.8. shows the plane which intersects one of the oxygen-metal-oxygen platelets on the outermost surface layer.

The plane of figure 6.6 highlights the different behaviour of the two columns (*C1* and *C2*) described earlier in this chapter. This plane contains only the cations belonging to odd-numbered atomic layers, i.e. column *C1*; ions in the even numbered layers (*C2*) lie above and below this plane, although their locations relative to the plane of figure 6.6 are shown for reference. It is clear from these figures that all cations are polarised away from the lower surface towards the upper surface, which is where the column terminates. We also note that the effectiveness of the polarisation decreases on moving through the slab away from the surface-terminated cation. The plane intersecting cations in the even-numbered atomic layers, i.e. column *C2* was the exact inverse of figure 6.6: here, all metal ions electronically polarise towards the lower surface (note that in column *C2* the surface-terminating cation now lies on the lower surface).

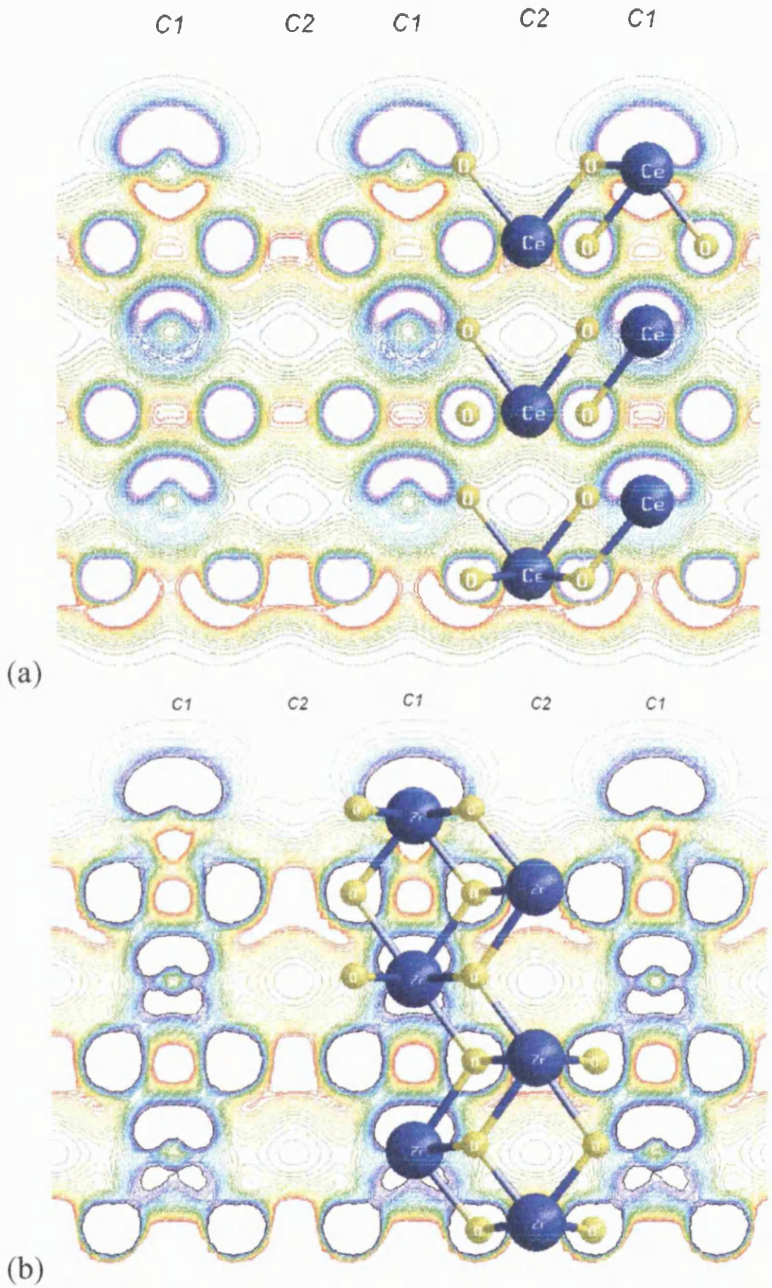

Figure 6.6: Electron density plot for six-layer {011} (a) ceria and (b) zirconia, intersecting the metal ion columns labelled as *C1* in figure 6.3. These images show the density obtained when the initial (atomic) electron density is subtracted from the total calculated. The contours range from -0.005 |e| to 0.005 |e|, with 30 contours spanning this range linearly. The colourings are such that negative values are 'cooler' dark blue and purple; positive values are 'warmer' red and orange. Yellow and green contours are close to zero

The electronic perturbations therefore appear to be transmitted from the surface to the subsurface layers differently in each of the two previously identified cation columns, in the same way as the ion relaxations discussed earlier in this section. Figure 6.6 therefore suggests an electronic explanation for the observed columnar relaxation effect in these materials – electrons on ions in the column are polarised towards the surface-terminated cation and the effect continues through the entire column. As the outermost

ion in the column relaxes away from the centre, the remainder of the column move with it, the macroscopic effect being that the columns *C1* and *C2* relax in opposite directions.

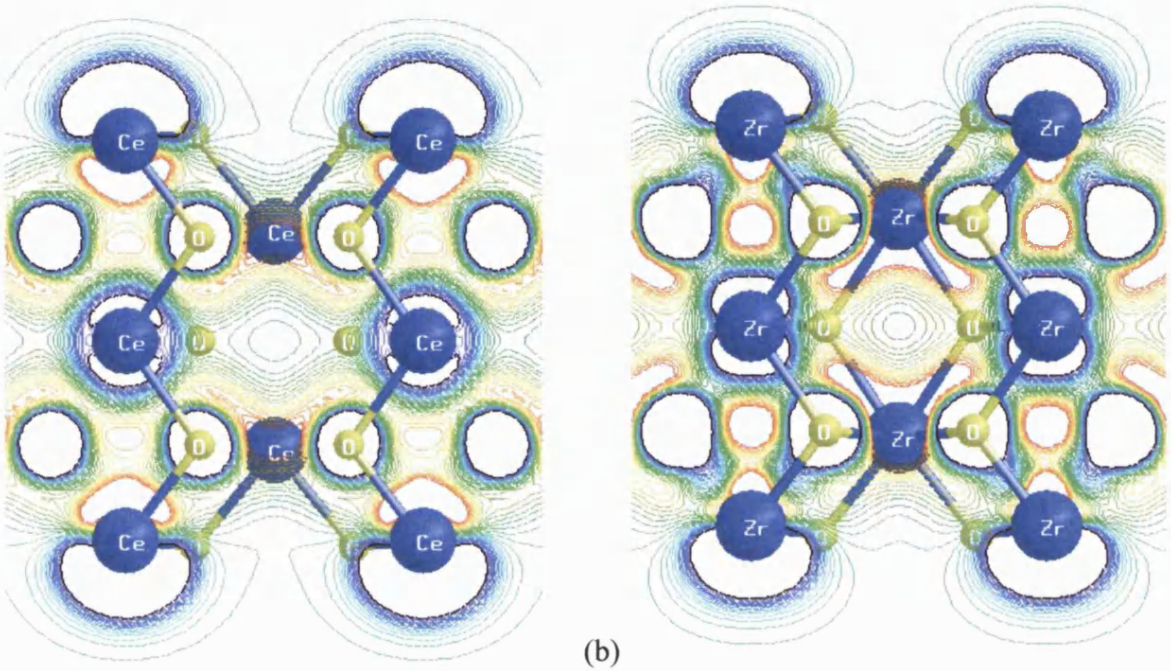

(a) (b)

Figure 6.7: Electron density plot for five -layer {011} (a) ceria and (b) zirconia, intersecting the metal ion columns (labelled as *C1* and *C2* throughout this thesis).

Figure 6.7 shows the same plane as figure 6.6 but for a slab containing only five-atomic layers through the *C1* metal ion column. By comparison to the six layer slab, the differences are clear: rather than the electron density moving in the same direction across the entire column (in the even layered slab), the requirement that the central plane be a mirror plane instead forces each half of the column to distort in opposite directions – each end of the column terminates on the outermost surface layer. As result of this is that the electron density is unable to fully relax, being constrained by the additional mirror symmetry on the central plane and therefore the calculated internal energy of such slabs is greater than those obtained for the even layers slabs (in which both the ion position and the electron density are able to fully relax). This effect is the cause of the oscillations observed in the calculated surface energies shown in figure 6.5: slabs with an odd number of layers possess a larger surface energy than those with an even number of layers.

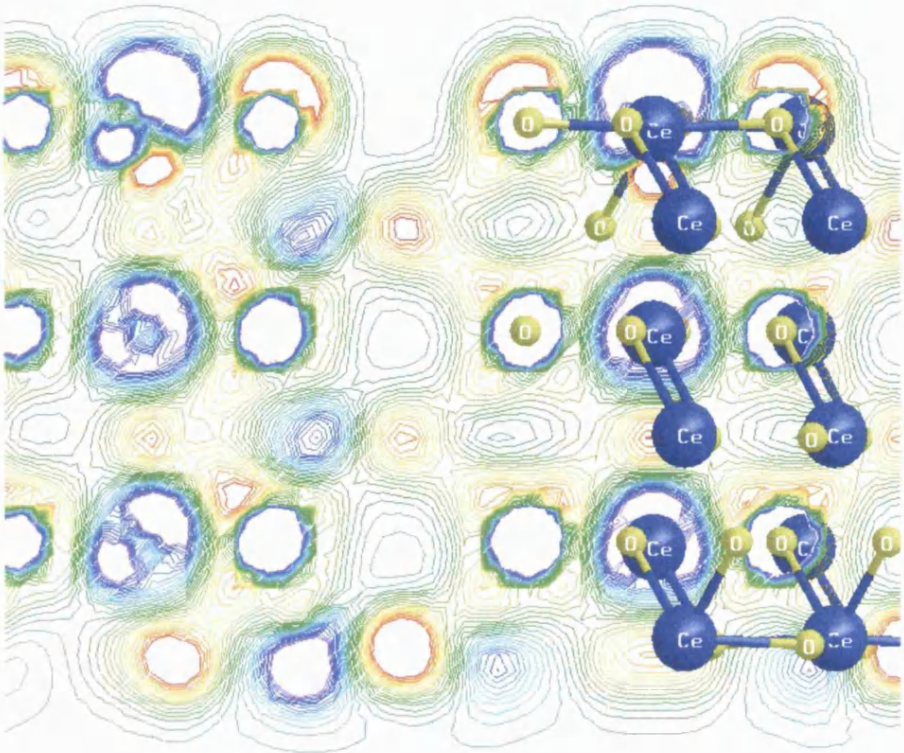

(a)

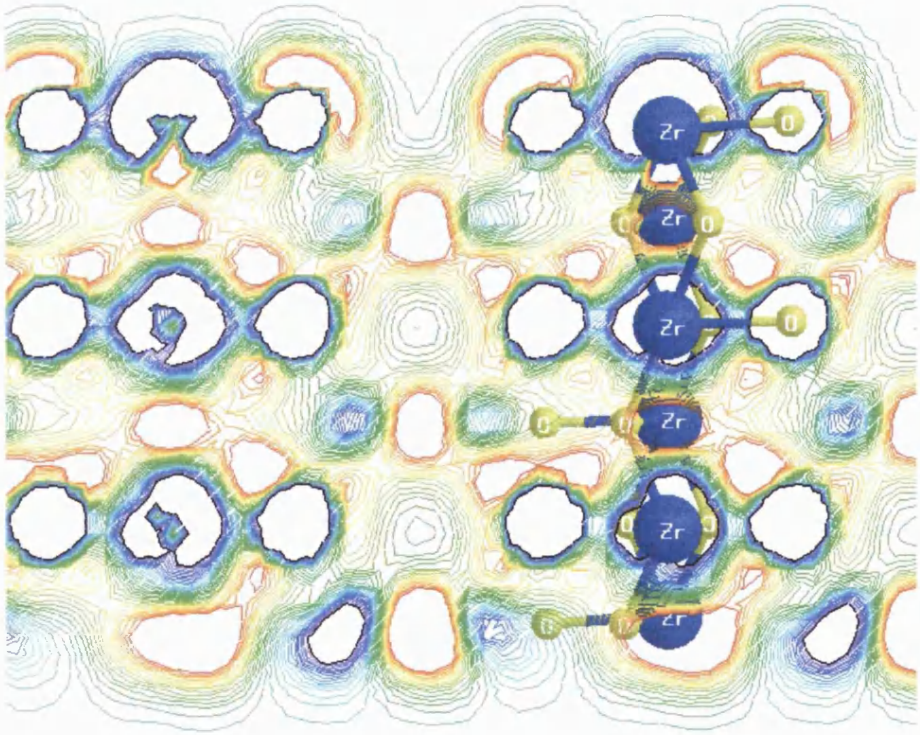

(b)

Figure 6.8: Electron density plots produced from the optimised Hartree-Fock calculations performed on 6-layer slabs of (a) ceria and (b) zirconia. The chosen cross-section intersects one of the surface metal-oxygen platelets described in the text, and also contains the slab surface normal along the vertical axis.

In figure 6.6, we observe that cerium ions have a lower *d*-orbital population than zirconium ions on the surface, since the contours on the zirconium ions appear to have a more pronounced *d*-component than they do on cerium; the same trend observed in the bulk materials is therefore preserved at the surface. In table 6.8 we see that in both ceria and zirconia, cations on the surface have a larger electron population (and therefore a lower positive charge) than those in the subsurface layers or in bulk: in ceria, the surface Ce ions contain approximately 0.4 more electrons than those in the centre of the six-layer slab, in zirconia the difference is smaller at 0.22 |e|, but is still an extremely large amount. These electrons are concentrated almost exclusively into the metal ions *d*-orbitals, the smaller charge transfer in zirconia may therefore be a result of the already significant population of these functions on ions in the bulk material and the increased electrostatic repulsion these would produce. The appearance of large areas of positive electron density (coloured red) in the ZrO_2 electron density plots in the regions between ions compared to those of ceria again demonstrates the higher covalence of zirconia

This observation confirms an increased covalence in the metal-oxygen bonding at the surface, where the Madelung (Coulomb) field is less favourable to formally charged Ce^{4+}/Zr^{4+} and O^{2-} ions. The increased electron population of the surface ions is oriented perpendicularly to the surface; the latter effect is clear in both figures 6.6 and 6.8, but even more so in the latter. Figure 6.8 shows the electron density in a plane passing through the outermost oxygen ions on the zirconia slab. As for surface Zr ions, the surface oxygen ions are distorted; the electron distribution of the outermost oxygens in figure 6.8 shows highly pronounced deviations from spherical symmetry, much greater than those seen on the subsurface oxygen ions.

Comparing the convergence properties of the surface energy and ionic relaxations examined earlier in the discussion, we conclude therefore that the latter converges more rapidly on increasing the slab thickness; further oscillations in the calculated surface energies are due to a longer-ranged electronic perturbation, which appears to be more "sensitive" to the surface than the ionic relaxations. Overall, a slab with not less than six {011} atomic layers should be employed for calculations to model the {011} surface of ceria and zirconia with sufficient accuracy. The interatomic potentials employed in the present study reproduce the QM results concerning the surface relaxation and the change in surface energy as the slab thickness is increased. However, they may be less

accurate in predicting the absolute value of the surface energy; in particular the comparison between the two materials does not reproduce the QM results.

6.4 The {111} Surface

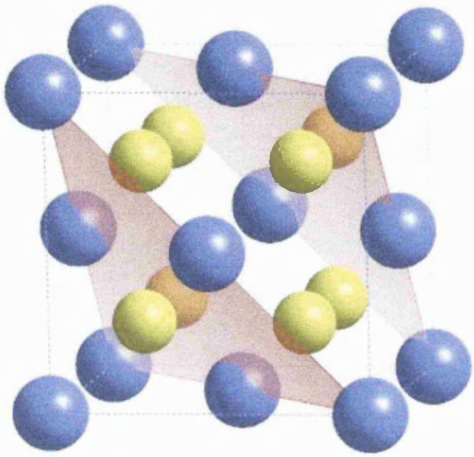

Figure 6.9: Graphic illustrating the location of the {111} surface in the fluorite structure.

The position of the {111} planes in the fluorite structure are illustrated in figure 6.9, with a sample cross-section through a {111} slab being given in figure 6.10. It can be viewed as a stepped {011} surface, in which the oxygen-metal ion-oxygen platelets partially overlap those in the layer below. Such a construction generates a rumpled surface, with highly exposed terminal oxygen ions. At the surface of the slab, the outermost oxygen ion is coordinated by three neighbouring metal ions; the outermost metal ion is instead surrounded by seven oxygen ions. It is interesting to note that this is the same coordination number as is found in monoclinic zirconia, the thermodynamically stable polymorph of the material of ZrO_2. The {111} surface was found to be the most stable surface in both experimental and in previous theoretical (IP based) studies. Since the oxygen and metal ions belong to different {111} atomic planes, each MO_2 formula unit is split into three atomic layers along the {111} direction. A {111} slab containing the same quantity of material as the six layer {011} slab would therefore require eighteen {111} atomic layers.

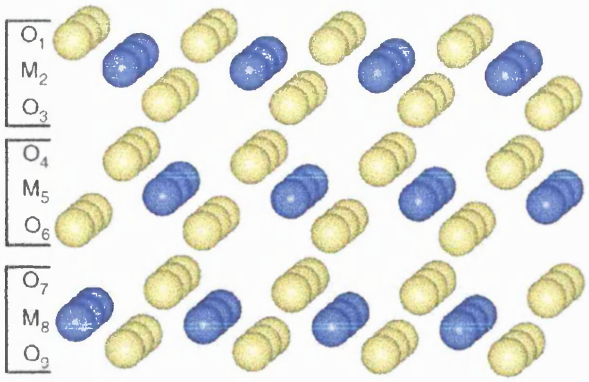

Figure 6.10: A graphical overview of the {111} surface obtained from cleaving a sample of CeO_2 and *c*-ZrO_2.

The STM (Scanning Tunnelling Microscopy) study by Nörenberg and Briggs (72,73) is one of the only known experimental attempts to directly image the surface structure of ceria, in this case the {111} surface was examined. They found that the surface was well-ordered, and terminated by oxygens in the manner shown in figure 6.10, as we would expect since this construction avoids the formation of a polar surface.

6.4.1 Slab Relaxation

During relaxation of the surface ions (which, as for the {011} surface, was restricted to retain all the symmetry operators present in the slab) only the outermost oxygen ion underwent any noticeable displacement, and even in this case by only ~0.05 Å, much smaller than the 0.21 Å relaxations of the outermost {011} surface ions. A summary of the calculated relaxations for the outermost three atomic layers in the {111} slabs is reported in table 6.9, comparing the HF and IP calculations.

Table 6.9: Relaxations of the outermost three layers in the eighteen layer {111} slab of ceria and zirconia. As for the {011}, positive relaxations are directed away from the slab centre; negative relaxations are towards the slab centre.

	n	HF	IP Set 1	IP Set 2
CeO_2	1 (O)	-0.045	-0.090	-0.086
	2 (Ce)	-0.009	-0.029	-0.025
	3 (O)	-0.024	-0.005	-0.005
ZrO_2	1 (O)	-0.044	-0.058	–
	2 (Zr)	-0.004	-0.001	–
	3 (O)	-0.029	+0.013	–

One additional consequence of the almost negligible ionic displacements of the {111} surface will be that the calculated properties of the relaxed and unrelaxed slabs will be virtually identical: the predicted {111} surface energy for a range of slab

thicknesses are summarised in table 6.10. The reduction in the calculated surface energy due to the ionic relaxations is only 0.032 J/m^2 in the 18-layer slabs (HF/CeO_2), an almost negligible amount. A second consequence is that the calculations are much faster to converge than the {011} slabs, both in the geometric optimisation of the ions and also in the SCF procedure: a much greater proportion of the {111} slab resembles the electronic configuration of the bulk material and has a higher ionicity in comparison to the {011} slabs. The calculations begin from a description of the system containing formally charged ions, which is a closer description to the electronic structure of the {111} slab than the {011}.

To confirm that the rapid convergence is not a result of our (necessary) restriction in the form of the ionic relaxations, sample calculations were repeated in the CASTEP program on similar slabs but without this relaxation restriction by both myself, and by Alfredsson (98,107); in addition, Alfredsson also performed the same calculations using the VASP program (93). The results of these calculations were in agreement to the unrestricted IP calculations performed here: the ions in the {111} slabs relax along the direction of the surface normal, there was no relaxation in the plane of the surface, which validates the use of our restricted relaxation in the work discussed here.

The LDA plane wave study of zirconia surfaces by Christensen and Carter (59) did not provide relaxed surface geometries for the cubic phase, however as we have just demonstrated that the relaxation effects in the {111} surface are almost negligible, then their calculated (unrelaxed) {111} surface energy of 1.12 J/m^2 is a close indication of what the relaxed energy would be. This value is in very good agreement to the figure of 1.49 J/m^2 calculated here.

Of somewhat greater importance is the difference in energies between the {111} and the {011} surface energies: the experimental observation is that the {111} surface is the thermodynamically stable structure, a result echoed in the current study where the {111} surface has a surface energy approximately 1 J/m^2 smaller than the {011}. This result was also found by Christensen and Carter, although without precise values of the relaxed surface energies of the cubic phase we can only estimate the energy difference that would be calculated between the two relaxed slabs to be of similar magnitude as that observed here. In their calculations of the tetragonal phase, the *t*-ZrO_2 {011} surface energy (1.53 J/m^2) is 0.3 J/m^2 greater than that of the relaxed *t*-ZrO_2 {111}

surface. We also note here that the results provided by Christensen and Carter tend to indicate that the surfaces of the cubic phase would have lower surface energies than the equivalents in the tetragonal phase: in particular, the **relaxed** energy of the tetragonal {111} surface (1.53 J/m^2) is still somewhat larger than the quoted **unrelaxed** energy of the cubic {111} surface (1.19 J/m^2) – clearly the cubic {111} surface is significantly more stable than the tetragonal {111} surface. We would expect this same trend to be seen in the current CRYSTAL calculations of the cubic and tetragonal phases, although time did not permit such a study to be performed.

As was the case with the {011} surfaces, the ceria surface energy calculated with IP Set 1 is very similar to those obtained with a pure HF Hamiltonian. The surface energy predicted by IP Set 2 is approximately 0.2 J/m^2 larger than the HF values, the same trend as observed on the {011} surface is preserved here. IP Set 2 was optimised by Vyas *et al.* for the study of high index surfaces which IP Set 1 was unable to do so. In his work, Vyas noted that on such surfaces the mass less shells surrounding the surface oxygen ions on these slabs completely separated away from the core of the anion: IP Set 2 therefore contains a larger core-shell spring constant than IP Set 1 in order to limit this unfeasible polarisation effect and encourage the anion core and shell to remain linked at all times.

Table 6.10: Relaxed and unrelaxed surface energies calculated for the {111} slabs

		CeO_2 (J/m^2)		ZrO_2 (J/m^2)	
		Unrelaxed	Relaxed	Unrelaxed	Relaxed
HF	9	1.340	1.313	1.513	1.488
	12	1.277	1.293	1.514	1.487
	18	1.277	1.245	1.514	1.485
IP Set 1	9	1.638	1.364	1.448	1.210
	12	1.638	1.365	1.448	1.220
	18	1.638	1.367	1.448	1.226
	∞	1.630	1.350	1.448	1.226
IP Set 2	9	1.820	1.555	–	–
	12	1.820	1.556	–	–
	18	1.820	1.558	–	–
	∞	1.820	1.550	–	–

A Mulliken population analysis on the electronic distribution for ions at the surface and in the centre of the slab (the results of which are given in table 6.11) shows that surface ions are more polarised and have a lower ionic charge than their equivalent ions

in the bulk, as we observed for the {011} surface. Ionic charges are largely unaffected by increasing the slab thickness beyond four atomic layers; at this point, the electronic distribution of the ions in the centre of the slab approximated the bulk materials reasonably well. We conclude therefore that the electron density, as well as the ionic relaxations, converges rapidly as a function of slab thickness, which is of course important if a slab model is to be used to represent the chemical (i.e. catalytic) activity of the surface examined.

Table 6.11: Mulliken charges and bond populations for ions in an eighteen layer {111} slab. The columns refer to a particular O_a-M_b-O_c platelet, as illustrated in figure 6.10.

	O_a-M_b-O_c platelet		
	O_1-M_2-O_3	O_4-M_5-O_6	O_7-M_8-O_9
$Q(O_a)$	-1.565	-1.703	-1.727
$Q_b(O_aCe_b)$	+0.012	-0.046	-0.041
$Q(Ce_b)$	+3.247	+3.456	+3.457
$Q_b(Ce_b\text{-}O_c)$	-0.045	-0.042	-0.042
$Q(O_c)$	-1.705	-1.731	-1.729
$Q(O_a)$	-1.404	-1.492	-1.497
$Q_b(O_aZr_b)$	+0.062	+0.010	+0.014
$Q(Zr_b)$	+2.909	+2.989	+2.991
$Q_b(Zr_b\text{-}O_c)$	-0.004	+0.013	+0.013
$Q(O_c)$	-1.504	-1.497	-1.496

Table 6.11 shows the results from a Mulliken analysis performed on the equilibrium HF electron density. These values illustrate that even for the thinnest slab used (containing only 9 {111} atomic layers, the equivalent number of ions as are contained in a 3 layer {011} slab) the ions at the centre of the slab already closely resemble those of the bulk material, and increasing the slab thickness does not alter the charge attributed to any of the ions in the slabs; we can therefore consider a 9 layer {111} slab as being fully converged.

(a)

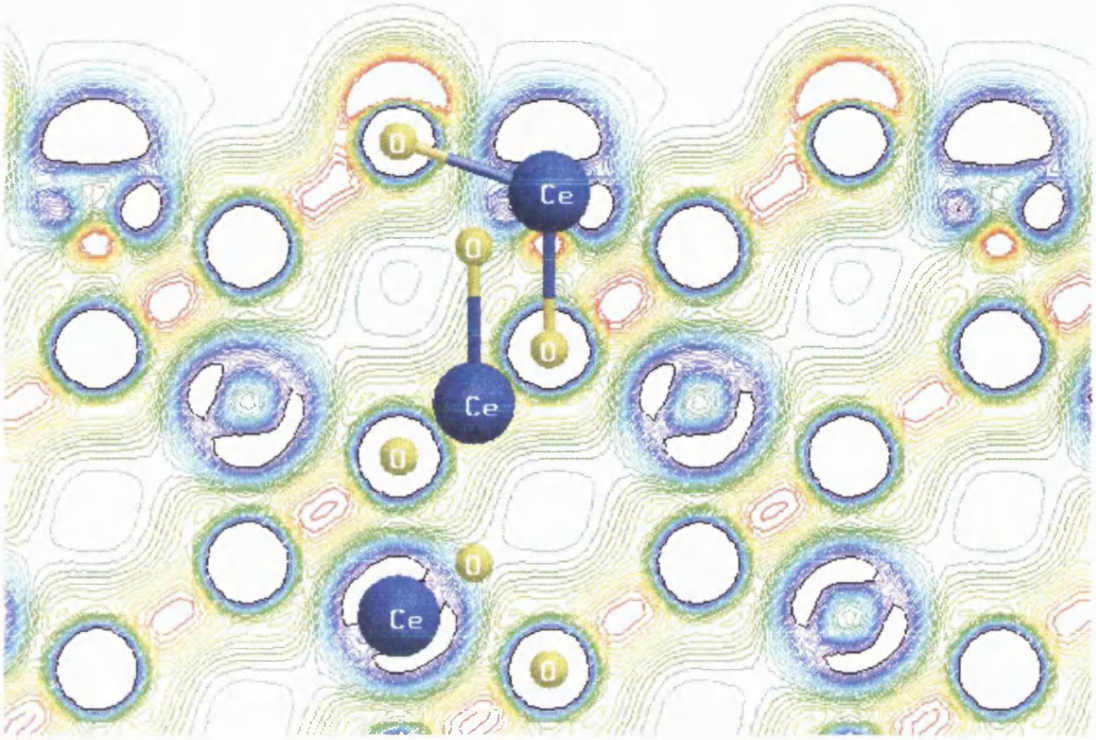

(b)

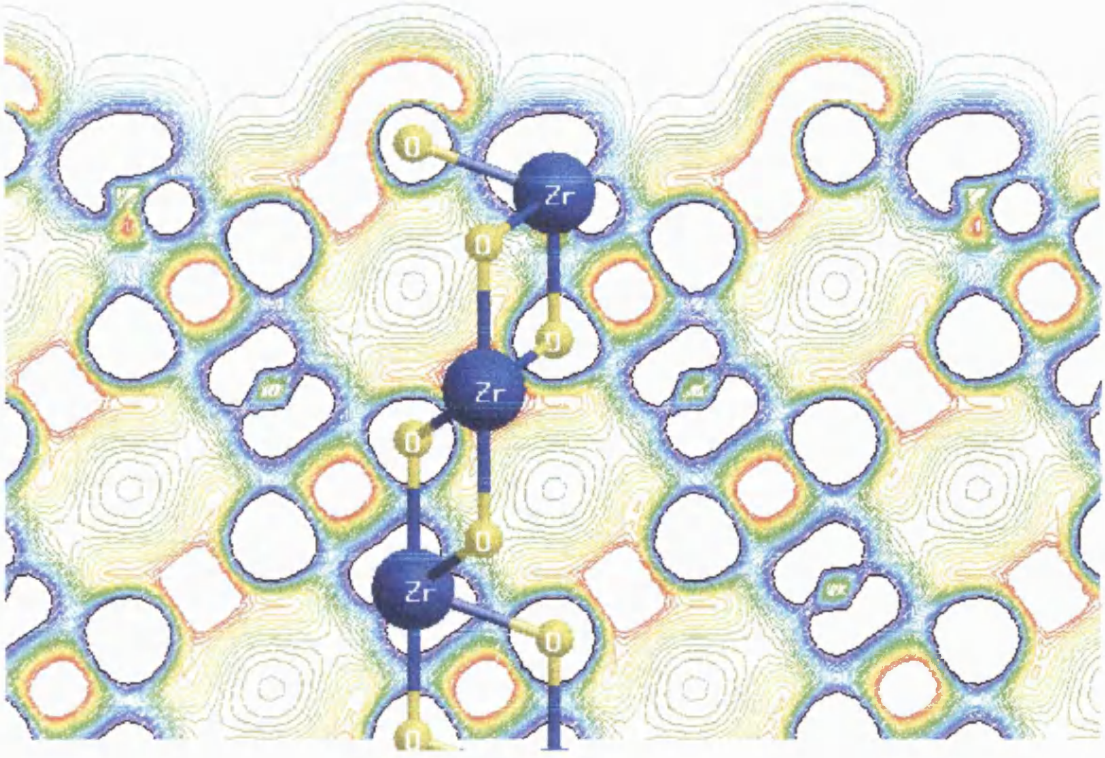

Figure 6.11: Electron density plot for 18-layer {111} of (a) ceria and (b) zirconia.

Results of the QM calculations confirm that the {111} surface is energetically stable compared to the {011} surface in both CeO_2 and ZrO_2, with the difference in surface energy between the two being approximately 1 J/m^2 in both cases. The experimentally observed order of stability of these two surfaces is correctly replicated, and the surface energies of each are in good agreement to calculations using interatomic potentials.

7 Conclusions

The work reported here has provided several key results which may be of great interest to future similar studies:

- Ceria is a highly ionic material, and while zirconia demonstrated a greater degree of covalence that ceria, it remains a largely ionic material.

- The order of stability of the ambient pressure zirconia phases was correctly predicted. The monoclinic phase is the most stable (approximately 2 mHa = 0.054 eV lower in energy than the cubic, at the HF level), followed by the tetragonal (0.58 mHa = 0.016 eV lower in energy than the cubic, again at the HF level). Such energy differences are typical of temperature-driven phase transitions such as these.

- The energy double well observed in all previous theoretical studies of the *c-t* zirconia phase transition is observed.

- Oxygen polarisability appears to be a key feature of the *c-t* phase transition – studies which are incapable of providing an adequate representation of the oxygen basis functions generally are unable to predict the tetragonal phase as thermodynamically more stable than the cubic. This appears to be a major failing of the interatomic potentials derived by Dwivedi *et al.* (100), used in this thesis.

- Ceria exists only in a fluorite phase. Attempts to stabilise non-cubic ceria structures produced systems having significantly greater internal energy than the fluorite.

- The most thermodynamically stable surface, in agreement to the (ceria) IP study by Vyas *et al.* (45,48), or the *ab initio* plane wave results of Christensen and Carter (59) is the {111}, having a (relaxed) surface energy of around 1.25-1.3 J/m^2.

- Ion relaxations in the {111} surface are almost negligible, indicating the extreme stability of the cleaved {111} planes.

- The second most stable surface, in agreement with the studies of both Vyas and Carter, is the {011}. In the current HF calculations, the {011} (relaxed) surface energy is found to be 2.1 J/m^2.

- The higher surface energy of the {011} slabs (in comparison to the {111}) suggests that the {011} surface is likely to be more catalytically active than the {111}.

- The structural and electronic relaxations in the {011} slabs are much more significant than those observed in the {111} surface, and appear correlated into two distinct columns, each relaxing towards the opposite end of the slabs.

A great many avenues for future study have been opened as a result of this work, in fact the results of some of the zirconia calculations have already been used in the study by Alfredsson *et al.* (98) to study the effects of noble metal deposition onto zirconia {011} and {111} surfaces.

Although time eventually ran out during the course of this work, partial studies were underway into similar surface deposition on ceria {011} and {111} surfaces, using the CASTEP code, based on the results of the preliminary plane wave calculations reported in this thesis. A similar bulk study of the electronic properties of yttria was performed, but not reported here, to allow future study of stabilised zirconia systems, and the properties of the resulting defect clusters. Until recent times, this was only possible through the use of interatomic potentials, although the recent work by Stapper *et al.* (58) proves that this is no longer the case. The difficulties encountered as a result of the optimisation process involved in CRYSTAL calculations made this a more lengthy process than that performed by Stapper, although we believe the additional benefits of a combined HF/DFT study possible with CRYSTAL are worth the additional expense.

Bibliography

1. Schrödinger, E. *Ann.Physik.* **1926,** *79* 361.
2. Born, M. *Z.Physik* **1926,** *38* 803.
3. Born, M.; Oppenheimer, J. R. *Ann.Physik.* **1927,** *84* 457.
4. Hartree, D. R. *Proc.Cambridge Phil.Soc.* **1928,** *24*(19), 111.
5. Hartree, D. R. *Proc.Cambridge Phil.Soc.* **1928,** *24*(19), 426.
6. Hartree, D. R. *Proc.Cambridge Phil.Soc.* **1928,** *24*(19), 89.
7. Fock, V. *Z.Physik* **1930,** *31* 1293.
8. Kohn, W.; Sham, L. J. *Physical Review A* **1965,** *140* 1133.
9. Saunders, V. R.; Dovesi, R.; Roetti, C.; Causá, M.; Harrison, N. H.; Orlando, R.; Zicovich-Wilson, C. M. *CRYSTAL98 Users Manual;* University of Torino: Torino, 1998.
10. Pisani, C.; Dovesi, R.; Roetti, C. *Hartree-Fock ab-initio Treatment of Crystalline Solids.;* Springer-Verlag: Heidelberg, 1988; Vol. 48.
11. Pauli, W. *Z.Physik* **1925,** *31* 765.
12. Slater, J. C. *Physical Review B* **1929,** *34* 1293.
13. Slater, J. C. *Physical Review B* **1930,** *35* 509.
14. Heisenberg; W. *Z.Physik* **1927,** *43* 172.
15. Pople, J. A.; Beveridge, D. L. *Approximate Molecular Orbital Theory;* McGraw-Hill: New York, 1970.
16. Slater, J. C. *Introduction to Chemical Physics;* McGraw-Hill: New York, 1939.
17. Slater, J. C. *Quantum Theory of Atomic Structure;* 3 ed.; McGraw-Hill: New York, 1960; Vol. 1.

18. Cora, F.; Patel, A.; Harrison, N. M.; Dovesi, R.; Catlow, C. R. A. *Journal of the American Chemical Society* **1996,** *118*(48), 12174-12182.

19. Cora, F.; Catlow, C. R. A. *Physica Status Solidi B-Basic Research* **2000,** *217*(1), 577-598.

20. Monkhorst, H. J.; Pack, J. D. *Physical Review B* **1976,** *13* 5188.

21. Perdew, J. P.; Zunger, A. *Physical Review B* **1981,** *23*(10), 5048-5079.

22. Perdew, J. P.; Wang, Y. *Physical Review B* **1986,** *33* 8800.

23. Perdew, J. P. *Physical Review B* **1989,** *40*(5), 3399.

24. Perdew, J. P.; Wang, Y. *Physical Review B* **1992,** *45*(23), 13244-13249.

25. Perdew, J. P. *Electronic Structure of Solids;* Akadamie Verlag: Berlin, 1991.

26. Becke, A. D. *Physical Review A* **1988,** *38*(6), 3098-3100.

27. Becke, A. D. *Journal of Chemical Physics* **1993,** *98*(2), 1372-1377.

28. Becke, A. D. *Journal of Chemical Physics* **1993,** *98*(7), 5648-5652.

29. Lee, C.; Parr, R. G. *Physical Review A* **1990,** *42*(1), 193-200.

30. Frisch, M. J.; Trucks, G. W.; Schlegel, H. B.; Gill, P. M. W.; Johnson, B. G.; Robb, M. A.; Cheeseman, J. R.; Keith, T. A.; Petersson, G. A.; Montgomery, J. A.; Raghavachari, K.; Al-Laham, M. A.; Zakrzewski, V. G.; Ortiz, J. V.; Foresman, J. B.; Peng, C. Y.; Ayala, P. Y.; Wong, M. W.; Andres, J. L.; Replogle, E. S.; Gomperts, R.; Martin, R. L.; Fox, D. J.; Binkley, J. S.; Defrees, D. J.; Baker, J.; Stewart, J. P.; Head-Gordon, M.; Gonzalez, C.; Pople, J. A. *Gaussian 94 (Revision E.1);* Gaussian Inc.: Pittsburgh PA, 1995.

31. Bardeen, J. *Journal of Chemical Physics* **1938,** *6* 372.

32. Miller, T. M.; Grassian, V. H. *Catalysis Letters* **1997,** *46*(3-4), 213-221.

33. Liu, W.; Wadia, C.; Flytzani-Stephanopoulos, M. *Catalysis Today* **1996,** *28*(4), 391-403.

34. Badwal, S. P. S.; Foger, K. *Ceramics International* **1996,** *22*(3), 257-265.

35. Steele, B. C. H. *J.Power Sources* **1994,** *49*(1-3), 1-14.

36. Hino, H.; Kobayashi, S.; Arata, K. *Journal of the American Chemical Society* **1979,** *101*(6439).

37. Hino, H.; Arata, K. *Journal of the Chemical Society-Chemical Communications* **1980,** 851.

38. Wyckoff, R. W. G. *Crystal Structures;* 2 ed.; Interscience: New York, 1963.

39. Gerward, L.; Staun-Olsen, A. S. *Powder Diffraction* **1993,** *8* 127.

40. Li, P.; Chen, I.-W.; Penner-Haan, J. E. *Physical Review B* **1993,** *48*(14), 10063-10073.

41. Lide, D. R. *CRC Handbook of Chemistry and Physics;* 77 ed.; CRC Press: Boac Raton, FL., 1996.

42. Mackrodt, W. C.; Woodrow, P. M. *Journal of the American Ceramic Society* **1986,** *69*(3), 277-280.

43. Kandil, H. M.; Greiner, J. D.; Smith, J. F. *Journal of the American Ceramic Society* **1984,** *67*(5), 341-346.

44. Balducci, G.; Kaspar, J.; Fornasiero, P.; Graziani, M.; Islam, M. S.; Gale, J. D. *Journal of Physical Chemistry B* **1997,** *101*(10), 1750-1753.

45. Vyas, S.; Grimes, R. W.; Gay, D. H.; Rohl, A. L. *Journal of the Chemical Society-Faraday Transactions* **1998,** *94*(19), 3059.

46. Vyas, S.; Grimes, R. W.; Gay, D. H.; Rohl, A. L. *Journal of the Chemical Society-Faraday Transactions* **1998,** *94*(3), 427-434.

47. Balducci, G.; Kaspar, J.; Fornasiero, P.; Graziani, M.; Islam, M. S. *Journal of Physical Chemistry B* **1998,** *102*(3), 557-561.

48. Vyas, S. Ph.D, University College London, 1997.

49. Hill, S.; Catlow, C. R. A. *Phys.Chem.Solids.* **1993,** *54*(4), 411-419.

50. Stefanovich, E. V.; Shluger, A. L.; Catlow, C. R. A. *Physical Review B* **1994,** *49*(17), 11560-11571.

51. Orlando, R.; Pisani, C.; Roetti, C.; Stefanovich, E. V. *Physical Review B* **1992,** *45*(2), 592-601.

52. Wuilloud, E.; Delley, B.; Schneider, W. D.; Baer, Y. *Physical Review Letters* **1984,** *53* 202.

53. Baudin, M.; Wojcik, M.; Hermansson, K.; Palmqvist, A. E. C.; Muhammed, M. *Chemical Physics Letters* **2001,** *335*(5-6), 517-523.

54. Stefanovich, E. V.; Shidlovskaya, E.; Shluger, A. L.; Zakharov, M. *Physica Status Solidi B-Basic Research* **1990,** *160*(2), 529-540.

55. Durand, P. H.; Barthelat, J. C. *Theoretica Chimica Acta* **1975,** *38* 283.

56. Fabris, S.; Paxton, A. T.; Finnis, M. W. *Physical Review B* **2000,** *61*(10), 6617-6630.

57. Finnis, M. W.; Paxton, A. T.; Methfessel, M.; vanSchilfgaarde, M. *Physical Review Letters* **1998,** *81*(23), 5149-5152.

58. Stapper, G.; Bernasconi, M.; Nicoloso, N.; Parrinello, M. *Physical Review B* **1999,** *59*(2), 797-810.

59. Christensen, A.; Carter, E. A. *Physical Review B* **1998,** *58*(12), 8050-8064.

60. Balducci, G.; Islam, M. S.; Kaspar, J.; Fornasiero, P.; Graziani, M. *Chem.Mater.* **2000,** *12*(3), 677-681.

61. Dovesi, R.; Causá, M.; Pisani, C.; Roetti, C. *Physical Review B* **1986,** *33*(2), 1308.

62. Hay, P. J.; Wadt, W. R. *Journal of Chemical Physics* **1985,** *82*(1), 270-283.

63. Guest, M. F.; Kendrick, J. H.; van Lenthe, J. H.; Sherwood, P. *GAMESS-UK 6.3, User's Guide and Reference Manual;* Daresbury Laboratory: Warrington, UK, 2001.

64. Andrae, D.; Haussermann, U.; Dolg, M.; Stoll, H.; Preuss, H. *Theoretica Chimica Acta* **1991,** *78*(4), 247-266.

65. Dovesi, R. 1998.

66. Birch, F. *J.Geophys.Res.* **1978,** *83* 1257.

67. Brennan, B. J.; Stacey, F. D. *J.Geophys.Res.* **1979,** *84* 5535.

68. Davis, L. A.; Gordon, R. B. *Journal of Chemical Physics* **1967,** 2250.

69. Murnagham, F. G. *Proc.Natl.Acad.Sci.U.S.A* **1944,** *30* 244.

70. Vinet, P.; Ferrante, J. H.; Rose, J. H.; Smith, J. R. *J.Geophys.Res.* **1987,** *92*(B9), 9319-9325.

71. Nakajima, A.; Yoshihara, A.; Ishigame, M. *Physical Review B* **1994,** *50*(18), 13297-13307.

72. Norenberg, H.; Briggs, G. A. D. *Physical Review Letters* **1997,** *79*(21), 4222-4225.

73. Norenberg, H.; Briggs, G. A. D. *Surface Science* **1998,** *404*(1-3), 734-737.

74. Marabelli, F.; Wachter, P. *Physical Review B* **1987,** *36*(2), 1238-1243.

75. Butorin, S. M.; Mancini, D. C.; Guo, J. H.; Wassdahl, N.; Nordgren, J.; Nakazawa, M.; Tanaka, S.; Uozumi, T.; Kotani, A.; Ma, Y.; Myano, K. E.; Karlin, B. A.; Shuh, D. K. *Physical Review Letters* **1996,** *77*(3), 574-577.

76. Pfau, A.; Schierbaum, K. D. *Surface Science* **1994,** *321*(1-2), 71-80.

77. Koelling, D. D.; BORING, A. M.; Wood, J. H. *Solid State Communications* **1983,** *47*(4), 227-232.

78. Mulliken, R. S. *Journal of Chemical Physics* **1955,** *23* 1833.

79. Sanchez-Portal, D.; Artacho, E.; Soler, J. M. *Solid State Communications* **1995,** *95*(10), 685-690.

80. Segall, M. D.; Pickard, C. J.; Shah, R.; Payne, M. C. *Molecular Physics* **1996,** *89*(2), 571-577.

81. Segall, M. D.; Shah, R.; Pickard, C. J.; Payne, M. C. *Physical Review B* **1996,** *54*(23), 16317-16320.

82. Glushkova, V. B.; Osiko, V. V.; Shcherbakova, L. G.; Aleksandrov, V. I.; Paputskii, Yu. N.; Tatarintsev, V. M. *Inorganic Materials (USSR)* **1978,** *13*(12), 1751-1754.

83. Kralik, B.; Chang, E. K.; Louie, S. G. *Physical Review B* **1998,** *57*(12), 7027-7036.

84. Liu, D. W.; Perry, C. H.; Feinberg, A. A.; Currat, R. *Physical Review B* **1987,** *36*(17), 9212-9218.

85. WWW Site: http://www.webelements.com. 2001.

86. Aldebert, P.; Traverse, J. P. *Journal of the American Ceramic Society* **1985,** *68*(1), 34-40.

87. Jansen, H. J. F.; Gardner, J. A. *Physica B & C* **1988,** *150*(1-2), 10-18.

88. Jansen, H. J. F. *Physical Review B* **1991,** *43*(9), 7267-7278.

89. Cohen, R. E.; Mehl, M. J.; Boyer, L. L. *Physica B & C* **1988,** *150*(1-2), 1-9.

90. Jomard, G.; Petit, T.; Pasturel, A.; Magaud, L.; Kresse, G.; Hafner, J. *Physical Review B* **1999,** *59*(6), 4044-4052.

91. Fukuhara, M.; Yamauchi, I. *Journal of Materials Science* **1993,** *28*(17), 4681-4688.

92. Kisi, E. H.; Howard, C. J. *Journal of the American Ceramic Society* **1998,** *81*(6), 1682-1684.

93. Kresse, G.; Furthmüller, J. *VASP 4.4: Vasp the Guide;* Tecnische Universität Wien: Vienna, 1999.

94. French, R. H.; Glass, S. J.; Ohuchi, F. S.; Xu, Y. N.; Ching, W. Y. *Physical Review B* **1994,** *49*(8), 5133-5141.

95. McComb, D. W. *Physical Review B* **1996,** *54*(10), 7094-7102.

96. Teufer, G. *Acta Crystallographica* **1962,** *15* 1187.

97. Howard, C. J.; HILL, R. J.; Reichert, B. E. *Acta Crystallography B* **1988,** *44* 116-120.

98. Alfredsson, M.; Catlow, C. R. A. *PCCP* **2001,** *18*(3), 4129-4140.

99. Lindan, P. *The Guide 1.1 to CASTEP 3.9;* Daresbury Laboratory: Warrington, UK., 1999.

100. Dwivedi, A.; Cormack, A. N. *Philosophical Magazine A-Physics of Condensed Matter Structure Defects and Mechanical Properties* **1990,** *61*(1), 1-22.

101. Perdew, J. P.; Wang, Y. *Physical Review B* **1992,** *46*(20), 12947-12954.

102. Wang, Y.; Perdew, J. P. *Physical Review B* **1991,** *44*(24), 13298-13307.

103. Sayle, T. X. T.; Parker, S. C.; Catlow, C. R. A. *Journal of Physical Chemistry* **1994,** *98*(51), 13625-13630.

104. Conesa, J. C. *Surface Science* **1995,** *339*(3), 337-352.

105. Corá, F.; Patel, A.; Harrison, N. H.; Dovesi, R.; Catlow, C. R. A. *Journal of the American Chemical Society* **1996,** *118*(48), 12174-12182.

106. Corá, F.; Patel, A.; Harrison, N. H.; Roetti, C.; Catlow, C. R. A. *Journal of Materials Chemistry* **1997,** *7*(8), 959-967.

107. Alfredsson, M.; Bromley, S. T.; Catlow, C. R. A. *Theoretical aspects of heterogeneous catalysis.;* Kluwer Academic Publisher: Netherlands, 2001.

Appendix A: Tables of Basis Sets

This appendix reports tables listing the various parameters derived for use in the Gaussian basis sets in the CRYSTAL calculations which were performed in this thesis.

Table A1: Hay and Wadt small-core pseudopotential parameters for Ce. The definition of the various parameters is given in section 2.3.3 in equation (2.25).

Ce Hay and Wadt		
α_{kl}	C_{kl}	n_{kl}
9.20747930	-15.3487561	-1
1.86730116	-5.84323953	-1
1.89370134	-255.562383	0
1.97914859	307.313928	0
10.7429697	10.6699017	-2
7.75592979	12.2292109	-2
1.81564126	124.942466	0
1.67164719	-84.5999868	0
1.70642047	24.9446755	0
6.48933742	10.2861447	-2

Table A2: The optimised Ce Hay and Wadt small-core pseudopotential valence basis functions.

		Coefficient	
Type	Exponent	*s*	*p* or *d*
4*sp*	3.45700	3.137491	1.949717
	4.29100	-1.429517	-0.912311
	2.29000	-2.675848	-2.020037
5*sp*	0.668400	1.0	1.0
6*sp*	0.285700	1.0	1.0
3*d*	0.591600		0.278320
	0.300200		0.458630
4*d*	0.124400		1.0

Table A3: The optimised Zr Hay and Wadt small-core pseudopotential basis set.

		Coefficient	
Type	Exponent	*s*	*p* or *d*
3*sp*	6.625845	-0.061704	0.056691
	2.226134	4.210912	0.913255
	1.690689	-2.584539	-1.202152
4*sp*	0.690186	1.0	1.0
5*sp*	0.301306	1.0	1.0
3*d*	2.642989		-0.037002
	1.646424		0.237752
	0.615145		0.653019
4*d*	0.187449		1.0

Table A4: The optimised Zr Stoll-Pruess small-core pseudopotential basis set.

		Coefficient	
Type	Exponent	*s*	*p* or *d*
3*sp*	6.267700	-0.662120	0.132450
	4.054500	1.463980	0.556330
	1.352000	-0.347380	-0.839680
4*sp*	0.571300	1.0	1.0
5*sp*	0.182100	1.0	1.0
3*d*	2.642989		-0.037002
	1.646424		0.237752
	0.615145		0.653019
4*d*	0.187449		1.0

Table A5: The optimised oxygen All-Electron 8-51G basis set.

		Coefficient	
Type	Exponent	*s*	*p* or *d*
1*s*	4000.00	0.00144	
	1355.58	0.00764	
	248.545	0.05370	
	69.5339	0.16818	
	23.8868	0.36039	
	9.27593	0.38612	
	3.82034	0.14712	
	1.23514	0.07105	
2*sp*	52.1878	-0.00873	0.00922
	10.3293	-0.08979	0.07068
	3.21034	-0.04079	0.20433
	1.23514	0.37666	0.34958
	0.536420	0.42248	0.27774
3*sp*	0.21830	1.0	1.0

Table A6: The oxygen 8-411dG basis set.

		Coefficient	
Type	Exponent	*s*	*p* or *d*
1*s*	4000.00	0.00144	
	1355.58	0.00764	
	248.545	0.05370	
	69.5339	0.16818	
	23.8868	0.36039	
	9.27593	0.38612	
	3.82034	0.14712	
	1.23514	0.07105	
2*sp*	49.430	-0.00883	0.00958
	10.470	-0.09150	0.06960
	3.235	-0.04020	0.20650
	1.217	0.37900	0.34700
3*sp*	0.5000	1.0	1.0
4*sp*	0.2183	1.0	1.0
3*d*	0.5000		1.0

Table A7: The Zr All-Electron basis set.

		Coefficient	
Type	Exponent	*s*	*p* or *d*
s	3085030	0.000038	
	418055	0.000362	
	82533	0.002349	
	19662	0.012527	
	5438.44	0.053130	
	1712.33	0.175607	
	604.764	0.393718	
	235.135	0.474028	
	95.5675	0.178180	
sp	6807.1	-0.000404	0.001043
	1535.29	-0.007462	0.010164
	453.951	-0.066553	0.063259
	155.134	-0.166837	0.248721
	59.8272	0.251220	0.515161
	25.687	0.782849	0.450879
	11.4476	0.298580	0.120840
sp	151.789	0.004661	-0.014487
	51.2486	-0.042645	-0.088443
	20.6628	-0.395485	0.979073
	8.5248	0.217897	1.163788
	3.6821	1.164957	1.453538
	1.4944	0.288347	0.359850
d	297.855		0.00597
	87.4716		0.0474
	31.5134		0.1925
	12.3703		0.4114
	4.9738		0.4381
	1.957		0.1588
sp	3.8653	-1.595	-0.1149
	1.739	-0.364	0.514
	0.7875	4.9455	1.3848
sp	0.33848	1.0	1.0
d	2.6978		0.08308
	0.9959		0.34899
d	0.413544		0.52029

Table A8: The Ce All-Electron basis set.

		Coefficient	
Type	Exponent	*s*	*p* or *d*
s	17261.00	0.0607638	
	2614.223	0.3656923	
	575.254	0.6920432	
s	765.722	-0.111540	
	75.1958	0.733938	
	31.3814	0.342436	
s	67.4758	-0.280158	
	12.4380	0.894026	
	5.35753	0.266555	
s	11.4136	0.379774	
	2.79730	-0.851733	
	1.34464	-0.389023	
s	2.20972	0.997277	
	0.43697	-2.317257	
	0.19858	-1.026952	
s	0.15000	2.757516	
sp	1141.0638	0.079533	0.079533
	267.8100	0.419739	0.419739
	80.1475	0.640965	0.640965
sp	159.3610	-0.033281	-0.033281
	29.0221	0.3970831	0.3970831
	11.5685	0.6699493	0.6699493
sp	4.8235	0.463126	0.463126
	2.1015	0.581822	0.581822
	0.7859	0.075023	0.075023
sp	0.5000	0.999715	0.999715
d	164.1335		0.115244
	46.5081		0.492516
	15.1987		0.609939
d	8.4807		0.275854
	3.1599		0.581454
	1.2103		0.292116
d	0.1500		10.466991

Table A9: Density Functional auxiliary basis sets optimised for zirconium and oxygen. These basis sets were used in the CRYSTAL LDA, GGA and B3LYP calculations reported in this thesis.

Zirconium			
Type	Number of Gaussians	Smallest Exponent	Largest Exponent
s	8	0.07	50
g	3	0.2	1.8
i	2	0.2	0.6

Oxygen			
Type	Number of Gaussians	Smallest Exponent	Largest Exponent
s	12	0.1	2000
p	4	0.1	5.0
d	3	0.2	2.5

Table A10: The atomic basis set for oxygen.

		Coefficient	
Type	Exponent	*s*	*p* or *d*
1*s*	4000.00	0.00144	
	1355.58	0.00764	
	248.545	0.05370	
	69.5339	0.16818	
	23.8868	0.36039	
	9.27593	0.38612	
	3.82034	0.14712	
	1.23514	0.07105	
2*sp*	49.430	-0.00883	0.00958
	10.470	-0.09150	0.06960
	3.235	-0.04020	0.20650
	1.217	0.37900	0.3470
3*sp*	0.4819	1.0	1.0
4*sp*	0.1736	1.0	1.0
5*sp*	0.0462		1.0